

Observing the Universe with a Polarizing Fourier Transform Spectrometer called PIXIE

by

Peter Campbell Nagler

A.B., Physics and French, Bowdoin College, 2009

Sc.M., Physics, Brown University, 2013

A DISSERTATION SUBMITTED IN PARTIAL FULFILLMENT OF THE REQUIREMENTS FOR

THE DEGREE OF DOCTOR OF PHILOSOPHY

IN THE DEPARTMENT OF PHYSICS AT BROWN UNIVERSITY

Providence, Rhode Island USA

May 2017

© Copyright 2017 by Peter Campbell Nagler

This dissertation by Peter Campbell Nagler is accepted in its present form by
the Department of Physics as satisfying the
dissertation requirement for the degree of
Doctor of Philosophy.

Date
Gregory Tucker, Advisor

Recommended to the Graduate Council

Date
Ian Dell'Antonio, Reader

Date
Dale Fixsen, Reader

Approved by the Graduate Council

Date
Andrew G. Campbell
Dean of the Graduate School

Curriculum vitae

Contact Information

Peter Campbell Nagler
16 Tell St., Apt. 3
Providence, RI 02909 USA

Education

Brown University, Providence, RI USA 2011 - 2017

- Ph.D., Physics, May 2017

Thesis Title: Observing the Universe with a Fourier Transform Spectrometer Called PIXIE

Thesis Advisor: Professor Greg Tucker

- Sc.M., Physics, May 2013

Bowdoin College, Brunswick, ME USA 2005 - 2009

- A.B., Physics and French with honors, May 2009

Cum laude diploma

Research and Professional Experience

Graduate research assistant 2012 - 2017

Observational Cosmology Lab,
Department of Physics,
Brown University
Providence, RI USA
Advisor: Professor Greg Tucker

Electronics engineer/graduate co-op 2011 - 2017

Detector Systems Branch,
NASA/Goddard Space Flight Center
Greenbelt, MD USA

Integration and test engineer 2009 - 2011

MEI Technologies, Inc., and
NASA/Goddard Space Flight Center
Greenbelt, MD USA

Awards

Fellowships

- Brown University Department of Physics
Galkin Foundation Fellowship 2016 - 2017
- NASA Rhode Island Space Grant Graduate Fellowship 2012 - 2013
- IEEE Applied Superconductivity Graduate Fellowship 2011 - 2012

Teaching awards

- Brown University Department of Physics
Graduate Teaching Award of Excellence 2012

Selected Publications

- D. J. Fixsen, A. Kogut, R. S. Hill, P. C. Nagler, L. T. Seals, and J. M. Howard. Dealing with beam structure in PIXIE. *Proc. SPIE*, 99141B-99141B-10, 2016.
- A. Kogut, D. J. Fixsen, P. C. Nagler, and G. S. Tucker. Systematic error mitigation for the PIXIE instrument. *Proc. SPIE*, 991438-991438-7, 2016.
- P. C. Nagler, K. T. Crowley, K. L. Denis, A. M. Devasia, D. J. Fixsen, A. J. Kogut, G. Manos, S. Porter, and T. R. Stevenson. Multimode bolometer development for the PIXIE instrument. *Proc. SPIE*, 99141A-99141A-10, 2016.
- P. C. Nagler, E. Canavan, R. De Alba, and T. R. Stevenson. Development of superconducting magnetic heat switches for an ideal integrating bolometer. *Journal of Low Temperature Physics*, 184(1):280–285, 2016.
- P. C. Nagler, D. J. Fixsen, A. Kogut, and G. S. Tucker. Systematic effects in polarizing Fourier transform spectrometers for cosmic microwave background observations. *The Astrophysical Journal Supplement Series*, 221:21, November 2015.
- J.-P. Porst, S. R. Bandler, J. S. Adams, M. A. Balvin, S. E. Busch, M. E. Eckart, R. L. Kelley, C. A. Kilbourne, S. J. Lee, P. C. Nagler, F. S. Porter, J. E. Sadleir, G. M. Seidel, S. J. Smith, and T. R. Stevenson. Characterization and performance of magnetic calorimeters for applications in x-ray spectroscopy. *Journal of Low Temperature Physics*, 176(5):617–623, 2014.
- A. G. Kozorezov, C. J. Lambert, S. R. Bandler, M. A. Balvin, S. E. Busch, P. C. Nagler, J.-P. Porst, S. J. Smith, T. R. Stevenson, and J. E. Sadleir. Athermal energy loss from x-rays deposited in thin superconducting films on solid substrates. *Phys. Rev. B*, 87:104504, Mar 2013.

- T. R. Stevenson, M. A. Balvin, S. R. Bandler, S. E. Busch, K. L. Denis, W. T. Hsieh, D. P. Kelly, W. Merrell, P. C. Nagler, J. P. Porst, J. E. Sadleir, G. M. Seidel, and S. J. Smith. Superconducting effects in optimization of magnetic penetration thermometers for x-ray microcalorimeters. *IEEE Transactions on Applied Superconductivity*, 23(3):2300605–2300605, June 2013.
- S. R. Bandler, K. D. Irwin, D. Kelly, P. C. Nagler, J.-P. Porst, H. Rotzinger, J. E. Sadleir, G. M. Seidel, S. J. Smith, and T. R. Stevenson. Magnetically coupled microcalorimeters. *Journal of Low Temperature Physics*, 167(3):254–268, 2012.
- E. M. Barrentine, D. E. Brandl, A. D. Brown, K. L. Denis, F. M. Finkbeiner, W. T. Hsieh, P. C. Nagler, T. R. Stevenson, P. T. Timbie, and K. U-Yen. Can the lateral proximity effect be used to create the superconducting transition of a micron-sized TES? *Journal of Low Temperature Physics*, 167(3):195–201, 2012.
- P. C. Nagler, J. S. Adams, M. A. Balvin, S. R. Bandler, K. L. Denis, W.-T. Hsieh, D. P. Kelly, J.-P. Porst, J. E. Sadleir, G. M. Seidel, S. J. Smith, and T. R. Stevenson. Performance of magnetic penetration thermometers for x-ray astronomy. *Journal of Low Temperature Physics*, 167(3):455–460, 2012.
- E. M. Barrentine, D. E. Brandl, A. D. Brown, K. L. Denis, W. T. Hsieh, P. C. Nagler, T. R. Stevenson, D. J. Talley, P. T. Timbie, and K. U-Yen. Thermal conductance measurements of a micron-sized transition-edge hot-electron microbolometer. *IEEE Transactions on Applied Superconductivity*, 21(3):258–261, June 2011.

Presentations

- P. C. Nagler, *et al.*, Multimode bolometer development for the PIXIE instrument. SPIE Astronomical Telescopes and Instrumentation. Edinburgh, UK. June 2016. Oral presentation.
- P. C. Nagler, *et al.*, Development of superconducting magnetic heat switches for an ideal integrating bolometer. 16th International Workshop on Low Temperature Detectors. Grenoble, France. July 2015. Poster presentation.
- P. C. Nagler, *et al.*, Fabrication of magnetic penetration thermometers (MPTs) optimized for soft x-ray spectroscopy. 15th International Workshop in Low Temperature Detectors. Pasadena, CA USA. June 2013. Poster presentation.
- P. C. Nagler, *et al.*, Performance of magnetic penetration thermometers (MPTs) for X-ray astronomy. 14th International Workshop on Low Temperature Detectors. Heidelberg, Germany. August 2011. Poster presentation.

Teaching experience

Tutor Fall 2013

Physics 050 - Foundations of Mechanics
Undergraduate level
Department of Physics,
Brown University

Teaching assistant Fall 2013

Physics 050 - Foundations of Mechanics
Undergraduate level
Department of Physics,
Brown University

Teaching assistant Fall 2011 - Spring 2012

Physics 1560 - Modern Physics Laboratory
Undergraduate level
Department of Physics,
Brown University

Teaching assistant Fall 2011 - Spring 2012

Physics 2010 - Techniques in Experimental Physics
Graduate level
Department of Physics,
Brown University

Teaching assistant Spring 2007 - Fall 2008

Physics 104 - Introductory Electromagnetism
Undergraduate level
Department of Physics,
Bowdoin College

Teaching assistant Fall 2007 - Spring 2009

Physics 103 - Introductory Mechanics
Undergraduate level
Department of Physics,
Bowdoin College

Preface and Acknowledgments

I would like to acknowledge and thank all of those who supported, encouraged, distracted, and pushed me over the past six years. Special thanks go to my advisor Greg, my thesis committee of Dale and Ian, my first year late-night problem set buddies (Altan, Gordon, Dan, Bob), my co-prisoner in the SciLi while preparing for the qual (Dan), my labmates at Brown, my friends and colleagues at Goddard (particularly Al, Thomas, and others who contributed to this work), my parents and brothers, and Ida. This would have been impossible without all of you. I am also grateful for all the funding sources that generously supported this work, including the NASA/GSFC IRAD program, the NASA/GSFC co-op program, the Brown Physics department and Graduate School, and the Galkin Foundation.

Contents

Contents	ix
List of Figures	xiii
List of Tables	xvi
1 Introduction	1
2 The <i>PIXIE</i> experiment	5
2.1 Introduction	5
2.2 Instrument description	7
2.2.1 Spacecraft and Thermal Design	7
2.2.2 Scan strategy	9
2.2.3 Optics	10
2.2.4 Detectors	16
2.3 Science goals	18
2.3.1 The cosmic microwave background	19
2.3.2 Polarization	22
2.3.3 Spectral distortions	25
2.3.3.1 Thermal distortions	25
2.3.3.2 Non-thermal distortions	26
2.3.4 Foregrounds	28

2.3.4.1	Synchrotron emission	29
2.3.4.2	Thermal dust	30
2.3.5	Line emission	32
2.3.6	Summary	34
3	Instrumental systematic effects	37
3.1	Introduction	37
3.2	The ideal instrument	38
3.2.1	Jones matrix method	38
3.2.2	Calculated signal	40
3.3	Emission errors	41
3.3.1	Review of theory	42
3.3.2	Primary mirrors with non-zero emissivity	43
3.3.2.1	Modified operators	43
3.3.2.2	Calculated signal	44
3.3.2.3	Identifying and correcting error	46
3.3.2.4	Conclusion	49
3.3.3	Polarizer grid A with non-zero emissivity	50
3.3.3.1	Modified operators	50
3.3.3.2	Calculated signal	52
3.3.3.3	Identifying and correcting error	53
3.3.3.4	Conclusion	54
3.3.4	Polarizer B with non-zero emissivity	55
3.3.4.1	Modified operators	56
3.3.4.2	Calculated signal	57
3.3.4.3	Conclusion	57
3.3.5	Emission from non-optical components	58
3.3.5.1	Emission from transfer mirror frames	58

3.3.5.2	Calculated signal	59
3.3.5.3	Identifying and correcting error	59
3.3.5.4	Conclusion	61
3.4	Geometric errors	62
3.4.1	Misalignment of polarizers A and D	62
3.4.1.1	Modified operators	63
3.4.1.2	Calculated signal	64
3.4.2	Conclusion	65
3.5	Mirror transport mechanism (MTM) errors	65
3.5.1	Phase errors	66
3.5.1.1	The ideal interferogram	66
3.5.1.2	Asymmetric apodization	68
3.5.1.3	Asymmetric interferogram	70
3.5.1.4	Misaligned transfer mirrors	74
3.5.1.5	Conclusion	75
3.5.2	Sampling errors	75
3.5.2.1	Position errors	77
3.5.2.2	Frequency scale errors	79
3.5.3	Harmonic oscillations of the instrument	79
3.5.3.1	Conclusion	81
3.6	Spin-synchronous errors	81
3.6.1	Gain drifts	83
3.6.2	Conclusion	86
3.7	<i>PIXIE</i> as a two-element radio array	86
3.8	Conclusion	89
4	Bolometers	92
4.1	Introduction	92

4.2	Detector design and fabrication	93
4.2.1	Overview	93
4.2.2	Absorber structure	93
4.2.3	Endbanks	96
4.2.4	Frame	97
4.3	Cryogenic detector performance	98
4.3.1	Load curves	99
4.3.2	Noise analysis	104
4.4	Next-generation detector assembly	106
4.4.1	Overview	107
4.4.2	Thermal design	109
4.4.3	Filter design	110
4.4.4	Amplifier design	112
4.4.5	Preliminary tests	113
4.5	Detector environmental tests	115
4.5.1	Vibration package	120
4.5.2	MIDEX-specified vibration test	121
4.5.3	GEVS-specified vibration test	122
4.5.4	Results	123
4.6	Conclusion	125
5	Conclusion and Outlook	127
	Bibliography	130

List of Figures

1.1	The CMB intensity spectrum as measured by <i>COBE/FIRAS</i>	2
1.2	Map of the CMB temperature deviation from its mean at 5' resolution (top) and its spherical harmonic transform (bottom), as measured by the <i>Planck</i> satellite.	3
2.1	Layout of the <i>PIXIE</i> spacecraft.	8
2.2	Illustration of <i>PIXIE</i> 's scan strategy.	9
2.3	Cartoon of the <i>PIXIE</i> FTS.	11
2.4	Schematic showing the possible positions of <i>PIXIE</i> 's external calibrator.	12
2.5	Cartoon of a single <i>PIXIE</i> bolometer.	17
2.6	Cartoon of a hybridized pair of <i>PIXIE</i> bolometers.	18
2.7	Thermal history of the universe, highlighting the science accessible to <i>PIXIE</i>	19
2.8	Relationship between distortions to the CMB blackbody and the energy release history of the early universe.	27
2.9	Line emission distortions to the CMB blackbody.	28
2.10	Comparison of single modified blackbody and multiple modified blackbody dust models.	32
2.11	Summary of <i>PIXIE</i> 's sensitivity as a function of optical frequency and spatial frequency.	36

3.1	Error due to emissive primary mirrors.	49
3.2	Error due to an emissive polarizer A.	55
3.3	Error due to emissive non-optical components.	61
3.4	The ideal two-sided interferogram showing the Fourier transform of the polarized CMB.	67
3.5	Ideal apodization function (top) and its non-ideal counterpart (bottom).	70
3.6	Error in foreground measurements due to asymmetries in the apodization function.	71
3.7	Sampling error spectrum due to a zeroth sample offset or instrumental vibrations.	76
3.8	Model difference spectrum we expect to measure with <i>PIXIE</i>	77
3.9	Interferogram showing the Fourier transform of the composite foreground spectrum and the single-pixel mirror transport mechanism position error requirement that gives us 0.01% accuracy in foreground intensity measurements.	78
3.10	Effect of sample position errors on foreground subtractions.	82
3.11	Model interferogram exhibiting gain error.	83
3.12	Error due to spin-synchronous gain drifts.	84
3.13	Spectra of the raw systematic errors and their combined spectrum.	90
3.14	Spectra of residual systematic errors and their combined spectrum.	91
4.1	Scanning electron micrograph of a completed bolometer showing the interface between the absorber structure and the endbank.	94
4.2	White light interferometer image showing the flatness of the absorber achieved after implementing the tensioning scheme.	95
4.3	Single bolometer packaged for dark tests in the <i>Astro-E2/Suzaku</i> dewar.	97
4.4	Basic bias and readout circuit used for dark detector characterization.	98
4.5	Series of measured bolometer load curves.	99

4.6	Average thermal conductance as a function of thermistor temperature.	100
4.7	DC electrical responsivity as a function of bias current for a few bath temperatures.	102
4.8	Measured noise spectrum along with the fit from our thermal model.	103
4.9	Predicted bolometer NEP calculated for the optical and electrical bias conditions in expected in flight.	105
4.10	Next-generation <i>PIXIE</i> detector assembly.	107
4.11	Next-generation cryogenic differential amplifier schematic.	112
4.12	Measured IV curves of a typical <i>PIXIE</i> JFET.	114
4.13	Scatter plot showing the spread in measured JFET IV characteristics.	115
4.14	<i>PIXIE</i> sub-Kelvin experimental setup.	116
4.15	Power flowing to the bolometer plate as a function of JFET temperature.	117
4.16	<i>PIXIE</i> detector packaged for vibration testing.	118
4.17	<i>PIXIE</i> vibration package mounted on the vibration table.	119
4.18	Axial and lateral vibration levels that MIDEEX hardware must survive.	121
4.19	GEVS-specified vibration power spectral density.	122
4.20	Results of GEVS random vibration test along the bolometer's axis of absorption.	123
4.21	Interferometer measurement of the absorber after testing at GEVS levels.	124

List of Tables

2.1	Rotational transition lines of ^{12}CO in the <i>PIXIE</i> bandwidth where contamination of CMB measurements is a concern.	33
3.1	Systematic error magnitudes at 215 GHz before and after mitigation.	91
4.1	Results of thermal model assuming that the powder filter is at $T = 2.6$ K.	110
4.2	Results of thermal model accounting for the powder filter's finite thermal conductance.	110
4.3	Results of thermal model for the case where the CuNi cladding has been stripped from the tensioned leads.	111
4.4	Thermal properties of detector assembly materials.	111

Chapter 1

Introduction

Since its discovery in the 1960s by Penzias and Wilson [1], the cosmic microwave background (CMB) has been studied and understood with ever-increasing precision. Based on measurements by the *FIRAS* instrument on the *COBE* satellite [2–5] and the *COBRA* sounding rocket experiment [6, 7], it is now known that the CMB is a near-perfect blackbody with a temperature of 2.72548 ± 0.00057 K (see Figure 1.1). This provides significant support for a hot big bang model of the universe, as predicted in the 1940s [8]. Theoretical predictions of spatial temperature fluctuations due to density perturbations of CMB radiation [9] and due to scattering of CMB radiation during recombination [10–12] have been confirmed and characterized with observations from satellite [2, 13, 14], balloon [15–23], and ground-based [24–44] telescopes (see Figure 1.2). Some of these experiments have also measured the even parity “*E*-mode” polarization of the CMB that results from Thomson scattering of a scalar quadrupolar anisotropic radiation field off free electrons in the primordial plasma. Odd parity “*B*-mode” polarization resulting from gravitational lensing of CMB photons has also been measured. Together, these measurements have helped form and refine a standard model of cosmology known as the Λ CDM model (see [45]).

Despite these successes, several important questions remain which could be ad-

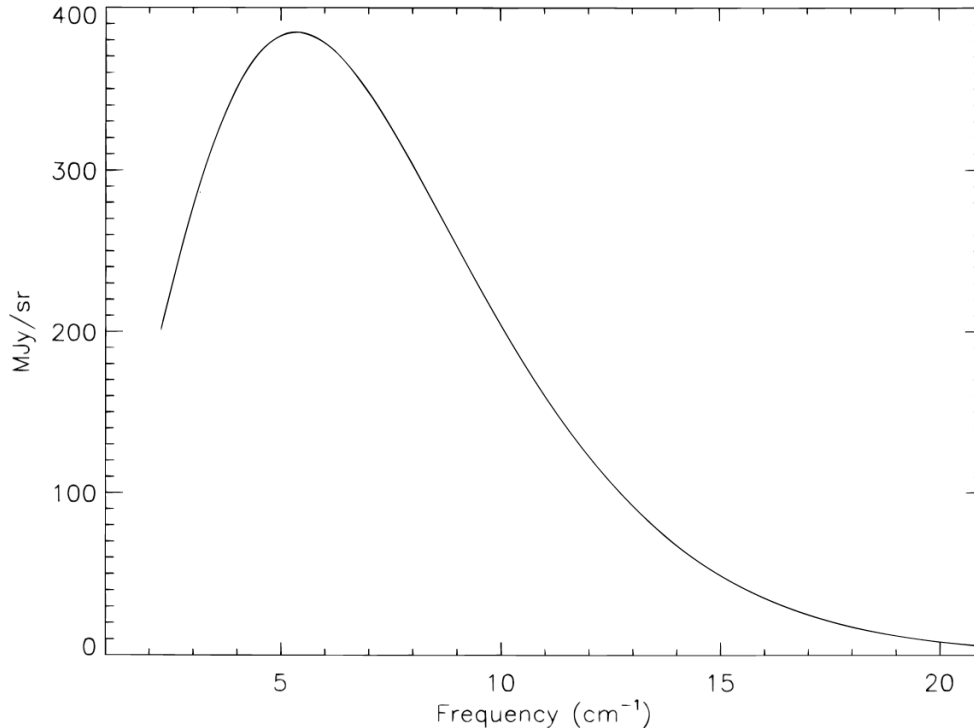


Figure 1.1 The CMB intensity spectrum as measured by *COBE/FIRAS* [5, 50]. The error bars in this plot are narrower than the line width. This measured spectrum is consistent with a Planck spectrum with a temperature of 2.72548 ± 0.00057 K.

dressed by even better observations of the CMB. For example, *B*-mode polarization of the CMB, resulting from the interaction of gravitational waves produced during inflation with the primordial plasma, has been predicted [46, 47]. To this point, however, no experiment has had the right combination of sensitivity, immunity to systematic effects, and understanding of galactic foregrounds, to either measure or rule out the existence of the *B*-mode signal. Likewise a number of physical processes can lead to perturbations to the CMB blackbody spectrum known as “spectral distortions” [e.g., 48, 49], but again to this point no experiment has been optimized for such measurements.

This thesis focuses on the *Primordial Inflation Explorer (PIXIE)* [52–54], a proposed space-based Fourier transform spectrometer (FTS) capable of addressing these two gaps in our experimental understanding of the CMB. In Chapter 2, I introduce the

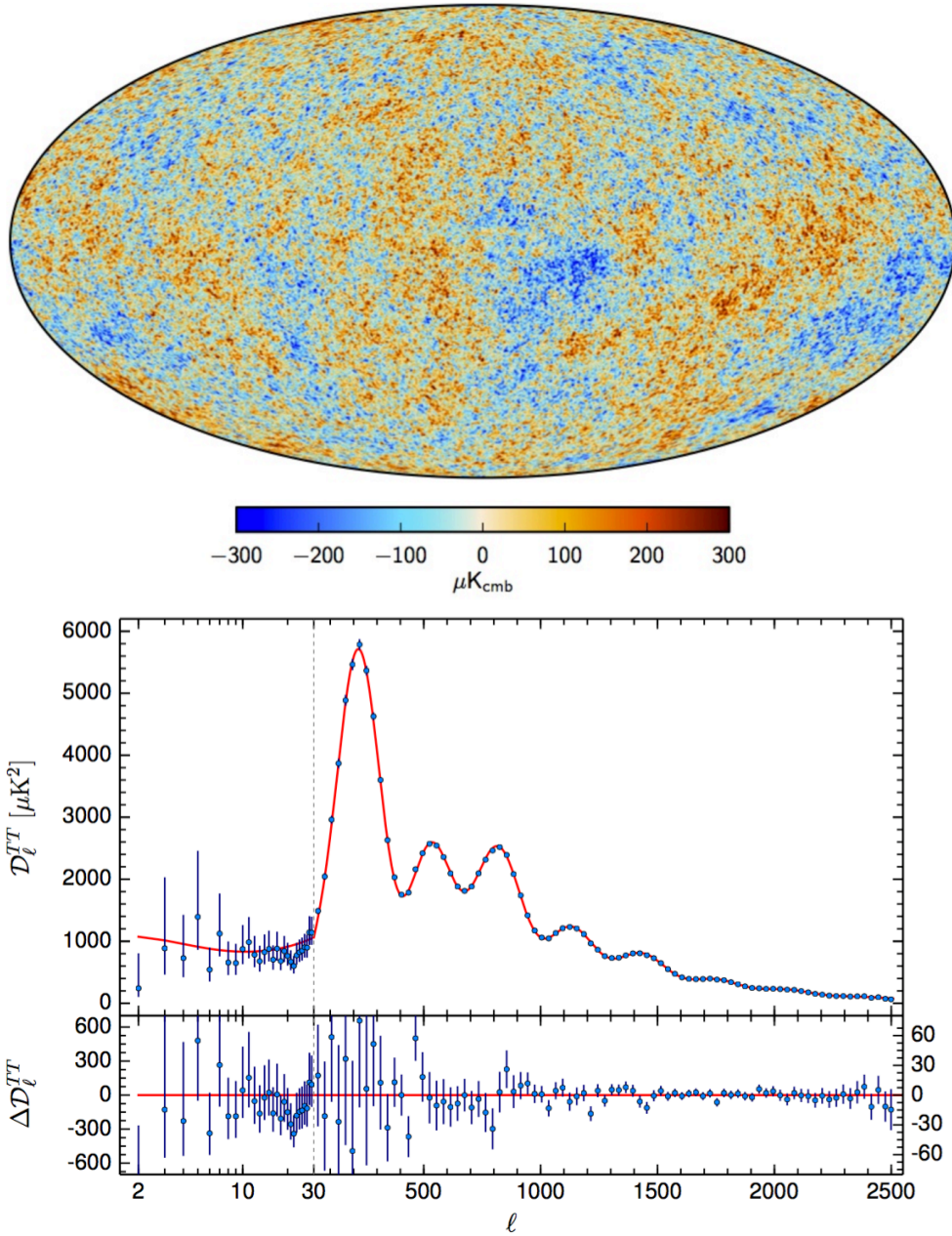


Figure 1.2 Map of the CMB temperature deviation from its mean at 5' resolution (top) and its spherical harmonic transform (bottom), as measured by the *Planck* satellite [51]. The temperature spectrum shows measurements with error bars and the best-fit prediction from ΛCDM cosmology, plotted as a function of multipole moment ℓ . The vertical dashed line at $\ell = 30$ separates spectral regions where different foreground removal techniques were used.

proposed *PIXIE* instrument and outline its science mission. In Chapter 3, I present an analytic analysis of *PIXIE*'s instrumental systematic effects. In Chapter 4, I present the details of the polarization-sensitive multimode bolometers we are developing for *PIXIE*. I also describe the front end readout electronics and the cryogenic detector assembly. Finally, in Chapter 5, I give the current status and future outlook for the development of *PIXIE*.

Chapter 2

The *PIXIE* experiment

2.1 Introduction

FTS measurements from balloon [16, 55], sounding rocket [6], and satellite [5] platforms have made significant contributions to CMB studies. Recently there has been renewed interest in deploying a FTS from a satellite platform [e.g., 52–54, 56] in order to measure the *B*-mode polarization signal of the CMB [46, 47] and spectral distortions of the CMB blackbody [48, 49]. Such measurements would provide critical tests of early universe and inflationary cosmology, probing physics at energies twelve orders of magnitude higher than is accessible to particle accelerators.

FTSs are particularly well equipped to measure these faint signals. First, they cover a wide frequency band with many channels, enabling the measurement and rejection of foreground signals. This is critical in order to distinguish between cosmological signals and signals originating within our own Galaxy [see 57]. Second, their symmetry leads to excellent control over instrumental systematic effects.

PIXIE is a proposed NASA-led Medium Class Explorer (MIDEX) mission whose science instrument is a polarizing FTS. The *PIXIE* experiment is based on a simple ansatz. The CMB is a near-perfect blackbody at a temperature of 2.725 K. The

PIXIE instrument will be kept isothermal with the CMB at a temperature of 2.725 K. Therefore the detectors will always be looking into a near-perfect blackbody cavity at the CMB temperature. Regardless of where the instrument points or of internal absorption and emission, the detectors will see the same thing, a Planck spectrum with a temperature of 2.725 K. Photons incident from the sky will be indistinguishable from those emitted by the instrument.

PIXIE is a nulling interferometer; it is sensitive only to the difference between orthogonal polarizations of incident light. Therefore to the extent the CMB is a blackbody, and to the extent its optics are isothermal with the CMB, *PIXIE* will measure zero. *PIXIE* has two modes of operation: polarization mode and spectral mode. In polarization mode, both beams are open to the sky and the instrument is sensitive only to Stokes Q and U . In spectral mode, one beam is blocked by a full-aperture blackbody calibrator and the instrument is sensitive to Stokes I , Q , and U . In polarization mode, the *PIXIE* design is ideal for measuring faint polarized signals in a bright unpolarized background. Likewise in spectral mode, the *PIXIE* design is ideal for measuring the difference between the intensity spectra of the sky and the instrument's calibrator.

PIXIE is a space-based instrument with two input beams that are co-pointed. The entire instrument spins about the same axis with a period of ~ 1 minute. Thus in a few seconds the polarization directions are interchanged. The instrument spin axis moves so that over the course of a few hours a great circle is traced out on the sky. This circle, 90 degrees from the sun, precesses so that over the course of a year the entire sky is mapped twice. *PIXIE* will operate from the second Sun-Earth Lagrange point (L2).

PIXIE will sample the sky's largest angular scales ($2 < \ell < 100$). The long-term stability and complete sky coverage of a space platform enables measurements down to the $\ell = 2$ mode. The $\ell = 1$ mode is also accessible, but it is ambiguous whether

the signal is cosmological in origin or results from our own motion in the universe. It is retained as a calibration source. So far, it has not been shown that ground or balloon platforms are capable of such measurements [e.g., 58]. *PIXIE*'s beam size (2.65°) limits the high spatial frequency capability of the instrument. Of key importance to the science mission is that *PIXIE*'s spatial frequency coverage includes the reionization peak of the predicted *B*-mode spectrum at $\ell \simeq 10$. This peak is unambiguously caused by primordial gravitational waves, and measurements of it are only accessible from a space platform (see Section 2.3 for more details).

The nominal *PIXIE* mission will last 4 years. In that time, *PIXIE* will map the full sky in Stokes *I*, *Q* and *U* with angular resolution of 2.65° and sensitivity of 70 nK per 1° square pixel. This sensitivity and resolution will be achieved in each of the instrument's 400 equally-spaced frequency channels, which span from 30 GHz to 6 THz.

2.2 Instrument description

Complete descriptions of the *PIXIE* instrument and certain subsystems (e.g., detectors, calibrator, concentrator horns, adiabatic demagnetization refrigerators) are available in the literature [52–54, 59–62], but in the following we describe some key elements that enable an understanding of the mission concept and instrument operation.

2.2.1 Spacecraft and Thermal Design

A diagram of the *PIXIE* spacecraft illustrating its layout and thermal design is shown in Figure 2.1. The FTS (outlined in red) operates at 2.725 K and the detectors operate at a base temperature of 100 mK. Nested sunshields first cool the instrument from the steady state temperature of 280 K to 150 K. A mechanical cryocooler further cools

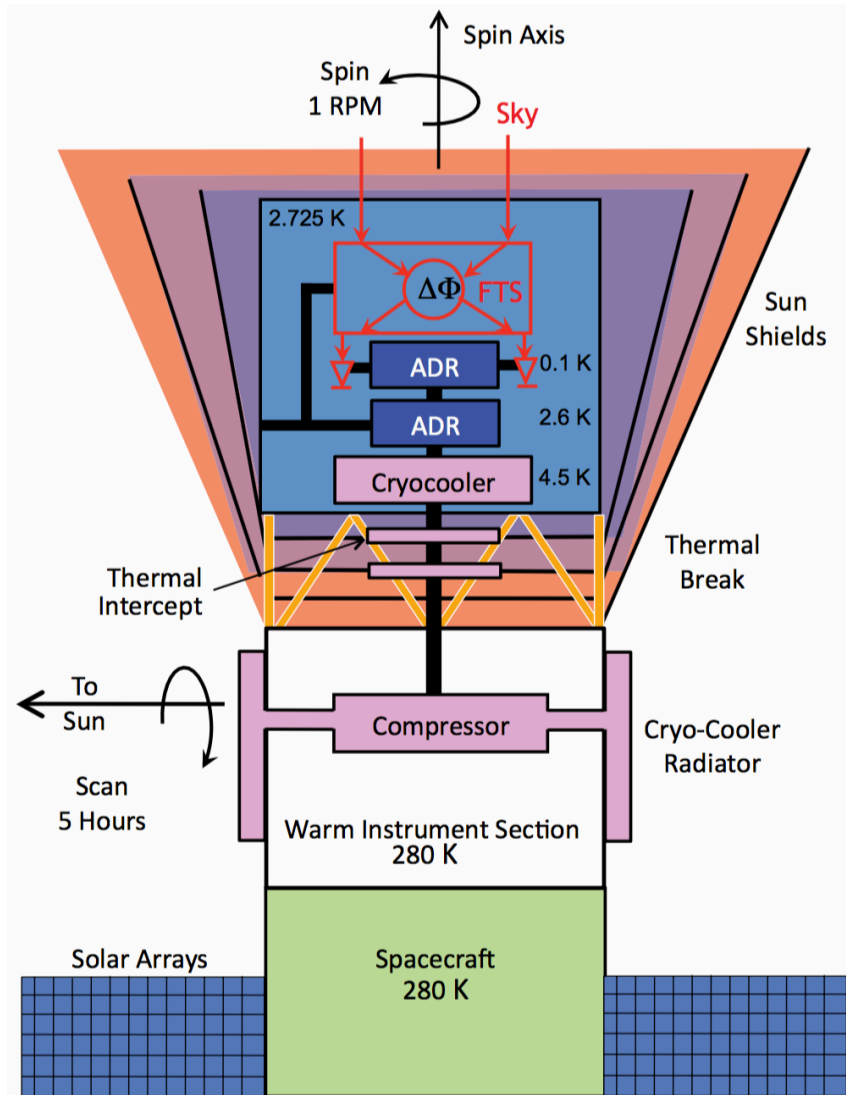


Figure 2.1 Layout of the *PIXIE* spacecraft. The spacecraft operates at 280 K. A series of sunshields provide passive cooling of the science instrument to 150 K. A mechanical cryocooler further cools the instrument to ~ 4 K. Finally, a series of adiabatic demagnetization refrigerators (ADRs) cool the instrument to 2.725 K and the detectors to 100 mK. Figure from [54].

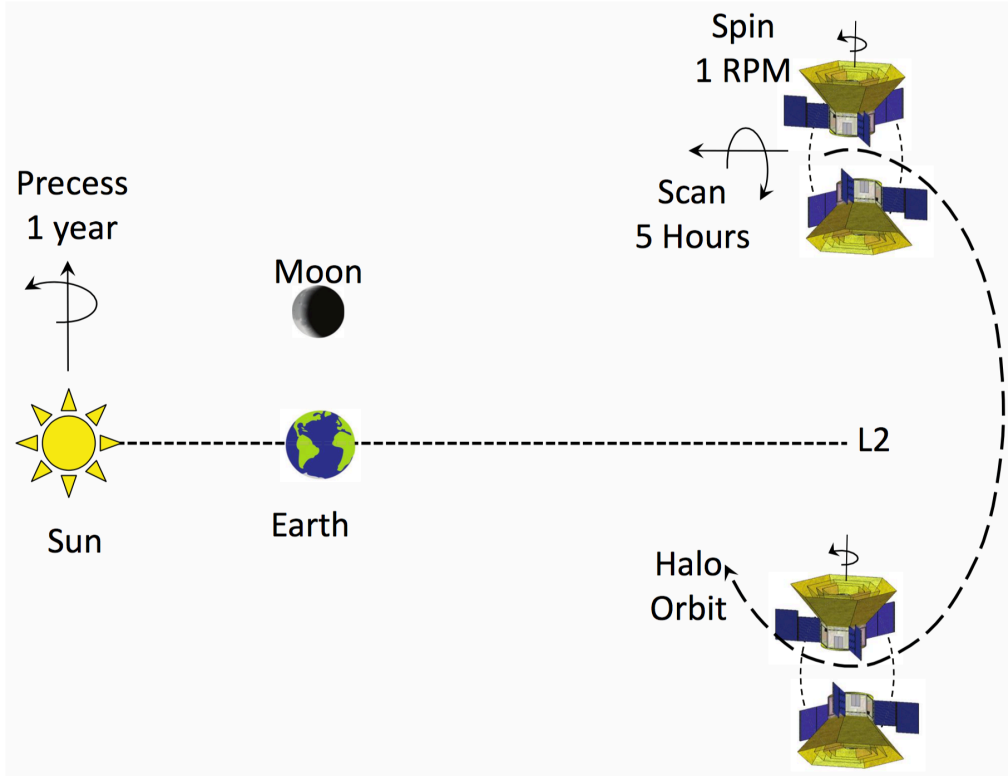


Figure 2.2 Illustration of *PIXIE*'s scan strategy. Because the beam axis spin is much faster than the scan, all sky pixels receive uniform coverage with respect to spin angle. Figure from [54].

the instrument from 150 K to 4 K. Finally, a series of adiabatic demagnetization refrigerators (ADRs) [62] cool the instrument from 4 K to 2.725 K, and the detectors from 2.725 K to 100 mK. The instrument spins about its vertical axis (see Figure 2.1) at ~ 1 rpm, rapidly interchanging (modulating) polarization directions incident on the detectors. The instrument also spins about the horizontal axis with a period of ~ 5 hours, scanning a great circle on the sky.

2.2.2 Scan strategy

PIXIE's scan strategy is summarized by Figure 2.2. The instrument traces a great circle on the sky every ~ 5 hours. It precesses $\sim 1^\circ$ per day, so the entire sky is mapped twice over the course of a year. An independent FTS measurement of a sky

pixel takes 1.5 seconds (the time it takes for the moving mirror to move from the null to the extreme of its stroke). Each pixel on the ecliptic is measured ~ 200 times before the scan moves to other pixels, and higher latitudes will get more measurements. This enables us to take sums and differences of measured signals under the reasonable assumption that the sky signal is constant, which plays an important role in mitigating systematic effects. Of key importance is that there are many different modulation timescales, each corresponding to a natural Fourier transform of the data. All sky frequencies are modulated by the moving mirror every few seconds. The fringe pattern is amplitude modulated by the spacecraft spin every minute. Repeated measurements of sky pixels occur every few hours. The instrument orbits the sun once every year. Because the Fourier transform is a linear operation, any Fourier transform can be performed in any order. As will be discussed in Chapter 3, this significantly simplifies systematic error mitigation on the instrument, allowing efficient separation of sky signals and instrumental artifacts. Further discussion of the *PIXIE* scan strategy is given by [63].

2.2.3 Optics

PIXIE's science instrument is a polarizing FTS with 14 optical surfaces per left or right beam. A cartoon of the instrument is shown in Figure 2.3, and complete descriptions of the optical design are given by [52–54]. Light incident on the left or right side (denoted “A” or “B” side, respectively) of the instrument is routed into the FTS. Polarizer A defines the polarization basis of the instrument, transmitting one polarization and reflecting the orthogonal polarization. The polarization angle of the instrument will be measured on the ground and calibrated in flight by observing a well-known polarized sky source [e.g., 64]. Polarizer B is oriented at 45 degrees relative to polarizer A, mixing the beams. The moving mirror injects an optical phase delay in the two beams, which are subsequently combined by polarizer C and sorted

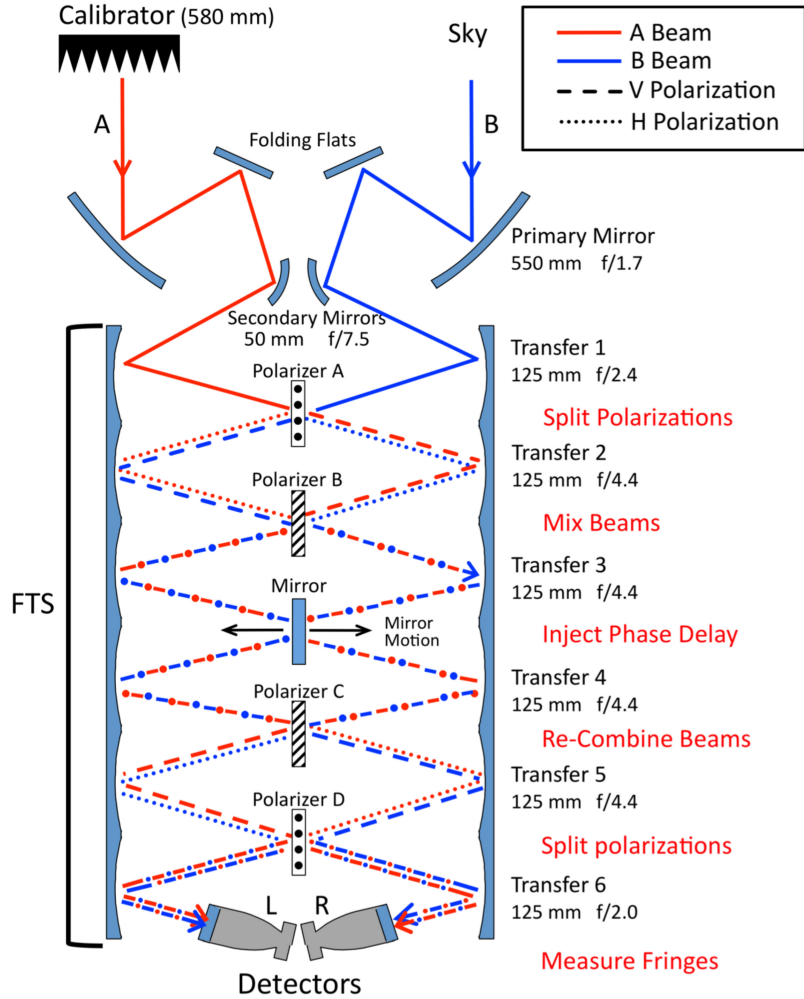


Figure 2.3 Cartoon of the *PIXIE* FTS. The listed dimensions give the diameters of components. The calibrator can block either beam or be stowed. The beams are co-aligned. Polarizers A and D are oriented with their grids vertical, transmitting horizontal (\hat{x}) polarization and reflecting vertical (\hat{y}) polarization. Polarizers B and C are oriented at 45 degrees relative to polarizers A and D. The mirror stroke is ± 2.6 mm, which corresponds to an optical path difference between beams of ± 10.0 mm. The mirror completes a stroke from $z = -2.7$ mm to $z = +2.7$ mm in 3 seconds. The optical path difference between beams ℓ is related to the frequency of incident radiation ν by the relationship $\ell = c/\nu$, where c is the speed of light. The frequency of the mirror movement ω is related to the frequency of incident radiation by $\omega = 4\nu v/c$, where v is the moving mirror's velocity. The CMB signal is largely confined to acoustic frequencies below 15 Hz. The dust signal is confined to acoustic frequencies below 100 Hz.

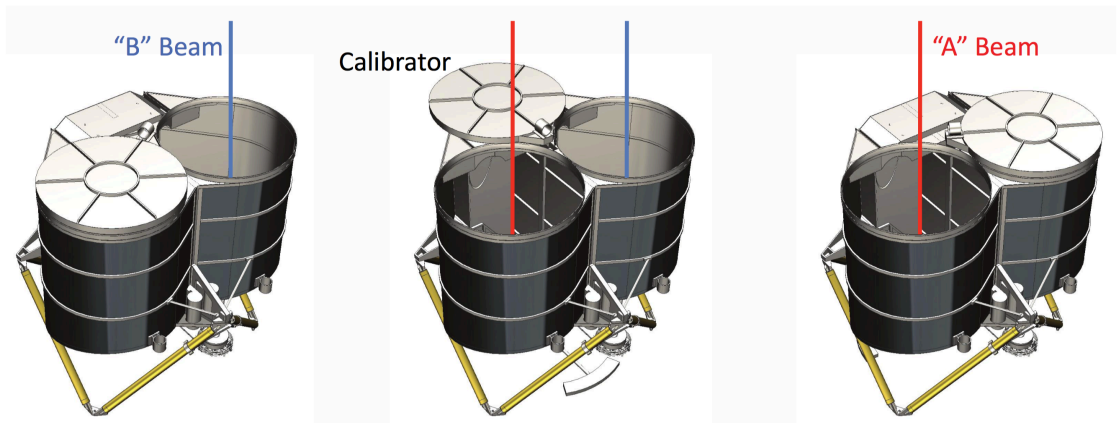


Figure 2.4 Schematic showing the possible positions of *PIXIE*'s external calibrator. It can block either beam or be stowed. When the calibrator blocks a beam, the instrument is in spectral mode. When it is stowed, the instrument is in polarization mode. Figure from [54]

by polarizer D. The light is then routed into the square receiver horns [61] and onto the focal planes. Each focal plane consists of two polarization-sensitive bolometers mounted back-to-back with their polarization axes orthogonal to each other, allowing simultaneous measurements of both polarizations.

Figure 2.4 shows an external schematic of the *PIXIE* FTS and the three positions of the full-aperture calibrator. The calibrator, which will be kept within a few mK of the CMB temperature, can block either beam or be stowed. Its temperature will be intentionally varied from ~ 2.72 K to ~ 2.73 K in order to measure the gain of the detectors and other parts of the instrument. It is comprised of a series of black cones. The calibrator enables absolute characterization of *PIXIE*'s optical efficiency and independent, non-differential measurements of each beam. When stowed, the instrument is in polarization mode and is sensitive only to Stokes Q and U (see Section 3.7 for a discussion of *PIXIE*'s sensitivity to Stokes V). When blocking a beam, the instrument is in spectral mode and is sensitive to Stokes I , Q and U . Some calibrator cones will have their temperatures raised to ~ 20 K in order to null the dust signal when in spectral mode. In addition to being modulated by the mirror

stroke, the targeted signals are also amplitude modulated by spacecraft spin. The nominal mission calls for the calibrator to be stowed 50% of the time and deployed 45% of the time. The remaining 5% includes high-temperature calibration of Galactic dust and lost observing time. Note that in spectral mode, *PIXIE* still has polarization sensitivity, but with half the signal-to-noise ratio (SNR) of polarization mode. We show this explicitly here.

Let light incident on the left side of the instrument be given by $E^L = \mathcal{A}\hat{x} + \mathcal{B}\hat{y}$, and light incident on the right side is represented by $E^R = \mathcal{C}\hat{x} + \mathcal{D}\hat{y}$. We can then solve for the power measured by each of the 4 detectors (see Chapter 3 for the details):

$$\begin{aligned}
\mathbf{P}_x^L &= \frac{1}{2} \int (\mathcal{B}^2 + \mathcal{C}^2) + (\mathcal{C}^2 - \mathcal{B}^2) \cos\left(\frac{4\nu z}{c}\right) d\nu, \\
\mathbf{P}_y^L &= \frac{1}{2} \int (\mathcal{A}^2 + \mathcal{D}^2) + (\mathcal{D}^2 - \mathcal{A}^2) \cos\left(\frac{4\nu z}{c}\right) d\nu, \\
\mathbf{P}_x^R &= \frac{1}{2} \int (\mathcal{A}^2 + \mathcal{D}^2) + (\mathcal{A}^2 - \mathcal{D}^2) \cos\left(\frac{4\nu z}{c}\right) d\nu, \\
\mathbf{P}_y^R &= \frac{1}{2} \int (\mathcal{B}^2 + \mathcal{C}^2) + (\mathcal{B}^2 - \mathcal{C}^2) \cos\left(\frac{4\nu z}{c}\right) d\nu,
\end{aligned} \tag{2.1}$$

where ν is the frequency of light, c is the speed of light, z is the moving mirror position, and the superscripts L and R , and subscripts x and y , indicate whether the power is measured by the left or right side \hat{x} or \hat{y} detector, respectively.

Each of the expressions in Equation 2.1 consists of a DC term and a term modulated by the movement of the mirror. We neglect the DC term (zeroth bin in the Fourier transform) because it may be unstable. The latter term is equal to the Fourier transform of the difference spectrum between orthogonal polarizations of light incident on the two sides of the instrument.

When we also include spacecraft rotation, it is necessary to transform from instrument-fixed to sky-fixed coordinates. We will do this first for the case where both beams are open to the sky. In this case, both beams are sampling the same electric field, so we

recognize that $\mathcal{A}\hat{x} = \mathcal{C}\hat{x}$ and $\mathcal{B}\hat{y} = \mathcal{D}\hat{y}$ ¹. Then the transformation from instrument-fixed to sky-fixed coordinates takes the following form:

$$\begin{aligned}\mathcal{A}\hat{x} &\rightarrow (\mathcal{A} \cos \gamma + \mathcal{B} \sin \gamma) \hat{x}', \\ \mathcal{B}\hat{y} &\rightarrow (\mathcal{B} \cos \gamma - \mathcal{A} \sin \gamma) \hat{y}',\end{aligned}\tag{2.2}$$

where (\hat{x}, \hat{y}) are instrument-fixed unit vectors, (\hat{x}', \hat{y}') are sky-fixed unit vectors, and γ is the spacecraft rotation angle.

Implementing this transformation, Equation 2.1 becomes

$$\begin{aligned}\mathbf{P}_x^L &= \frac{1}{2} \int (Q_{\text{sky}} \cos(2\gamma) + U_{\text{sky}} \sin(2\gamma)) \cos\left(\frac{4\nu z}{c}\right) d\nu, \\ \mathbf{P}_x^L &= \frac{1}{2} \int (-Q_{\text{sky}} \cos(2\gamma) - U_{\text{sky}} \sin(2\gamma)) \cos\left(\frac{4\nu z}{c}\right) d\nu, \\ \mathbf{P}_x^L &= \frac{1}{2} \int (Q_{\text{sky}} \cos(2\gamma) + U_{\text{sky}} \sin(2\gamma)) \cos\left(\frac{4\nu z}{c}\right) d\nu, \\ \mathbf{P}_x^L &= \frac{1}{2} \int (-Q_{\text{sky}} \cos(2\gamma) - U_{\text{sky}} \sin(2\gamma)) \cos\left(\frac{4\nu z}{c}\right) d\nu,\end{aligned}\tag{2.3}$$

where Q_{sky} and U_{sky} are the Stokes Q and U parameters of the sky, given by $\langle \mathcal{A}^2 - \mathcal{B}^2 \rangle$ and $2 \text{Re} \langle \mathcal{A}\mathcal{B} \rangle$, respectively. For clarity, we ignore the DC (unmodulated) terms, which show up in the zeroth bin of the Fourier transform. Linearly polarized sky light described by the Stokes parameters Q and U is amplitude modulated at twice the spacecraft's spin frequency. Any signal that is not amplitude modulated at twice the rotation frequency is not from a polarized sky source.

This exercise can be repeated for the case where one beam is blocked by the calibrator. There is no coordinate transformation for light emitted by the calibrator; its coordinates are always instrument-fixed. In this case, the measured signals are given by

¹This is not strictly true. In Section 3.7, we treat *PIXIE* as a two-element radio array, taking into account the different paths light must travel from an distant source to each of the two beams.

$$\begin{aligned}
\mathbf{P}_x^L &= \frac{1}{4} \int (I_{\text{sky}} - I_{\text{cal}} + Q_{\text{sky}} \cos(2\gamma) + U_{\text{sky}} \sin(2\gamma)) \cos\left(\frac{4\nu z}{c}\right) d\nu, \\
\mathbf{P}_x^L &= \frac{1}{4} \int (I_{\text{sky}} - I_{\text{cal}} - Q_{\text{sky}} \cos(2\gamma) - U_{\text{sky}} \sin(2\gamma)) \cos\left(\frac{4\nu z}{c}\right) d\nu, \\
\mathbf{P}_x^L &= \frac{1}{4} \int (I_{\text{cal}} - I_{\text{sky}} + Q_{\text{sky}} \cos(2\gamma) + U_{\text{sky}} \sin(2\gamma)) \cos\left(\frac{4\nu z}{c}\right) d\nu, \\
\mathbf{P}_x^L &= \frac{1}{4} \int (I_{\text{cal}} - I_{\text{sky}} - Q_{\text{sky}} \cos(2\gamma) - U_{\text{sky}} \sin(2\gamma)) \cos\left(\frac{4\nu z}{c}\right) d\nu,
\end{aligned} \tag{2.4}$$

where Stokes I is the modulus of the \hat{x} and \hat{y} electric fields for the calibrator or sky. Polarized signals are modulated by the spacecraft rotation, but as expected they show up at half the intensity as when both sides of the instrument are open to the sky. The unmodulated component of the signal is equal to the intensity difference between the sky and the calibrator. If both were perfect blackbodies, this term would average to zero over the course of the mission, so long as the calibrator is on average isothermal with the sky. We enforce this; the calibrator will spend an equal amount of time at temperatures hotter and colder than the CMB. But to the degree that the calibrator is black (expected to be > 65 dB [60]), this term is a measurement of spectral distortions to the CMB blackbody.

The FTS will be kept isothermal with the CMB to within a few mK, so to first order any sky photon absorbed by the instrument will be replaced by an indistinguishable photon emitted by the instrument. We will actively control and asynchronously modulate the temperature of each surface in the FTS about the CMB temperature. The modulations will have periods of a few hours and will be nearly mutually orthogonal. Their amplitudes will vary, but will never exceed a few mK. This enables significant control over systematic effects (see Chapter 3).

The low frequency response of the instrument is limited by the etendue. Specifically there is a low frequency cutoff at 15 GHz imposed by the physical size of the detector. This is reinforced by the maximum scan length which limits the resolution

to ~ 15 GHz and thus all of the power below ~ 30 GHz is pushed into inaccessible bins in the Fourier transform.

The highest frequency is limited by the spacing on the wire grids. A filter (or series of filters) will be included to limit the input and hence noise from frequencies greater than ~ 5 THz. These are further limited by the finite response time of the bolometers.

The response of the instrument will not be uniform over all frequencies but this is calibrated by observing the changing temperature of the calibrator.

2.2.4 Detectors

PIXIE's multimode “lightbucket” design enables background-limited sensitivity with four polarization-sensitive bolometers based on silicon thermistors. The condition for background-limited sensitivity is for photon noise at the detector to dominate other detector noise sources. The electrical photon noise equivalent power (NEP) of a bolometer is given by

$$\text{NEP}_{\text{photon}}^2 = 4 \frac{A\Omega}{c^2} \frac{(k_B T_s)^5}{h^3} \int \frac{x^4 dx}{e^x - 1} \left(1 + \frac{\alpha \epsilon f}{e^x - 1} \right) (\alpha \epsilon f), \quad (2.5)$$

where A is the area of the detector, Ω is the solid angle of the detector, c is the speed of light, T_s is the temperature of the source, α is the detector absorptivity, ϵ is the emissivity of the source, f is the transmissivity of the optical system, and $x = h\nu/k_B T$ [65]. *PIXIE* achieves background-limited sensitivity by keeping other bolometer noise components small (e.g., phonon noise, amplifier noise, Johnson noise), while maximizing the photon noise term by making the the detector's etendue $A\Omega$ as large as possible given constraints on detector thermalization (limits A) and desired angular resolution on the sky (limits Ω).

A cartoon of a single *PIXIE* bolometer is shown in Figure 2.5 and a cartoon of

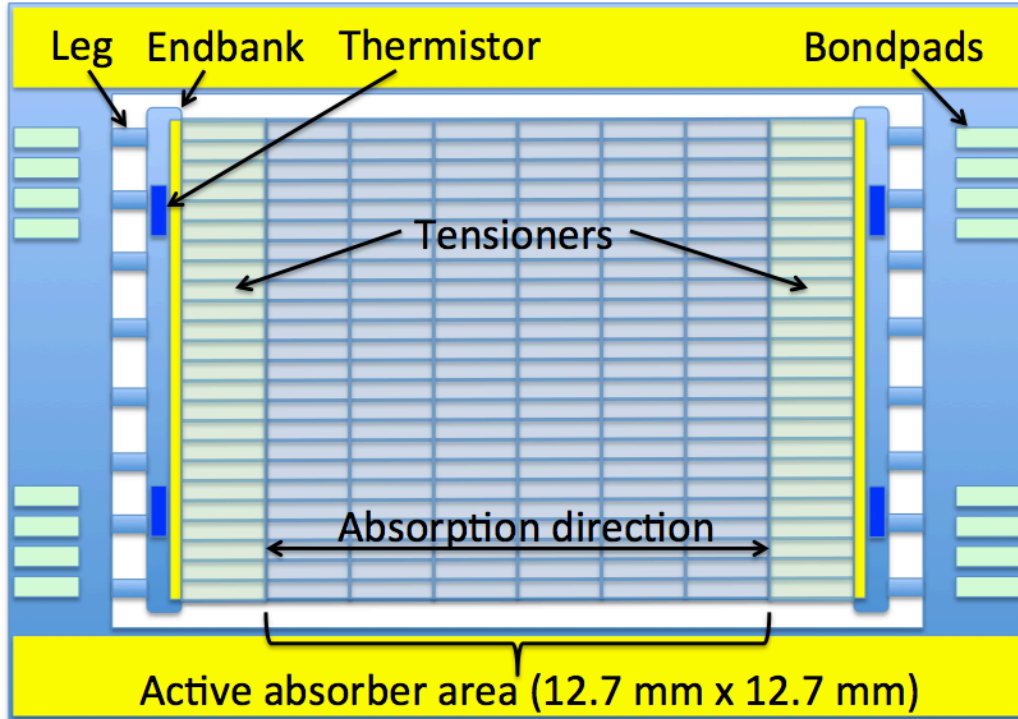


Figure 2.5 Cartoon of a single *PIXIE* bolometer. Degenerately doped wires of single-crystal silicon absorb a single linear polarization along the indicated direction of absorption. Undoped support beams orthogonal to the direction of light absorption provide mechanical support while contributing a negligible cross-polar response. The response time of the detector is driven by the heat capacity C of the endbank’s gold thermalization bar and the effective thermal conductance G_e (which accounts for electrothermal feedback gain) of the silicon legs between the endbank and the chip frame. These can be independently tuned.

a hybridized pair of bolometers is shown in Figure 2.6. A brief discussion of the detector operation is presented here, but a full treatment of their design, fabrication, and operation is presented in Chapter 4. Light incident on the detectors is absorbed in a thin degenerately-doped silicon layer in the absorber area. The absorbed light is converted to heat (phonons), which thermally diffuse out of the absorber area and into the gold thermalization bars positioned on each endbank. The thermalization bars in turn heat up and emit phonons that are subsequently absorbed by the doped silicon thermistors. The thermistors are also located on the endbanks. Absorption of phonons emitted by the gold increases the temperature of the thermistors, decreasing

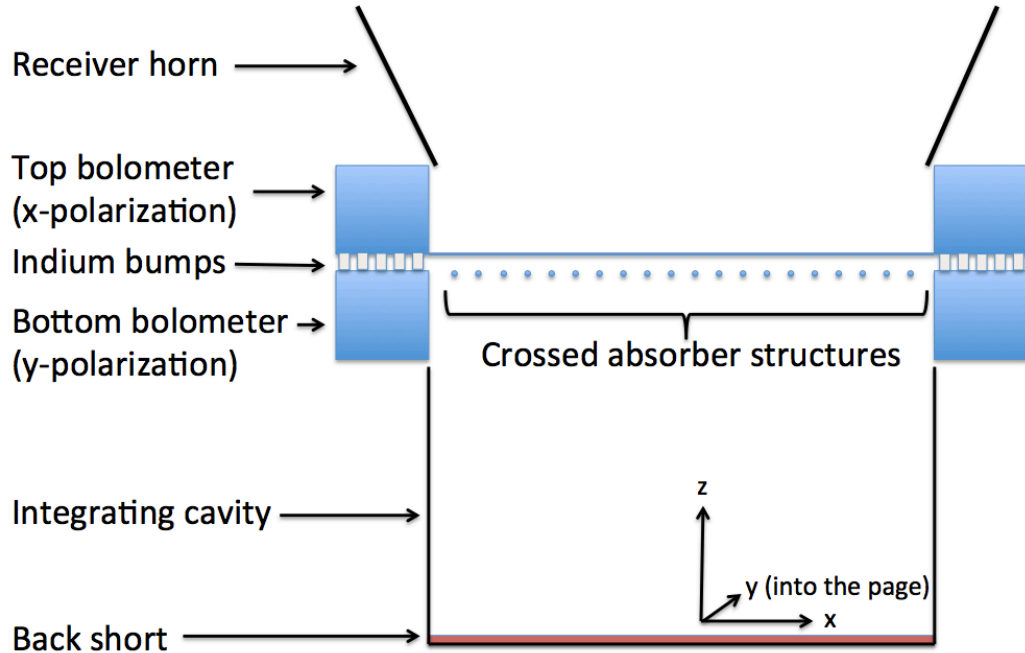


Figure 2.6 Cartoon showing a profile view of a hybridized pair of *PIXIE* bolometers. With indium bumps the pair of chips will be stood off from each other by $< 20 \mu\text{m}$, so the detectors will be sampling orthogonal polarizations of nearly the same electric field. The back short depth is designed to be $\sim \lambda/4$ at 270 GHz. Its depth is greatly exaggerated in the figure. It is important to note that light is incident on the strings from 2π sr, so there are no interference nulls that would occur were the light normally incident.

their resistance. Under current bias, the resistance change of the thermistors is sensed by a series of ultra-low-noise voltage amplifiers. The *PIXIE* detectors can be read out with a total of 8 wires (2 per detector). This is a factor of 1000 fewer than required of an imager with similar sensitivity and etendue.

2.3 Science goals

In terms of both sensitivity (~ 70 nK rms) and frequency coverage (30 GHz – 6 THz in 400 channels), *PIXIE* will enable unprecedented measurements of CMB polarization, spectral distortions to the CMB blackbody, and galactic foregrounds. In the following, we introduce the key science goals of *PIXIE* with a discussion of the

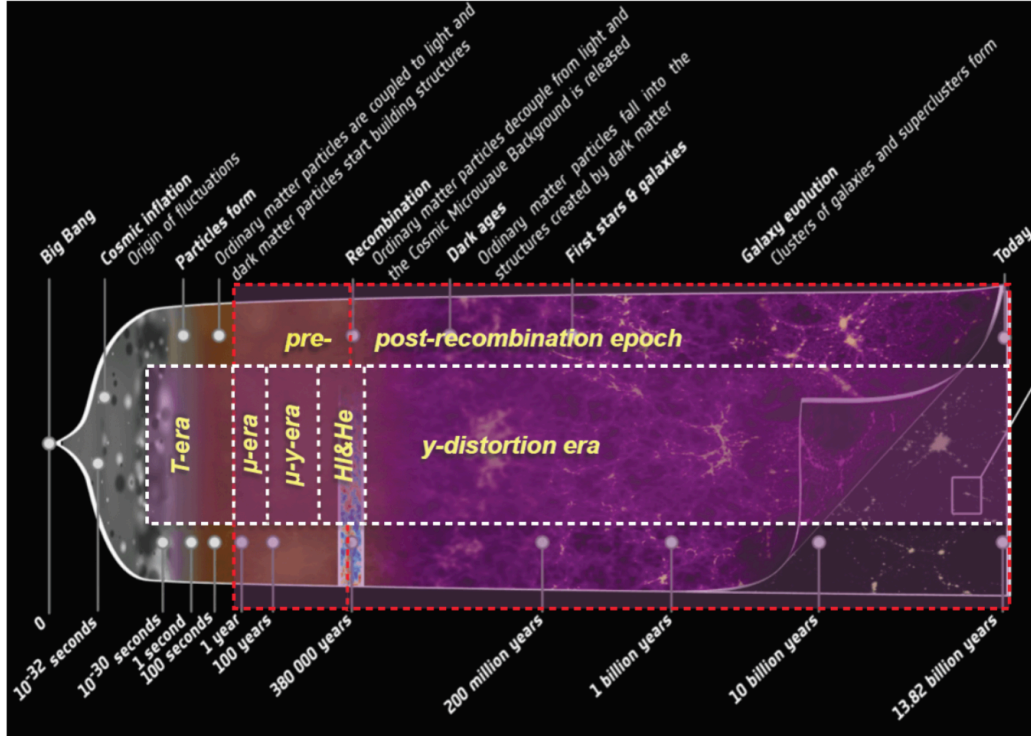


Figure 2.7 Thermal history of the universe, highlighting the science accessible to *PIXIE*. Figure from [56].

theoretical and experimental results that motivate the instrument. The thermal history of the universe and an introduction to the CMB is presented in Section 2.3.1. CMB polarization is discussed in Section 2.3.2, distortions to the CMB blackbody are discussed in Section 2.3.3, and galactic foregrounds are discussed in Section 2.3.4.

2.3.1 The cosmic microwave background

Figure 2.7 illustrates the thermal history of the universe. Immediately after the Big Bang, the universe is predicted to have undergone a rapid period of expansion known as inflation [66]. Inflation provides a simple explanation for many observables in the universe. First is the “horizon problem.” The universe is remarkably uniform, even in patches of sky that cannot be causally connected by signals moving at the speed of light. Under inflation, where the metric describing the universe expands much faster than the speed of light, now-disparate patches of sky were once in causal con-

tact. Next there is the “flatness problem.” Measurements show that the universe is flat (i.e., its geometry is Euclidian). Without inflation flatness changes with time, and we just happen to live in a flat universe; very specific initial conditions give rise to what we observe today. With inflation, however, the universe has always been flat, no tightly-constrained initial conditions required. Finally there is the “magnetic monopole problem.” Under grand unified models of particle physics, the initial conditions of the universe would give rise to a large number of heavy magnetic monopoles, about 10^{14} times more than current observational limits [66]. An initial period of inflation also mitigates the magnetic monopole problem. It should be noted that a number of other theories can also yield the same observables [e.g., 67, and references therein]. The theory of inflation, however, gives rise to a very specific observable in the polarization of the CMB (discussed in Section 2.3.2).

A few minutes after the Big Bang, as the universe continued to expand, particles formed. Ordinary matter particles (protons, electrons, and nuclei of deuterium, lithium, helium) were strongly coupled to photons in a hot plasma. Gravitational wells caused by perturbations imprinted during inflation led to anisotropy in the density of the universe. Harmonic acoustic waves, caused by the interaction of over and under-dense regions, propagated through the plasma. Dark matter particles condensed in the dense regions and began to form structure. A number of scattering processes led to distortions of the plasma’s Planck spectrum (see Section 2.3.3). Non-thermal radiation was emitted as isotopes of helium and hydrogen underwent atomic transitions.

About 380,000 years after the Big Bang, the universe had sufficiently expanded and cooled for photons to decouple from ordinary matter. At this time the radiation temperature is $\sim 1/4$ eV, where hydrogen can deionize in the primordial energy environment. Neutral elements formed in a process called recombination, and the radiation has traveled (almost) freely since. Known as the “surface of last scattering,”

the CMB that we observe today is a snapshot of this epoch. The last few scattering events experienced by the photons lead to the polarization that is measured today. The propagating acoustic modes at the surface of last scattering lead to the harmonic peaks in the angular power spectrum that are observed today. Over- and under-dense regions at the surface of last scattering leave their signature on the CMB as regions of slightly colder or hotter temperature.

After recombination, the universe underwent a “dark” period where radiation and matter remained decoupled. Regular matter condensed in gravitational wells formed by dark matter and large scale structure formed. Eventually the first stars and galaxies formed, and the universe reionized. Since this stage, matter has again interacted with CMB photons. Several resultant effects are measurable.

First, there is the Sunyaev-Zel’dovich (S-Z) effect, where CMB photons are up-scattered by energetic electrons in clusters of galaxies [68]. The S-Z effect makes detailed predictions about the energy increase of CMB photons after scattering, and also the perturbations to the CMB angular power spectrum. Several experiments have mapped the S-Z effect and used the results to probe cluster physics [43, 44, 69].

Another physical mechanism that affects the CMB radiation we observe is the integrated Sachs-Wolfe (ISW) effect [9]. The ISW effect refers to the redshift experienced by CMB photons when they travel through gravitational wells associated with large scale structures (LSS). The physics of ISW effect is the same whether it takes place at late times or in the primordial plasma. In order to distinguish the two, measured maps of the CMB are cross-correlated with maps of LSS [e.g., 70].

Interactions between CMB photons and LSS also affect the polarization of the CMB. This is discussed in more detail in Section 2.3.2, but gravitational lensing of CMB photons by LSS can convert spatial polarization patterns from even to odd parity modes. The effect of lensing is most important at smaller angular scales ($\ell > 100$), so its spectral content allows it to be distinguished from primordial polarization signals.

2.3.2 Polarization

CMB polarization results when a quadrupole anisotropic radiation field is Thomson scattered by free electrons. When an isotropic field is scattered, there is no net polarization. The polarization that is detected today was generated at the surface of last scattering ($z \simeq 1100$) or during reionization ($z \simeq 11$). Polarization induced by earlier scattering events is lost by subsequent re-scattering. We first provide the mathematical machinery for understanding polarization of the CMB, following the conventions of [47]. We then introduce the physical implications of the polarized field.

A linearly-polarized radiation field can be described by its 2×2 coherency matrix $I_{ij}(\hat{n})$, given by

$$I_{ij}(\hat{n}) = \begin{bmatrix} \langle E_1 E_1^* \rangle & \langle E_1 E_2^* \rangle \\ \langle E_1^* E_2 \rangle & \langle E_2 E_2^* \rangle \end{bmatrix}, \quad (2.6)$$

where \hat{n} is some direction on the sky, and E_1 and E_2 are electric field amplitudes in the direction of some orthogonal basis vectors \mathbf{e}_1 and \mathbf{e}_2 , respectively, and the angle brackets indicate a time average [71]. The linear polarization state of the field described by $I_{ij}(\hat{n})$ is given by the Stokes parameters $Q(\hat{n})$ and $U(\hat{n})$, where $Q(\hat{n}) = \frac{1}{4}(I_{11}(\hat{n}) - I_{22}(\hat{n}))$ and $U(\hat{n}) = \frac{1}{4}(I_{12}(\hat{n}) + I_{21}(\hat{n}))$. The temperature of the field $T(\hat{n})$ is given by the trace of $I_{ij}(\hat{n})$.

The temperature of the field is invariant under rotations. Therefore on a sphere it can be expanded as a spin-0 (standard) spherical harmonic series, where

$$T(\hat{n}) = \sum_{\ell, m} a_{\ell m} Y_{\ell m}(\hat{n}). \quad (2.7)$$

The spin-0 spherical harmonic transform of the *Planck* satellite's temperature measurements is shown in Figure 1.2.

$Q(\hat{n})$ and $U(\hat{n})$ depend on the orientation of the unit vectors \mathbf{e}_1 and \mathbf{e}_2 on the

sky. We are free to express $Q(\hat{n})$ and $U(\hat{n})$ as the independent linear combinations $(Q + iU)(\hat{n})$ and $(Q - iU)(\hat{n})$. In this case, the transformations under rotation take the following form:

$$(Q \pm iU)(\hat{n}) \rightarrow \exp(\mp 2i\phi) (Q \pm iU)(\hat{n}), \quad (2.8)$$

where ϕ is the rotation angle. $Q(\hat{n})$ and $U(\hat{n})$ transform under rotations about \hat{n} as spin-2 spherical harmonics with spin weights ± 2 , respectively (see [72]). Then they may be expressed as

$$\begin{aligned} (Q + iU)(\hat{n}) &= \sum_{\ell, m} a_{\ell m}^{(+2)} {}_{(+2)}Y_{\ell m}(\hat{n}), \\ (Q - iU)(\hat{n}) &= \sum_{\ell, m} a_{\ell m}^{(-2)} {}_{(-2)}Y_{\ell m}(\hat{n}), \end{aligned} \quad (2.9)$$

where the factors ± 2 indicate the spin weights.

A fundamental property of spin-weighted spherical harmonics is that their spin state can be raised or lowered by applying raising and lowering operators. When applied to the expressions given by Equation 2.9, it is possible to express the polarized field as spin-0 spherical harmonics, which are independent of the choice of coordinates (see [47] for a derivation). The field is then described by

$$\begin{aligned} E(\hat{n}) &= \sum_{\ell, m} a_{\ell m}^E Y_{\ell m}(\hat{n}), \\ B(\hat{n}) &= \sum_{\ell, m} a_{\ell m}^B Y_{\ell m}(\hat{n}), \end{aligned} \quad (2.10)$$

where the coefficients $a_{\ell m}^E$ and $a_{\ell m}^B$ given by linear combinations of the spin-2 coefficients:

$$\begin{aligned} a_{\ell m}^E &= -\frac{1}{2} \left(a_{\ell m}^{(+2)} + a_{\ell m}^{(-2)} \right), \\ a_{\ell m}^B &= -\frac{1}{2i} \left(a_{\ell m}^{(+2)} - a_{\ell m}^{(-2)} \right). \end{aligned} \quad (2.11)$$

The so-called E and B -mode polarization fields given by Equations 2.10 and 2.11 completely specify the polarization properties of the coherency matrix. Of critical importance is that the E and B -mode fields, while rotationally invariant, are of even and odd parity, respectively; therefore they can be distinguished observationally by their distinct spatial signatures.

The characteristics of the incident radiation field $Y_{\ell=2}^{m=0,\pm 1,\pm 2}$ determine the spatial signature of the resultant polarization. The scalar $m = 0$ mode gives rise to an E -mode contribution. The $m = 0$ mode results from temperature anisotropies in the primordial plasma. The vector $m = 1$ mode corresponds to vorticity in the primordial plasma. It can produce a B -mode polarization signal, but its contributions are not important at the surface of last scattering. Vorticity does not lead to density anisotropies and is therefore dampened by the expansion of the universe. The tensor $m = 2$ mode gives rise to both E -mode polarization and B -mode polarization. The tensor mode is caused by gravitational waves generated during inflation. Propagating gravitational waves perturb the radiation field as a differential redshift, which is manifested as an $m = 2$ mode. Only the $m = 2$ mode can give rise to the B -mode polarization signal of the CMB at the surface of last scattering. As a result, its detection would provide strong evidence for inflation.

The amplitude of the predicted B -mode signal is determined by the energy scale of inflation V , where

$$V^{1/4} = 1.06 \times 10^{16} \text{ GeV} \left(\frac{r}{0.01} \right)^{1/4}, \quad (2.12)$$

and r is the tensor-to-scalar ratio, defined as the power ratio of gravitational wave to density (temperature) perturbations in the primordial plasma [73]. As a result, a measurement of the B -mode amplitude is a direct probe of the energy scale of inflation. Measurements today have only put upper limits on r . The best upper-limit

constraint on r is $r < 0.12$, which was determined by joint analysis of data from the ground-based *BICEP-2* experiment and the space-based *Planck* experiment [57].

2.3.3 Spectral distortions

As shown in Figure 1.1, the best measurements we have show that the CMB is a near-perfect blackbody. This spectrum was measured by the FTS-based *FIRAS* instrument that flew on the *COBE* satellite [5]. Combining the *FIRAS* results with a similar spectrum measured by the FTS-based *COBRA* sounding rocket experiment [7], we find that the CMB fits a Planck spectrum to 50 parts per million precision. *PIXIE* will be 1000 times more sensitive than *FIRAS* and therefore able to search for deviations from a Planck spectrum at the 50 parts per billion level. Many known astrophysical processes will generate spectral distortions at this level. These are described in this section, and more complete treatments are available in the literature [e.g., 74–77, and references therein]. We focus here on the spectral distortions that *PIXIE* is likely to detect based on known astrophysical processes.

2.3.3.1 Thermal distortions

Thermal spectral distortions are caused by the scattering of CMB photons by free electrons. At intermediate to late redshifts ($z < 10^4$), the dominant distortion mechanism is Compton scattering of CMB photons by thermal electrons. Known generally as “ y -distortions”, the resultant distortion to a Planck spectrum is described analytically by

$$\frac{\delta I}{I} = xy \frac{e^x}{e^x - 1} \left(\frac{x}{\tanh(x/2)} - 4 \right), \quad (2.13)$$

where $x = h\nu/k_bT$. The parameter y is given by

$$y = n_e \sigma_0 c H_0^{-1} \int \frac{k_b T(z)}{m_e c^2} \frac{(1+z)}{\sqrt{1+\Omega z}} dz, \quad (2.14)$$

where n_e and m_e are the electron density and mass, σ_0 is the Thomson cross section, c is the speed of light, and $T(z)$ is the radiation temperature.

Another type of distortion, known as “ μ -distortions”, occurs at earlier epochs ($z > 10^4$). μ -distortions result from multiple rapid scattering events that lead to kinetic equilibrium between electrons and photons. The resulting distorted Planck spectrum is given by

$$I_\nu = \frac{2h\nu^3}{c^2} \frac{1}{\exp(h\nu/k_B T - \mu) - 1}, \quad (2.15)$$

and is characterized by a chemical potential μ , given by

$$\mu = 1.4 \frac{\delta E}{E}, \quad (2.16)$$

where $\delta E/E$ is the fractional energy release.

Even earlier scattering events ($z \sim \text{few} \times 10^6$), combined with Bremsstrahlung and double Compton emission, are so rapid that distortions are averaged out, but they yield a net increase in the CMB temperature known as T -distortions. Pure y -distortions only occur near the epoch of recombination, and pure μ -distortions only happen when the primordial plasma is sufficiently dense. At intermediate times the distortions are characterized by a mixture of T , y and μ distortions. As a result, measurements of the distorted spectrum, and the relative fraction of T , y and μ -type distortions, are measurements of the energy release history of the early universe. This is illustrated by Figure 2.8.

2.3.3.2 Non-thermal distortions

Non-thermal processes can also lead to spectral distortions. Atomic transitions during the epoch of recombination ($10^3 < z < 10^4$), when neutral helium and hydrogen

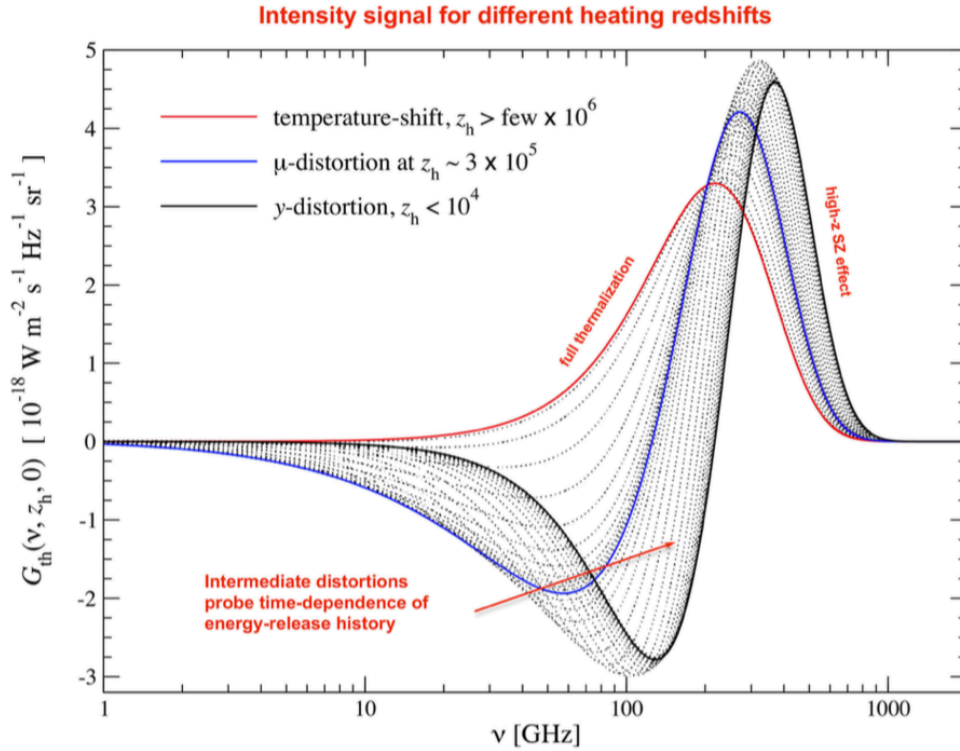


Figure 2.8 Relationship between distortions to the CMB blackbody and the energy release history of the early universe. At early times ($z > \text{few} \times 10^6$), there is a temperature shift. At intermediate times ($z \sim 3 \times 10^5$), distortions are pure μ -type. At later times ($z < 10^4$), the distortions are pure y -type. The signal we expect to measure is a superposition of all three; their relative abundances reveal the energy release history. Figure from [74].

formed from the primordial plasma, yield line distortions to the CMB blackbody. Radiation results from electrons transitioning from high energy states to the ground state, in particular $\text{HeIII} \rightarrow \text{HeII}$ at $z \simeq 5900$, $\text{HeII} \rightarrow \text{HeI}$ at $z \simeq 2000$, and $\text{HII} \rightarrow \text{HI}$ at $z \simeq 1300$ [76]. Figure 2.9 shows a calculated spectrum of recombination atomic lines that are detectable with *PIXIE*. Detection of these lines provides a measurement of the primordial helium abundance and probes physics of the primordial plasma before the surface of last scattering ($z \simeq 1100$).

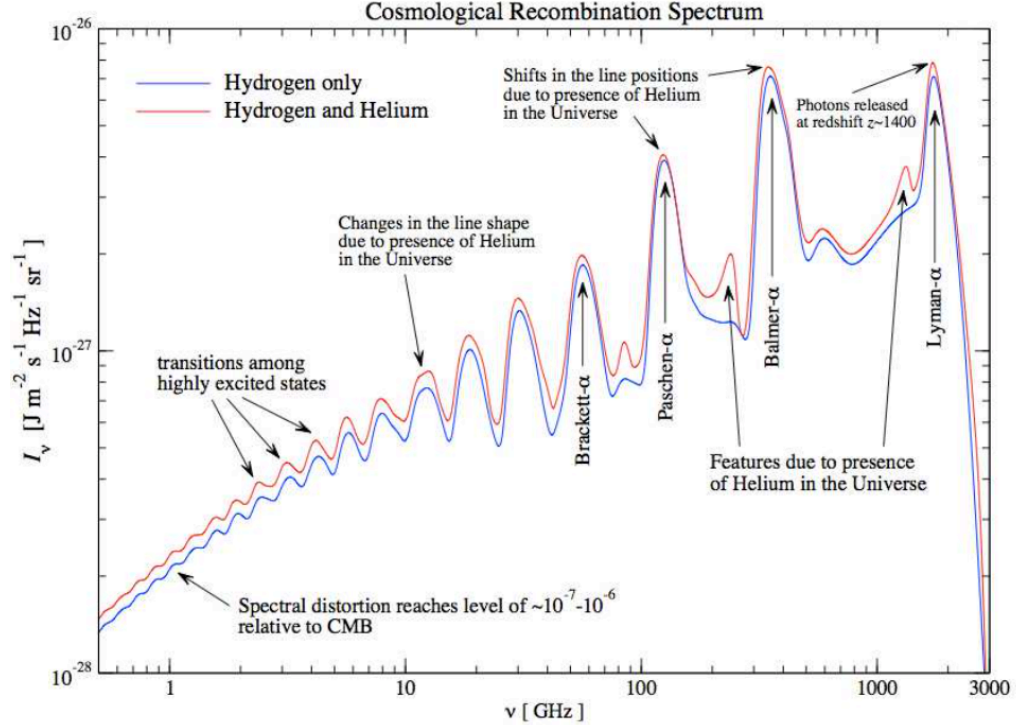


Figure 2.9 Line emission distortions to the CMB blackbody from atomic transitions during the epoch of recombination. Figure from [76].

2.3.4 Foregrounds

Polarized and unpolarized galactic foregrounds and their impact on CMB measurements are well treated in the literature. In this section, we examine the three dominant galactic sources of emission in the *PIXIE* band. At low frequencies, the foreground signal is dominated by synchrotron emission, which results from the acceleration of relativistic charged particles by the galactic magnetic field. Synchrotron radiation is inherently polarized; therefore it is an important signal that must be identified and removed when measuring CMB polarization. At high frequencies, the signal is dominated by thermal dust, which emits both polarized and unpolarized radiation. Present across the *PIXIE* band are molecular and atomic emission lines, which can simultaneously act as useful calibration sources and obscure measurements of the CMB. In this section, we discuss all three of these sources, including their physical

origin and the contributions that *PIXIE* can make to their understanding.

2.3.4.1 Synchrotron emission

Synchrotron radiation is caused by the acceleration of relativistic electrons by a magnetic field. The physics of galactic synchrotron radiation is well understood, with key results derived in detail by [78] and referenced by [79] and others. We reproduce some of these results here.

Synchrotron radiation is elliptically polarized, and total the emission spectrum of a single relativistic electron in a magnetic field is the sum of the parallel and perpendicularly polarized components:

$$P(\nu) = \frac{\sqrt{3}e^3 B \sin \alpha}{16\pi^2 \epsilon_0 c m_e} \frac{\nu}{\nu_c} \int_{\nu/\nu_c}^{\infty} K_{5/3}(\xi) d\xi, \quad (2.17)$$

where e is the charge of an electron, B is the magnetic field strength, α is the electron pitch angle, c is the speed of light, m_e is the mass of an electron, $K_{5/3}(\xi)$ is the modified Bessel function of order 5/3, and ν_c is the synchrotron critical frequency, defined by $\nu_c = 3eB\gamma^2/4\pi m_e c$ [78].

The result given by Equation 2.17 can be used to solve for the spectrum emitted by a distribution of relativistic electrons in a magnetic field. If we assume the electrons follow a power law energy distribution function $N(E)$, where $dN/dE = N_0 E^{-p}$, then the collective synchrotron emission spectrum is given by

$$P(\nu) = \frac{\sqrt{3}e^3}{8\pi m c^2} \left(\frac{3e}{4\pi m^3 c^5} \right)^{(p-1)/2} L N_0 B^{(p+1)/2} \nu^{-(p-1)/2} a(p), \quad (2.18)$$

where L is the length of the emitting volume along the observer's line-of-sight, and $a(p)$, given by [78], is approximately equal to 0.1 for typical values of p (see below). The assumption of a local power law dependence of the electron energy spectrum is motivated by observations [e.g., 80].

The local power law dependence p of the electron energy distribution yields a corresponding power law dependence $(p + 1) / 2$ of the spectrum of the electrons. Therefore measurements of the frequency dependence of the spectrum are also measurements of the local particle energy distribution and local magnetic field strength. These have been observed to vary across the sky [81].

The polarization fraction Π of synchrotron radiation perpendicular to a magnetic field line is given by $\Pi = (p + 1) / (p + 7/3)$ [82]. For a typical cosmic ray electron energy distribution ($p = 3$), $\Pi \sim 70\%$. In practice, however, Π measured by an observer is much lower ($< 40\%$) due to beam averaging, superposition of field directions, and Faraday rotation [82].

Synchrotron radiation can be removed from observations targeting the CMB because of its power law spectral content. With three frequency channels below ~ 60 GHz, where synchrotron emission dominates, *PIXIE* is better equipped to subtract the synchrotron signal than experiments with fewer low frequency channels [58]. Studies have also examined the angular power spectrum expected from diffuse synchrotron emission, providing an additional Fourier domain method to subtract synchrotron emission from CMB signals [e.g., 83].

2.3.4.2 Thermal dust

Emission from thermal dust dominates the foreground signal at frequencies higher than ~ 60 GHz. Thermal dust emission is dominated by large grains that are in thermal equilibrium with the local radiation field [84]. Thermal dust emission is partially polarized, with typical observed polarization percentages of $< 10\%$ [58]. The polarization arises from dust aligning with the local magnetic field. Largely based on observations by the *IRAS*, *COBE*, *WMAP*, and *Planck* satellites, several models have emerged that are used to describe the spectral content of thermal dust. The simplest empirical model, favored by the *Planck* experiment, consists of a single

modified blackbody spectrum where the dust intensity I_ν is given by

$$I_\nu = \tau_{\nu_0} \mathbf{B}_{\nu, T_{\text{obs}}} \left(\frac{\nu}{\nu_0} \right)^{-\beta_{\text{obs}}}, \quad (2.19)$$

where ν is frequency, τ_{ν_0} is the dust optical depth at a frequency ν_0 , $\mathbf{B}_{\nu, T_{\text{obs}}}$ is a Planck spectrum at an effective temperature T_{obs} , and β_{obs} is the modified blackbody spectral index. The *Planck* experiment used $T_{\text{obs}} = 23 \pm 3$ K and $\beta_{\text{obs}} = 1.55 \pm 0.1$. It should be noted that this is not a physical model, and it remains difficult to fit physical parameters even to the few parameters in this model.

More complicated models consist of two or more modified blackbodies at different temperatures, such as that proposed by [85]:

$$I_\nu = I_{\nu_0} \sum_n f_n \mathbf{B}_{\nu, T_n} \left(\frac{\nu}{\nu_0} \right)^{-\beta_n}, \quad (2.20)$$

where I_{ν_0} is the intensity measured at some reference frequency ν_0 , f is the fraction of dust along the line of sight that is at effective temperature T and whose spectrum is characterized by spectral index β . Multiple modified blackbody models (Equation 2.20) are intended to be more physical than single modified blackbody models (Equation 2.19). The superimposed spectrum at multiple temperatures is meant to account for different sized dust grains; smaller dust grains in thermal equilibrium with the local radiation field will be hotter than larger grains in the same field. Even so, the detailed relationships between fitted parameters and physical quantities remain unknown [84]. Dust models of intermediate complexity have also been employed [85].

For typical effective dust temperatures of between 15 K and 25 K, the spectrum measured by most CMB experiments is well within the Rayleigh-Jeans regime. As shown in Figure 2.10, this adds to the difficulty of discriminating between models and determining physical quantities from observed fit parameters, particularly when an experiment samples the dust spectra at just a few discrete frequencies. This

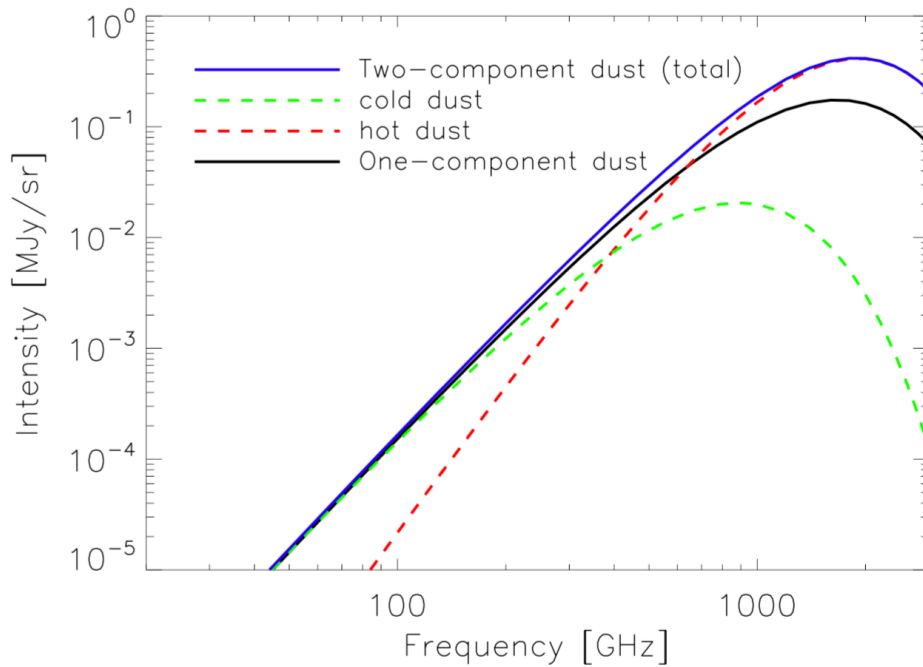


Figure 2.10 Comparison of single modified blackbody and multiple modified blackbody dust models. In the Rayleigh-Jeans regime, the models agree well. Only near the peak of the spectrum do they diverge. Figure from [58].

problem has been examined by [58, 86] and others. In [58], the authors find that substantial bias in measurements of CMB polarization can occur if incorrect models of thermal dust are employed. Likewise in [86], the authors reach similar conclusions but point out that sampling dust spectra at frequencies higher than its peak frequency substantially reduce the bias.

2.3.5 Line emission

PIXIE will be sensitive to emission lines from both atomic and molecular transitions across its bandwidth (see [53] for a comprehensive list of species detectable by *PIXIE*). In this section we focus on one of the more important sources of line emission, CO rotational transitions, due their brightness, potential to be polarized, spectral overlap with the CMB, and consequent ability to contaminate *PIXIE*'s polarization measure-

Line [$J_{\text{upper}} \rightarrow J_{\text{lower}}$]	Frequency [GHz]
1 \rightarrow 0	115.271
2 \rightarrow 1	230.538
3 \rightarrow 2	345.796
4 \rightarrow 3	461.041
5 \rightarrow 4	576.268
6 \rightarrow 5	691.473
7 \rightarrow 6	806.652
8 \rightarrow 7	921.799
9 \rightarrow 8	1036.912

Table 2.1 Rotational transition lines of ^{12}CO in the *PIXIE* bandwidth where contamination of CMB measurements is a concern (values from [87]).

ments. Other molecular lines (e.g., C+, N+ and O) may be brighter than CO at certain frequencies in the *PIXIE* band, but we consider CO as a representative case.

Measurements of CO line emission are powerful probes of the molecular component of the interstellar medium (ISM), as CO is both abundant and easily excited by collisions with other molecular components of the ISM [e.g., 87, and references therein]. CO emission is also a dominant cooling mechanism in molecular gas clouds; measurements of its structure are probes of turbulent clouds that can be regions of star formation. Beyond its inherent astrophysical significance, CO emission is an important foreground signal for CMB observations, both as a calibration source [e.g., 5] as a contaminant of CMB measurements.

Table 2.1 shows the transition number and emission frequency of the first nine ^{12}CO rotational transitions in the band from ~ 100 GHz to ~ 1 THz, where we are most concerned with foreground contamination of CMB measurements. The first three lines, centered at 115, 215, and 230 GHz, are the brightest; near the galactic plane CO emission accounted for a significant percentage of power measured by the

Planck experiment’s 100 GHz (50%), 217 GHz (15%), and 353 GHz (1%) channels [87]. The *Planck* experiment employed several algorithms to remove CO emission power from CMB maps; however particularly bright CO emission regions were masked due to concern about temperature-to-polarization instrumental systematics [88].

In addition, CO lines are expected to be polarized at the $\sim 1\%$ level [89, 90], thus their contribution to measurements of CMB polarization must be understood and quantified. This is particularly true away from the galactic plane where CO emission lines may be unresolved and current data are not sensitive enough to identify line emission sources. Recent work based on the *Planck* CO maps [90] suggests that unresolved line emission could yield a *B*-mode signal comparable in magnitude to an inflationary signal ($r = \text{few} \times 10^{-3}$) at intermediate angular scales ($\ell \sim 80$). CO emission is not expected to contaminate measurements at the largest angular scales, particularly near the reionization peak in the predicted *B*-mode spectrum. Therefore contamination of the form described by [90] is more likely to be a concern for ground and balloon-based experiments that cannot sample the low- ℓ modes.

2.3.6 Summary

PIXIE’s expected sensitivity, plotted in comparison to relevant astrophysical signals, is shown in Figure 2.11. Here we summarize the science contributions that *PIXIE* will make.

CMB polarization In polarization mode, *PIXIE* will have sufficient sensitivity and bandwidth to measure and subtract bright foreground signals at sub-percent accuracy. This opens a window to unambiguous measurements of the primordial *B*-mode signal at the largest angular scales, where *PIXIE* can make a detection for a tensor-to-scalar ratio $r < 4 \times 10^{-4}$ at 95% confidence. A detection of the *B*-mode signal, and the resultant understanding of the energy scales of the early universe,

will represent a significant theoretical and experimental achievement. *PIXIE* will also measure the E -mode polarization signal to limits imposed by cosmic variance. This measurement will probe the ionization history of the universe and yield a 3σ detection of the neutrino mass [54].

CMB spectral distortions In spectral mode, *PIXIE* will have the sensitivity and frequency coverage to measure the difference spectrum between the sky’s intensity spectrum the blackbody calibrator at nK-sensitivity, probing early universe physics that is otherwise inaccessible. These measurements will make tremendous contributions to our understanding of the early universe and its evolution from the primordial plasma to what we observe today. In particular, *PIXIE* will constrain y - and μ -type distortions to $|\mu| < 10^{-8}$ and $|y| < 2 \times 10^{-9}$, respectively. This will be a factor of 1000 improvement over the limits set by *FIRAS* [54].

Foregrounds *PIXIE* will make full sky maps of both polarized and unpolarized foregrounds at nK-scale sensitivity. Especially important are measurements of thermal dust that will extend to frequencies higher than the peak of the effective thermal emission spectrum, enabling refinement of existing models used to correct for the presence of dust in CMB maps. *PIXIE*’s foreground maps will be valuable for future CMB experiments that have fewer frequency channels but higher sensitivity per channel. Mapping of line emission in the Galaxy will also provide useful calibration for future experiments that make measurements in the *PIXIE* bandwidth.

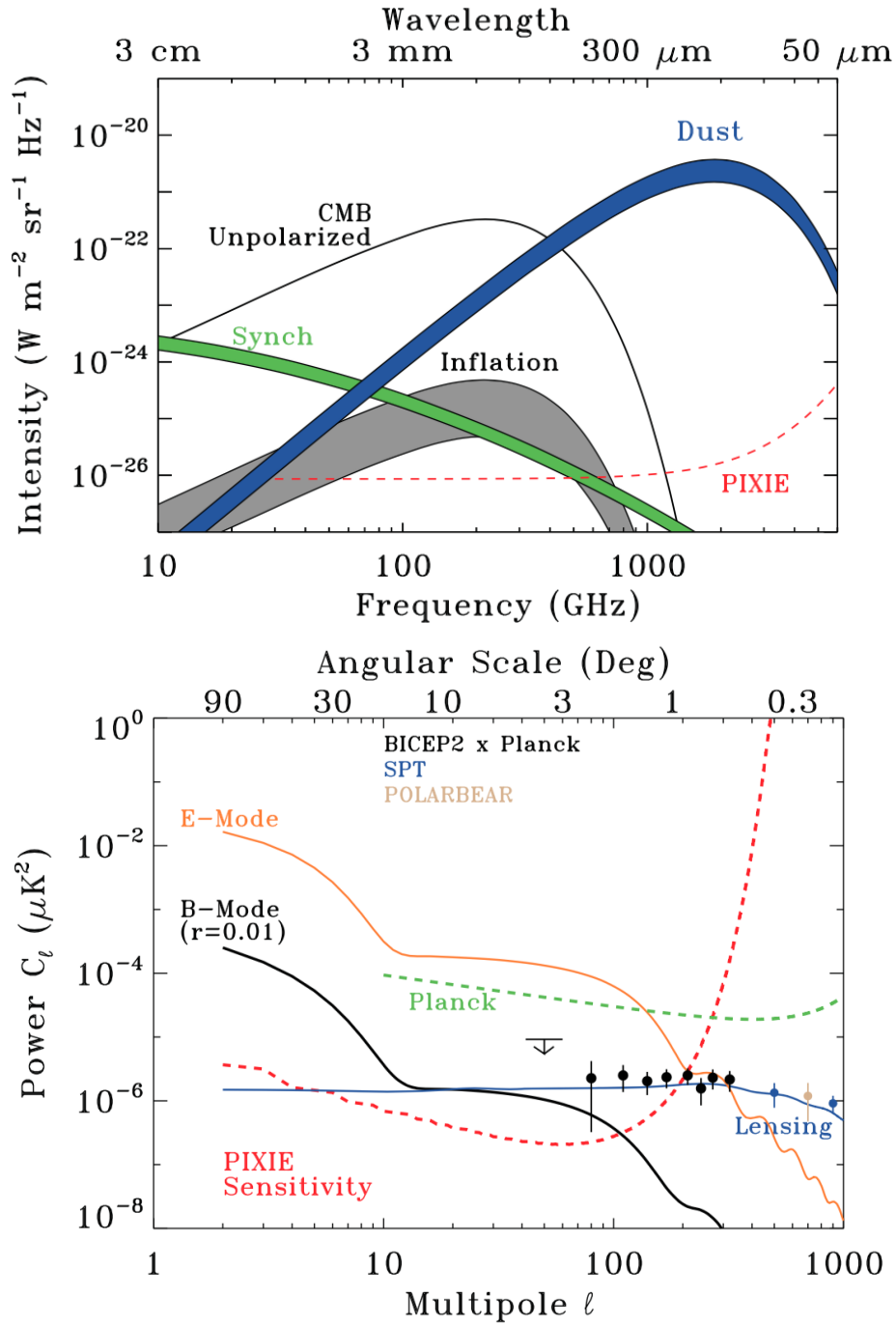


Figure 2.11 Summary of *PIXIE*'s sensitivity as a function of optical frequency (top) and spatial frequency (bottom). Shown are the target astrophysical signals and important polarized foregrounds which must be subtracted to the sub-percent level. *PIXIE* has the sensitivity to unambiguously detect the inflationary *B*-mode signal (gray shaded band in top figure) down to $r < 4 \times 10^{-4}$. This is enabled by the stability of a space platform, which allows access to the *B*-mode spectrum's reionization peak at $\ell \simeq 10$ (see bottom). Figure from [54].

Chapter 3

Instrumental systematic effects

3.1 Introduction

In this chapter, we present an analysis of instrumental systematic effects in polarizing Fourier transform spectrometers, using *PIXIE* as a worked example. This chapter is based on [91]. We analytically solve for the most important systematic effects inherent to the FTS - emissive optical components, misaligned optical components, sampling and phase errors, and spin synchronous effects - and demonstrate that residual systematic error terms after corrections will all be at the sub-nK level, well below the predicted 100 nK *B*-mode signal. This analysis focuses on instrument performance when operating in polarization mode, and error magnitudes are compared to the predicted *B*-mode signal. The results equally apply to spectral mode, though the instrument's sensitivity will be a factor of two worse.

To understand how systematic error is mitigated in an instrument like *PIXIE*, it is helpful to recall the measurement principle of a FTS. As a nulling interferometer, *PIXIE* is sensitive only to the difference between orthogonal polarizations of incident light. Therefore to the extent the CMB is a blackbody, and to the extent its optics are isothermal with the CMB, *PIXIE* will measure zero. The same concept applies

to systematic error sourced from imperfections in the *PIXIE* FTS. In general, the instrument is not sensitive to absolute non-idealities but instead to differential non-idealities between symmetrically positioned optical components.

The systematic effects treated are separated into several categories. The first, denoted emission errors, result from emissive optical components that absorb and emit radiation. These are discussed in Section 3.3. The second, denoted geometric errors, come about when a given optical component is not perfectly aligned, generally leading to reductions in optical efficiency. These are treated in Section 3.4. The third, denoted mirror transport mechanism (MTM) errors, result from systematic offsets and uncertainties in the moving mirror assembly’s position. We examine these in Section 3.5. Finally in Section 3.6 we consider spacecraft spin-synchronous effects, which can cause various instrumental drifts. For systematic errors of each kind, we solve for their analytic form, estimate their uncorrected magnitude, and subsequently show how they can be corrected to below 1 nK.

3.2 The ideal instrument

3.2.1 Jones matrix method

The optical layout of the *PIXIE* FTS is described in Section 2.2.3 and is shown in Figure 2.3. The Jones matrix method [92] is used to model the *PIXIE* FTS. Mathematically equivalent to either the Mueller matrix method [93] or the coherency matrix method [71], the Jones method assigns a 2×2 matrix operator \mathbf{J}_i to the i^{th} optical element in the signal path. Radiation incident on the i^{th} element is represented by the vector E_{i-1} , and the polarization state E_i after interaction with the optical element is given by

$$E_i = \mathbf{J}_i E_{i-1}. \tag{3.1}$$

Now we define the Jones operators that correspond to the ideal instrument's optical components, specifically mirrors, wire grid polarizers, and the moving mirror assembly. It is possible to define Jones operators in either the reference frame of the instrument or the reference frame of the radiation; we choose the latter. This choice does not affect the form of the resulting power expressions.

Reflections from a mirror flip the signs of the incident electric fields, but conserve power. Thus the corresponding Jones reflection operator is

$$\mathbf{J}_r = \begin{bmatrix} -1 & 0 \\ 0 & -1 \end{bmatrix}, \quad (3.2)$$

where the subscript r refers to reflections.

The wire grid polarizers transmit one polarization state while reflecting the orthogonal state. Thus each polarizer requires a Jones operator for both transmission and reflection. For a polarizer oriented such that \hat{x} polarization is transmitted and \hat{y} polarization is reflected, the corresponding Jones operators are

$$\begin{aligned} \mathbf{J}_t &= \begin{bmatrix} 1 & 0 \\ 0 & 0 \end{bmatrix}, \\ \mathbf{J}_r &= \begin{bmatrix} 0 & 0 \\ 0 & -1 \end{bmatrix}, \end{aligned} \quad (3.3)$$

where the subscripts t and r refer to transmission and reflection, respectively. When the polarizer is instead oriented at some angle θ about the \hat{z} -axis, which is the direction of light propagation, then the Jones operators $\mathbf{J}_t(\theta)$ and $\mathbf{J}_r(\theta)$ become

$$\begin{aligned} \mathbf{J}_t(\theta) &= \mathbf{R}_Z(\theta) \mathbf{J}_t \mathbf{R}_Z(\theta)^\dagger, \\ \mathbf{J}_r(\theta) &= \mathbf{R}_Z(\theta) \mathbf{J}_r \mathbf{R}_Z(\theta)^\dagger, \end{aligned} \quad (3.4)$$

where $\mathbf{R}_Z(\theta)$ is the rotation operator about the \hat{z} -axis.

Reflections from the moving mirror assembly insert phase delays and flip the sign of the \hat{y} polarization. The corresponding Jones operators are

$$\begin{aligned} \mathbf{J}_r^L &= \begin{bmatrix} \exp\left(\frac{2i\nu z}{c}\right) & 0 \\ 0 & -\exp\left(\frac{2i\nu z}{c}\right) \end{bmatrix}, \\ \mathbf{J}_r^R &= \begin{bmatrix} \exp\left(\frac{-2i\nu z}{c}\right) & 0 \\ 0 & -\exp\left(\frac{-2i\nu z}{c}\right) \end{bmatrix}, \end{aligned} \quad (3.5)$$

where ν is the frequency of light, z is the moving mirror position, and c is the speed of light. The superscripts L and R indicate whether light is incident on the mirror assembly from the left or right side, respectively.

3.2.2 Calculated signal

Light incident on the left side of the FTS is represented by $E^L = \mathcal{A}\hat{x} + \mathcal{B}\hat{y}$, and light incident on the right side is represented by $E^R = \mathcal{C}\hat{x} + \mathcal{D}\hat{y}$. The power measured by a single detector is then¹:

$$\mathbf{P}_x^L = \frac{1}{2} \int (\mathcal{B}^2 + \mathcal{C}^2) + (\mathcal{C}^2 - \mathcal{B}^2) \cos\left(\frac{4\nu z}{c}\right) d\nu, \quad (3.6)$$

where ν is the frequency of light, c is the speed of light, z is the moving mirror position, and the superscript L and subscript x indicate that the power is measured by the left side \hat{x} detector.

This expression contains a DC term and a term modulated by the movement of the moving mirror assembly. The latter represents the measured interferogram or fringe pattern, and it is proportional to the Fourier transform of the incident difference spectrum. Taking the inverse Fourier transform of the measured power gives the incident spectrum $\mathbf{S}_x^L(\nu)$. Up to some constant, it is given by

¹In general we only give the power measured by the left side \hat{x} detector, but similar expressions for signals measured by the other detectors are both available [52, 53] and readily worked out.

$$\mathbf{S}_x^L(\nu) = \mathcal{C}_\nu^2 - \mathcal{B}_\nu^2, \quad (3.7)$$

where the subscript ν indicates that we are working in the frequency domain.

The spectrum given by Equation 3.7 is equal to the Stokes Q parameter in instrument-fixed coordinates. This highlights the most critical aspect of *PIXIE*: the instrument is sensitive only to polarized sources. If the sky were unpolarized, *PIXIE* would measure no fringe pattern. Instead it only sees the difference spectrum between orthogonal polarizations of light incident on the two sides of the instrument. The symmetry of the *PIXIE* FTS ensures that nearly all systematic error terms are also proportional to differences.

3.3 Emission errors

In this section we introduce emission errors and see how associated systematic error terms propagate, are identified, and are corrected. Only non-ideal optical components upstream of polarizer B can yield error terms that are modulated by mirror movement. The moving mirror assembly will inject no phase delay in thermal photons emitted from polarizer B and beyond; therefore such non-ideal components will only serve to attenuate the sky signal.

To demonstrate how non-ideal components lead to modulated error terms, we consider the cases of emissive primary mirrors, emissive grids on polarizer A, and emissive non-optical surfaces, specifically the frames around the transfer mirrors. Emissive folding flats, secondary mirrors, and first transfer mirrors will give rise to systematic error terms identical in form to those from emissive primary mirrors, therefore we do not provide their derivations in this work.

To demonstrate how non-ideal components lead to attenuation of the sky signal, we model polarizer B's grids as emissive.

3.3.1 Review of theory

According to Kirchhoff's law of thermal radiation, the emissive power of a body is given by the product of its absorptance and the Planck formula:

$$\mathbf{E}_\nu = \alpha_\nu \mathbf{B}_{\nu,T}, \quad (3.8)$$

where \mathbf{E}_ν is the emission power spectrum, α_ν is the frequency-dependent absorptance spectrum (unitless), and $\mathbf{B}_{\nu,T}$ is the Planck spectrum with a temperature T .

For sufficiently thick optical surfaces, where power that is not reflected by the surface is absorbed, the reflectance ρ_ν is related to the absorptance by

$$\rho_\nu = 1 - \alpha_\nu. \quad (3.9)$$

At sufficiently low frequencies (e.g., the cutoff for gold is ~ 3.5 THz), the reflectance spectrum of metals is given by the Hagen-Rubins equation:

$$\rho_\nu = 1 - 2\sqrt{\frac{\nu}{\sigma_0}}, \quad (3.10)$$

where ν is the frequency of radiation, and σ_0 is the DC conductivity [94]. As a result, the absorptance spectrum is given by

$$\alpha_\nu = 2\sqrt{\frac{\nu}{\sigma_0}}. \quad (3.11)$$

We define the absorption coefficient as a_ν , then:

$$a_\nu a_\nu^* = \alpha_\nu. \quad (3.12)$$

As a result, a_ν is given by

$$a_\nu = \sqrt{\alpha_\nu} \exp [i\phi_a], \quad (3.13)$$

where ϕ_a is a phase factor.

Similarly, for the reflection coefficient r_ν :

$$r_\nu r_\nu^* = 1 - \alpha_\nu. \quad (3.14)$$

Then r_ν is given by

$$r_\nu = \sqrt{1 - \alpha_\nu} \exp [i\phi_r], \quad (3.15)$$

where ϕ_r is a phase factor.

These expressions show up in modified Jones operators that describe the non-ideal instrument. We include the subscript ν in the following analyses only when we are working in the frequency domain.

3.3.2 Primary mirrors with non-zero emissivity

Here we investigate degradation due to emission mismatches from the primary mirrors. Geometric mismatches leading to beam errors are explicitly left for an optical treatment. In principle emission can be easily calculated from the conductivity of the material (Equation 3.11), however, it is very sensitive to the details of the surface, cleanliness, surface roughness, temperature, oxidation, *et cetera*, so we leave the actual emissivity as a parameter in the following derivations.

3.3.2.1 Modified operators

When the primary mirrors are modeled to exhibit non-zero emissivity, we define two new reflection operators that correspond to reflections from the left and right primary mirrors, as indicated by the superscripts L and R :

$$\begin{aligned}
\mathbf{J}_r^L &= \begin{bmatrix} -|r_x^L| \exp i\phi_{rx}^L & 0 \\ 0 & -|r_y^L| \exp i\phi_{ry}^L \end{bmatrix}, \\
\mathbf{J}_r^R &= \begin{bmatrix} -|r_x^R| \exp i\phi_{rx}^R & 0 \\ 0 & -|r_y^R| \exp i\phi_{ry}^R \end{bmatrix},
\end{aligned} \tag{3.16}$$

where r_x and r_y are the reflection coefficients in the \hat{x} and \hat{y} directions, and ϕ_{rx} and ϕ_{ry} are phases between incident and reflected radiation in the \hat{x} and \hat{y} directions, respectively.

The left and right primary mirrors also emit radiation whose electric fields are described by:

$$\begin{aligned}
E_M^L &= \begin{bmatrix} \frac{1}{\sqrt{2}} |a_x^L| \sqrt{\mathbf{B}_{\nu,T}} \exp i\phi_{ex}^L \\ \frac{1}{\sqrt{2}} |a_y^L| \sqrt{\mathbf{B}_{\nu,T}} \exp i\phi_{ey}^L \end{bmatrix}, \\
E_M^R &= \begin{bmatrix} \frac{1}{\sqrt{2}} |a_x^R| \sqrt{\mathbf{B}_{\nu,T}} \exp i\phi_{ex}^R \\ \frac{1}{\sqrt{2}} |a_y^R| \sqrt{\mathbf{B}_{\nu,T}} \exp i\phi_{ey}^R \end{bmatrix},
\end{aligned} \tag{3.17}$$

where a_x and a_y are the absorption coefficients in the \hat{x} and \hat{y} -directions, ϕ_{ex} and ϕ_{ey} are phase factors between incident and emitted radiation in the \hat{x} and \hat{y} directions, and the factor of $1/\sqrt{2}$ normalizes the power such that $|E_M|^2 = \mathbf{B}_{\nu,T}$. The subscript M indicates the emission is from a mirror. The absorption and reflection coefficients in Equations 3.16 and 3.17 are related by Equation 3.15.

3.3.2.2 Calculated signal

Treating all optical surfaces except the primary mirrors as ideal, we get the following fringe pattern from the left side \hat{x} detector:

$$\tilde{\mathbf{P}}_x^L = \frac{1}{2} \int \left(\mathcal{C}^2 (1 - \alpha_x^R) - \mathcal{B}^2 (1 - \alpha_y^L) + \frac{1}{2} (\alpha_x^R - \alpha_y^L) \mathbf{B}_{\nu,T} \right) \cos \left(\frac{4\nu z}{c} \right) d\nu, \tag{3.18}$$

where α_x and α_y are the absorptances of the primary mirror along the \hat{x} and \hat{y} directions, and the tilde indicates that this is an actual, not ideal, quantity. None of the phase factors present in Equations 3.16 and 3.17 show up in the fringe pattern expression because the phases are uncorrelated quantities; consequently photons emitted by different optical components do not interfere with each other.

$\tilde{\mathbf{P}}_x^L$ is proportional to the Fourier transform of the radiation incident on the detector, so taking the inverse Fourier transform yields the spectrum $\tilde{\mathbf{S}}_x^L(\nu)$. Expressed as the sum of the spectrum measured by the ideal instrument and an error term $\epsilon_x^L(\nu)$, it is given by

$$\tilde{\mathbf{S}}_x^L(\nu) = \mathcal{C}_\nu^2 - \mathcal{B}_\nu^2 + \epsilon_x^L(\nu). \quad (3.19)$$

The error term is given by

$$\epsilon_x^L(\nu) = \Delta\alpha_\nu (-\mathbf{B}_{\nu,T} + \mathcal{B}_\nu^2 + \mathcal{C}_\nu^2), \quad (3.20)$$

where $\Delta\alpha_\nu$ is the difference in absorptance between the left and right primary mirrors.

The error term shows up in second order and is proportional to the *difference* in absorptance between the left and right primary mirrors, multiplied by the *difference* in temperature between the instrument and the sky. The difference in absorptance will be of order 10^{-4} . This assumes that the average absorptance of the mirrors is of order 10^{-2} and they are matched to a part in 10^2 . Both these constraints are easily met. Well-polished aluminum can demonstrate emissivity of order 10^{-3} at *PIXIE* frequencies [95], and both mirrors will be made from the same aluminum stock. The component of the error term given by the difference spectrum between the sky and the instrument (i.e., the quantity $-\mathbf{B}_{\nu,T} + \mathcal{B}_\nu^2 + \mathcal{C}_\nu^2$ in Equation 3.20) will be a few mK. Uncorrected, the error signal from emissive mirrors will be hundreds of nK, larger than the 100 nK *B*-mode polarization signal. The *PIXIE* design enables identification

and correction of these errors down to the sub-nK level.

3.3.2.3 Identifying and correcting error

Here we focus on identifying and correcting the error given by Equation 3.20. We take advantage of several important elements of *PIXIE*, including the ability to keep the instrument isothermal with the CMB to within a few mK, the ability to actively control and modulate the temperature of each optical component, and the ability to observe the same sky pixel multiple times on short timescales. In the following derivations, we mitigate error only by performing linear operations on measurements performed by a single detector, avoiding any assumptions of uniformity between detector pairs. In practice, however, it is also possible to mitigate error by comparing signals measured by detector pairs.

Cold optics *PIXIE*'s optics will be isothermal with the sky to within a few mK. For a given differential absorptance $\Delta\alpha_\nu$, the error will be determined by the temperature difference between the optics and the sky, denoted δT . Explicitly, if the mirrors are at some temperature $T = T_0 + \delta T$, where T_0 is the CMB temperature, then the error given by Equation 3.20 becomes

$$\epsilon_x^L(\nu) = \Delta\alpha_\nu (-\mathbf{B}_{\nu, T_0 + \delta T} + \mathbf{B}_{\nu, T_0}), \quad (3.21)$$

where we used $\mathbf{B}_{\nu, T_0} = \mathcal{B}_\nu^2 + \mathcal{C}_\nu^2$.

Since δT is small relative to T_0 , we express the quantity $\mathbf{B}_{\nu, T_0 + \delta T}$ as a Taylor series:

$$\mathbf{B}_{\nu, T_0 + \delta T} = \mathbf{B}_{\nu, T_0} + \mathbf{B}'_{\nu, T_0} \delta T + \Theta(\delta T^2), \quad (3.22)$$

where

$$\mathbf{B}'_{\nu, T_0} = \left. \frac{\partial \mathbf{B}_{\nu, T}}{\partial T} \right|_{T=T_0}. \quad (3.23)$$

Then the error reduces to

$$\epsilon_x^L(\nu) = -\Delta\alpha_\nu \mathbf{B}'_{\nu, T_0} \delta T. \quad (3.24)$$

Thus error scales linearly with the temperature difference δT between the sky and the mirrors. Over the course of the mission, we will match each warm temperature $T = T_0 + \delta T$ with a cooler temperature $T = T_0 - \delta T$. As a result, the error will reduce to a higher order term proportional to errors in controlling δT , contributing not to mean measurements, but rather to measurement variance.

Mirror temperature modulation The primary mirrors will be kept close to the CMB temperature T_0 , but we actively modulate and control the temperature difference δT between the mirrors and the sky. Keeping terms through second order, the emission spectrum of the mirrors is

$$\Delta\alpha_\nu \mathbf{B}_{\nu, T} = \Delta\alpha_\nu \left(\mathbf{B}_{\nu, T_0} + \mathbf{B}'_{\nu, T_0} (T - T_0) + \frac{1}{2} \mathbf{B}''_{\nu, T_0} (T - T_0)^2 + \Theta (T - T_0)^3 \right). \quad (3.25)$$

If the mirror is at $T = T_0 + \delta T$, the emission spectrum becomes

$$\Delta\alpha_\nu \mathbf{B}_{\nu, T_0 + \delta T} = \Delta\alpha_\nu \left(\mathbf{B}_{\nu, T_0} + \mathbf{B}'_{\nu, T_0} \delta T + \frac{1}{2} \mathbf{B}''_{\nu, T_0} \delta T^2 + \Theta (\delta T)^3 \right). \quad (3.26)$$

Similarly for $T = T_0 - \delta T$, the emission spectrum becomes

$$\Delta\alpha_\nu \mathbf{B}_{\nu, T_0 - \delta T} = \Delta\alpha_\nu \left(\mathbf{B}_{\nu, T_0} - \mathbf{B}'_{\nu, T_0} \delta T + \frac{1}{2} \mathbf{B}''_{\nu, T_0} \delta T^2 - \Theta (\delta T)^3 \right). \quad (3.27)$$

Now imagine that during the observation of one sky pixel, say at time $t = t_1$, the primary mirrors are held at $T = T_0 + \delta T$. During a subsequent observation of the same sky pixel, at time $t = t_2$, the mirrors are kept at $T = T_0 - \delta T$. If we difference the power measured by a single detector at the two observation times, the sky signals vanish, leaving

$$\tilde{\mathbf{S}}_x^L(\nu) \Big|_{t=t_1} - \tilde{\mathbf{S}}_x^L(\nu) \Big|_{t=t_2} = -2\Delta\alpha_\nu \mathbf{B}'_{\nu, T_0} \delta T + \Theta (\delta T^3). \quad (3.28)$$

Since \mathbf{B}'_{ν, T_0} and δT are known, differencing gives a direct measure of $\Delta\alpha_\nu$ to nK-scale precision.

With $\Delta\alpha_\nu$ measured, consider summing the power measured at the two observation times:

$$\tilde{\mathbf{S}}_x^L(\nu) \Big|_{t=t_1} + \tilde{\mathbf{S}}_x^L(\nu) \Big|_{t=t_2} = 2\mathcal{C}_\nu^2 - 2\mathcal{B}_\nu^2 + \Sigma\epsilon_x^L(\nu), \quad (3.29)$$

where

$$\Sigma\epsilon_x^L(\nu) = \Delta\alpha_\nu \mathbf{B}''_{\nu, T_0} \delta T^2. \quad (3.30)$$

If the temperature excursions δT are kept at the few-mK level, then the residual error given by Equation 3.30 will be $\sim 10^{-10}$ K, much smaller than the expected B -mode signal. It is easily confirmed that the operations that mitigate the left side \hat{x} error to the sub-nK level simultaneously apply to the error measured by the other three detectors. If it turns out that the temperatures at times t_1 and t_2 do not match, then the residual error term will be proportional to the temperature difference between

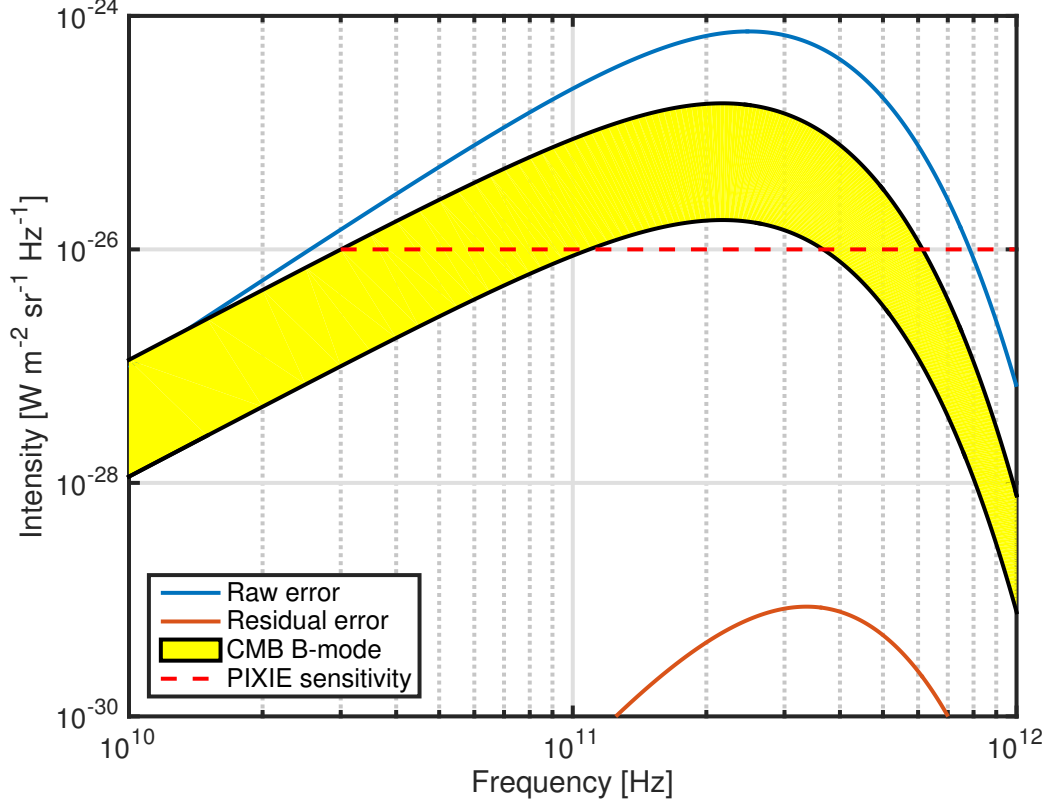


Figure 3.1 Error due to emissive primary mirrors. Both the CMB signal and the raw error are proportional to \mathbf{B}'_{ν, T_0} (Equation 3.23), while the residual error is proportional to \mathbf{B}''_{ν, T_0} . They can therefore be distinguished based on their spectral content. In addition the error terms exhibit the $\nu^{1/2}$ dependence of the absorptance spectrum. We have conservatively assumed that we will know both δT and $\Delta\alpha_\nu$ to within $\sim 1\%$. The B -mode band shows amplitudes for $0.01 < r < 0.1$.

the mirrors at the two times. Differencing the signals gives a measure of this term. Times will be chosen to minimize the difference (error) signal, thereby matching the temperatures. No exact prior knowledge of the mirror temperatures is required.

3.3.2.4 Conclusion

This section shows how emissive primary mirrors affect measured signals. Uncorrected error signals in the raw time stream are hundreds of nK. But *PIXIE*'s design enables significant control over these error signals. By performing simple operations - modulating the temperature of the primary mirrors and taking sums and differences

of power measured by single detectors - the errors can be suppressed to a level that is negligible compared to *PIXIE* noise (see Figure 3.1).

Over the course of the mission, however, the error will become even smaller than is represented by Equation 3.30. We will take linear combinations of signals from not just two measurements of the same pixel of sky, but repeated measurements of all sky pixels. This enables knowledge of δT and $\Delta\alpha_\nu$ with ever increasing precision. As a result, we will subtract away error of the form given by Equation 3.30, leaving some higher order term whose magnitude is $< 1\%$ of the error given by Equation 3.30.

3.3.3 Polarizer grid A with non-zero emissivity

The *PIXIE* polarizing grids will be grids of fine wire stretched over a stiff frame. We have constructed grids of 12 μm diameter tungsten wire with 30 μm spacing with ≤ 5 μm rms error in spacing and flatness over ~ 100 mm diameters. For frequencies less than 500 GHz (i.e., most of the CMB spectrum) these are essentially perfect [96]. By employing free-standing wire grid polarizers and keeping the FTS isothermal with the sky, we avoid some of the beam splitter systematics others have observed [e.g. 97, and references therein]. Thus our treatment of systematics stemming from the polarizing grids is limited to emission and absorption (this section) and misalignments (Section 3.4.1).

When a polarizing grid is modeled to exhibit non-zero emissivity, its reflection and transmission operators change, and it also emits thermal radiation. We treat polarizer A as emissive, demonstrating how errors appear in the measured fringe pattern. Later we consider the case of an emissive polarizer B, which only attenuates the sky signal.

3.3.3.1 Modified operators

There are four relevant operators which act on transmitted or reflected light incident from the left or right side of an emissive polarizer A. The transmission and reflection

operators that act on radiation incident from the left are given by

$$\begin{aligned}\mathbf{J}_t^L &= \begin{bmatrix} 1 & 0 \\ 0 & 0 \end{bmatrix}, \\ \mathbf{J}_r^L &= \begin{bmatrix} 0 & 0 \\ 0 & -|r| \exp i\phi_r^L \end{bmatrix},\end{aligned}\tag{3.31}$$

where $|r|$ is the reflection coefficient of the grid and ϕ_r^L is the phase between incident and reflected light off the grid. The transmission operator does not change since light whose electric field is orthogonal to the wire grids is not sensitive to emissive wires.

The equivalent operators that act on radiation incident from the right are given by

$$\begin{aligned}\mathbf{J}_t^R &= \begin{bmatrix} 1 & 0 \\ 0 & 0 \end{bmatrix}, \\ \mathbf{J}_r^R &= \begin{bmatrix} 0 & 0 \\ 0 & -|r| \exp i\phi_r^R \end{bmatrix},\end{aligned}\tag{3.32}$$

where $|r|$ is the reflection coefficient and ϕ_r^R is the associated phase factor. We assume here that both sides of the grid have the same reflection coefficient. This is not strictly the case, but any differences between the two will be small. For details see [96].

The grids also emit thermal radiation along the same direction as reflections. The electric fields from this radiation are represented by

$$\begin{aligned}E_P^L &= \begin{bmatrix} 0 \\ \frac{1}{2} |a| \sqrt{\mathbf{B}_{\nu,T}} \exp i\phi_e^L \end{bmatrix}, \\ E_P^R &= \begin{bmatrix} 0 \\ \frac{1}{2} |a| \sqrt{\mathbf{B}_{\nu,T}} \exp i\phi_e^R \end{bmatrix},\end{aligned}\tag{3.33}$$

where $|a|$ is the absorption coefficient of the grid, ϕ_e is the phase between incident and emitted radiation, and the factor of $1/2$ normalizes the power such that $|E_P^L|^2 + |E_P^R|^2 = \mathbf{B}_{\nu,T}/2$. The subscript P indicates that this is emission from a polarizer.

3.3.3.2 Calculated signal

Treating all optical surfaces except polarizer A as ideal, we get the following fringe pattern:

$$\tilde{\mathbf{P}}_x^L = \frac{1}{2} \int \left(\mathcal{C}^2 - \mathcal{B}^2 (1 - \alpha) - \frac{1}{2} \alpha \mathbf{B}_{\nu,T} \right) \cos \left(\frac{4\nu z}{c} \right) d\nu, \quad (3.34)$$

where α is the absorptance of the grids. We take the inverse Fourier transform and express the resulting spectrum as the sum of the ideal instrument's measurement and an error term $\epsilon_x^L(\nu)$. Up to some constant, the spectrum is

$$\tilde{\mathbf{S}}_x^L(\nu) = \mathcal{C}_\nu^2 - \mathcal{B}_\nu^2 + \epsilon_x^L(\nu), \quad (3.35)$$

and error term is given by

$$\epsilon_x^L(\nu) = \alpha_\nu \left(\mathcal{B}_\nu^2 - \frac{1}{2} \mathbf{B}_{\nu,T} \right). \quad (3.36)$$

The error from an emissive polarizer A is similar to that from emissive mirrors (Equation 3.20), except it is sensitive to absolute absorptance instead of differential absorptance. This is the only emissive systematic error that is sensitive to absolute absorptance. This is because only one polarization is reflected by the grid and therefore subject to attenuation. The other polarization passes through unaware that the grid is emissive. Similarly, emission from the grid is only in one polarization.

Before performing any corrective actions, we estimate the raw magnitude of the error. The quantity in parenthesis will be proportional to the temperature difference between the sky and the grid (a few mK). The absorptance of the grids α_ν will be

$\sim 10^{-2}$. Therefore the error will be of order $10 \mu\text{K}$.

3.3.3.3 Identifying and correcting error

To identify and correct the error given by Equation 3.36, we modulate the temperature of the wire grids by some δT about the CMB temperature and observe the same sky pixel multiple times. Again the details will be presented for measurements by the left side \hat{x} detector, but the techniques employed simultaneously apply to measurements made by the other three detectors.

Cold optics The wire grids will be kept isothermal with the sky to within a few mK. The quantity \mathcal{B}_ν^2 will be a Planck spectrum at CMB temperature T_0 , but at half the overall intensity since it represents only one polarization state. Then the error given by Equation 3.36 reduces to

$$\epsilon_x^L(\nu) = \alpha_\nu \left(\frac{1}{2} \mathbf{B}_{\nu, T_0} - \frac{1}{2} \mathbf{B}_{\nu, T} \right). \quad (3.37)$$

Since the temperature of the wire grids will be close to that of the sky, we represent the emission spectrum of the grids as a Taylor series. Then the error becomes

$$\epsilon_x^L(\nu) = \frac{1}{2} \alpha_\nu \mathbf{B}'_{\nu, T_0} \delta T. \quad (3.38)$$

The error due to an emissive grid will scale linearly with the temperature difference between the grids and the sky. As with the primary mirrors, each warm temperature $T = T_0 + \delta T$ will be matched with a cooler temperature $T = T_0 - \delta T$. Then the error given by Equation 3.38 will ultimately reduce to a higher order term that depends on the uncertainty of δT .

Grid temperature modulation We mitigate the error due to an emissive grid by modulating the grid's temperature and taking linear combinations of measured

signals. Assume that during the observation of a pixel of sky at time $t = t_1$, the emissive wire grid polarizer is at temperature $T = T_0 + \delta T$, and that during a subsequent observation of the same sky pixel at time $t = t_2$, the polarizer is at temperature $T = T_0 - \delta T$. Differencing the power measured at times t_1 and t_2 gives

$$\tilde{\mathbf{S}}_x^L(\nu) \Big|_{t=t_1} - \tilde{\mathbf{S}}_x^L(\nu) \Big|_{t=t_2} = -\alpha_\nu \mathbf{B}'_{\nu, T_0} + \Theta(\delta T^3). \quad (3.39)$$

\mathbf{B}'_{ν, T_0} is known, so differencing gives a measure of the average absorptance α_ν of the wire grids. This operation also gives us the ability to measure the differential absorptance between two sides of the same grid. Examining $\epsilon_x^L(\nu)$ and $\epsilon_y^R(\nu)$ gives the absorptance of the left side of the grid, and examining $\epsilon_y^L(\nu)$ and $\epsilon_x^R(\nu)$ gives the absorptance of the right side.

Summing the power measured at times t_1 and t_2 gives

$$\tilde{\mathbf{S}}_x^L(\nu) \Big|_{t=t_1} + \tilde{\mathbf{S}}_x^L(\nu) \Big|_{t=t_2} = 2\mathcal{C}_\nu^2 - 2\mathcal{B}_\nu^2 + \Sigma\epsilon_{lx}(\nu), \quad (3.40)$$

where the error term is given by

$$\Sigma\epsilon_x^L(\nu) = -\alpha_\nu \mathbf{B}''_{\nu, T_0} \delta T^2. \quad (3.41)$$

The residual error given by Equation 3.41 is at the nK level, and as a twice-differential Planck spectrum, its spectral content will differ from that of the sky.

3.3.3.4 Conclusion

This section shows how error from an emissive polarizer A will affect the measured signals. Uncorrected, errors are of order 10 μK . By modulating the temperature of the emissive grid and taking linear combinations of power measured at different times, these errors can be reduced to below 1 nK (see Figure 3.2). If we instead take sums and differences of signals measured by detector pairs, then both the raw and residual

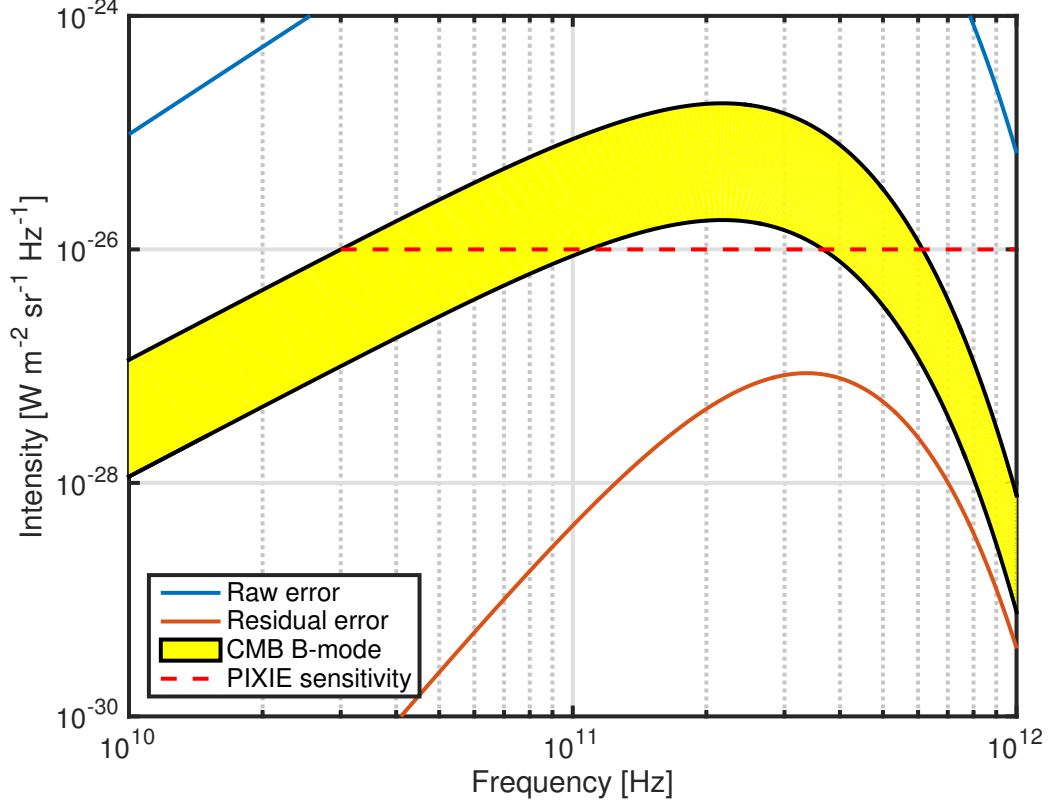


Figure 3.2 Error due to an emissive polarizer A. Both the CMB signal and the raw error are proportional to \mathbf{B}'_{ν, T_0} , while the residual error is proportional to \mathbf{B}''_{ν, T_0} . We have conservatively assumed that we will know both δT and α_ν to within $\sim 1\%$, so the residual error is a factor of 100 smaller than expressed in Equation 3.41. If we instead take sums and differences of signals measured by different detectors, both the raw and residual error will be at least two orders of magnitude smaller, **and only** sensitive to differential, rather than absolute, absorptance. The B -mode band shows amplitudes for $0.01 < r < 0.1$.

errors will be proportional to the differential absorptance between the two sides of the grid, taking the same form as error from emissive primary mirrors (Equations 3.20 and 3.30, respectively). Their magnitudes will be at least two orders of magnitude smaller than in Figure 3.2.

3.3.4 Polarizer B with non-zero emissivity

In this section, we model polarizer B as exhibiting non-zero emissivity, demonstrating how non-ideal optical components downstream of the second transfer mirrors affect

our measurements. Their effect is different from the previous two examples because thermal photons emitted by such surfaces are not split, mixed, and interfered, thus they contribute no modulated error signals. Instead, non-unity reflectivity only attenuates our sky signals, an effect that is measured with the calibrator.

3.3.4.1 Modified operators

Polarizer B is oriented at 45° relative to polarizer A, so its non-ideal operators are derived by applying the rotation operator to polarizer A's modified operators. Then the transmission and reflection operators that act on radiation incident from the left are given by

$$\begin{aligned} \mathbf{J}_t^L &= \mathbf{R}_Z(45^\circ) \times \begin{bmatrix} 1 & 0 \\ 0 & 0 \end{bmatrix} \times \mathbf{R}_Z^\dagger(45^\circ), \\ \mathbf{J}_r^L &= \mathbf{R}_Z(45^\circ) \times \begin{bmatrix} 0 & 0 \\ 0 & -|r| \exp i\phi_r^L \end{bmatrix} \times \mathbf{R}_Z^\dagger(45^\circ). \end{aligned} \quad (3.42)$$

The equivalent operators that act on radiation incident from the right are given by

$$\begin{aligned} \mathbf{J}_t^R &= \mathbf{R}_Z(45^\circ) \times \begin{bmatrix} 1 & 0 \\ 0 & 0 \end{bmatrix} \times \mathbf{R}_Z^\dagger(45^\circ), \\ \mathbf{J}_r^R &= \mathbf{R}_Z(45^\circ) \times \begin{bmatrix} 0 & 0 \\ 0 & -|r| \exp i\phi_r^R \end{bmatrix} \times \mathbf{R}_Z^\dagger(45^\circ). \end{aligned} \quad (3.43)$$

The grids emit thermal radiation along the same direction as reflections. The electric fields from this radiation are given by

$$\begin{aligned}
E_P^L &= \mathbf{R}_Z(45^\circ) \times \begin{bmatrix} 0 \\ \frac{1}{2} |a| \sqrt{\mathbf{B}_{\nu,T}} \exp i\phi_e^L \end{bmatrix}, \\
E_P^R &= \mathbf{R}_Z(45^\circ) \times \begin{bmatrix} 0 \\ \frac{1}{2} |a| \sqrt{\mathbf{B}_{\nu,T}} \exp i\phi_e^R \end{bmatrix}.
\end{aligned} \tag{3.44}$$

Again we set the absorption coefficient $|a|$ of the two sides of the grid to be equal.

3.3.4.2 Calculated signal

Treating all optical surfaces but polarizer B as ideal, we get the following fringe pattern:

$$\tilde{\mathbf{P}}_x^L = \frac{1}{2} \int |r| (\mathcal{C}^2 - \mathcal{B}^2) \cos\left(\frac{4\nu z}{c}\right) d\nu, \tag{3.45}$$

where $|r|$ is the reflection coefficient of the grid. We take the inverse Fourier transform to get the spectrum:

$$\tilde{\mathbf{S}}_x^L(\nu) = |r| (\mathcal{C}_\nu^2 - \mathcal{B}_\nu^2). \tag{3.46}$$

No further steps need to be taken. The attenuation term $|r|$ is part of the instrument's optical efficiency and is measured by the calibrator throughout the flight.

3.3.4.3 Conclusion

In this section we use the example of polarizer B to show how non-ideal optical components positioned downstream of the second transfer mirrors affect our measured signal. Unlike the examples of the primary mirrors and polarizer A, they contribute no systematic error, but instead only attenuate the sky signal.

3.3.5 Emission from non-optical components

According to ray trace calculations, up to $\sim 3\%$ of radiation incident on the detectors will not be from the sky or emitted by any optical components (such as mirrors or grids), but rather will be from emissive non-optical components, such as the transfer mirror frames. Equivalently, $\sim 3\%$ of light incident on the instrument will be absorbed by non-optical components. These frames and other components will be black, having emissivity approaching 1. In this section we show that emission from surfaces upstream of polarizer B will result in residual error identical in form to that sourced by emissive primary mirrors.

3.3.5.1 Emission from transfer mirror frames

Radiation emitted by the transfer mirror frames is described by the following electric fields:

$$\begin{aligned}
 E_F^L &= \begin{bmatrix} \frac{1}{\sqrt{2}}\sqrt{\kappa} |a_x^L| \sqrt{\mathbf{B}_{\nu,T}} \exp i\phi_{ex}^L \\ \frac{1}{\sqrt{2}}\sqrt{\kappa} |a_y^L| \sqrt{\mathbf{B}_{\nu,T}} \exp i\phi_{ey}^L \end{bmatrix}, \\
 E_F^R &= \begin{bmatrix} \frac{1}{\sqrt{2}}\sqrt{\kappa} |a_x^R| \sqrt{\mathbf{B}_{\nu,T}} \exp i\phi_{ex}^R \\ \frac{1}{\sqrt{2}}\sqrt{\kappa} |a_y^R| \sqrt{\mathbf{B}_{\nu,T}} \exp i\phi_{ey}^R \end{bmatrix},
 \end{aligned} \tag{3.47}$$

where κ is the fraction of power incident on the instrument that is absorbed by the frames and the subscript F indicates that the radiation is coming from a transfer mirror frame.

The absorption coefficients present in Equation 3.47 also act on incident radiation, such that a fraction $\kappa\alpha \sim 0.03$ of power incident on the instrument is absorbed by the non-optical components.

3.3.5.2 Calculated signal

Treating all optical surfaces as ideal, and accounting for emission from the transfer mirror frames, we get the following fringe pattern:

$$\tilde{\mathbf{P}}_x^L = \frac{1}{2} \int \left(\mathcal{C}^2 (1 - \kappa \alpha_x^L) - \mathcal{B}^2 (1 - \kappa \alpha_y^R) + \kappa (\alpha_x^R - \alpha_y^L) \mathbf{B}_{\nu,T} \right) \cos \left(\frac{4\nu z}{c} \right) d\nu. \quad (3.48)$$

Taking the inverse Fourier transform gives the spectrum:

$$\tilde{\mathbf{S}}_x^L(\nu) = \mathcal{C}_\nu^2 - \mathcal{B}_\nu^2 + \epsilon_x^L(\nu). \quad (3.49)$$

The associated error term is given by

$$\epsilon_x^L(\nu) = \kappa_\nu \Delta\alpha_\nu (\mathbf{B}_{\nu,T} - \mathbf{B}_{\nu,T_0}), \quad (3.50)$$

where $\Delta\alpha_\nu$ is the differential absorptance between the left and right frames.

Before taking any corrective actions, we estimate the magnitude of the error given by Equation 3.50. If $\sim 3\%$ of all radiation incident on the detectors is emitted by non-optical components, then $\kappa_\nu \sim 0.03$. The quantity $\Delta\alpha_\nu$ will be of order 10^{-2} . The difference spectrum between the sky and the frames will be proportional to their temperature difference (a few mK). Therefore the error from emissive non-optical components will be hundreds of nK.

3.3.5.3 Identifying and correcting error

To identify and correct emissive frame errors, we actively control temperature of the frames and observe the same sky pixel multiple times. The operations shown apply to the signals measured by all detectors.

Cold optics For a given differential absorptance $\Delta\alpha_\nu$, the magnitude of the error is determined by the temperature difference between the frames and the sky. If the frames are at some temperature $T = T_0 + \delta T$, then the error is

$$\epsilon_x^L(\nu) = \kappa_\nu \Delta\alpha_\nu \mathbf{B}'_{\nu, T_0} \delta T. \quad (3.51)$$

The error scales linearly with the temperature difference δT between the sky and the frames. Its spectrum will differ from polarized CMB signals since it is multiplied by κ_ν , which exhibits the ν^{-1} dependence of diffraction off hard edges in the FTS. Since the average temperature of the frames over the whole mission will be very near T_0 , the error will ultimately reduce to a higher order term proportional to uncertainty in δT .

Frame temperature modulation During the observation of one sky pixel, the transfer mirror frames are held at $T = T_0 + \delta T$, and during a subsequent observation of the same sky pixel, the frames are kept at $T = T_0 - \delta T$. Differencing the power measured at the two times gives:

$$\tilde{\mathbf{S}}_x^L(\nu) \Big|_{t=t_1} - \tilde{\mathbf{S}}_x^L(\nu) \Big|_{t=t_2} = 2\kappa_\nu \Delta\alpha_\nu \left(\mathbf{B}'_{\nu, T_0} \delta T + \Theta(\delta T^3) \right). \quad (3.52)$$

Both \mathbf{B}'_{ν, T_0} and δT are well known, so differencing gives a measure of $\kappa_\nu \Delta\alpha_\nu$ to nK-scale precision.

With $\kappa_\nu \Delta\alpha_\nu$ measured, consider summing the measured powers:

$$\tilde{\mathbf{S}}_x^L(\nu) \Big|_{t=t_1} + \tilde{\mathbf{S}}_x^L(\nu) \Big|_{t=t_2} = 2\mathcal{C}_\nu^2 - 2\mathcal{B}_\nu^2 + \Sigma\epsilon_x^L(\nu), \quad (3.53)$$

where

$$\Sigma\epsilon_x^L(\nu) = \kappa_\nu \Delta\alpha_\nu \mathbf{B}''_{\nu, T_0} \delta T^2. \quad (3.54)$$

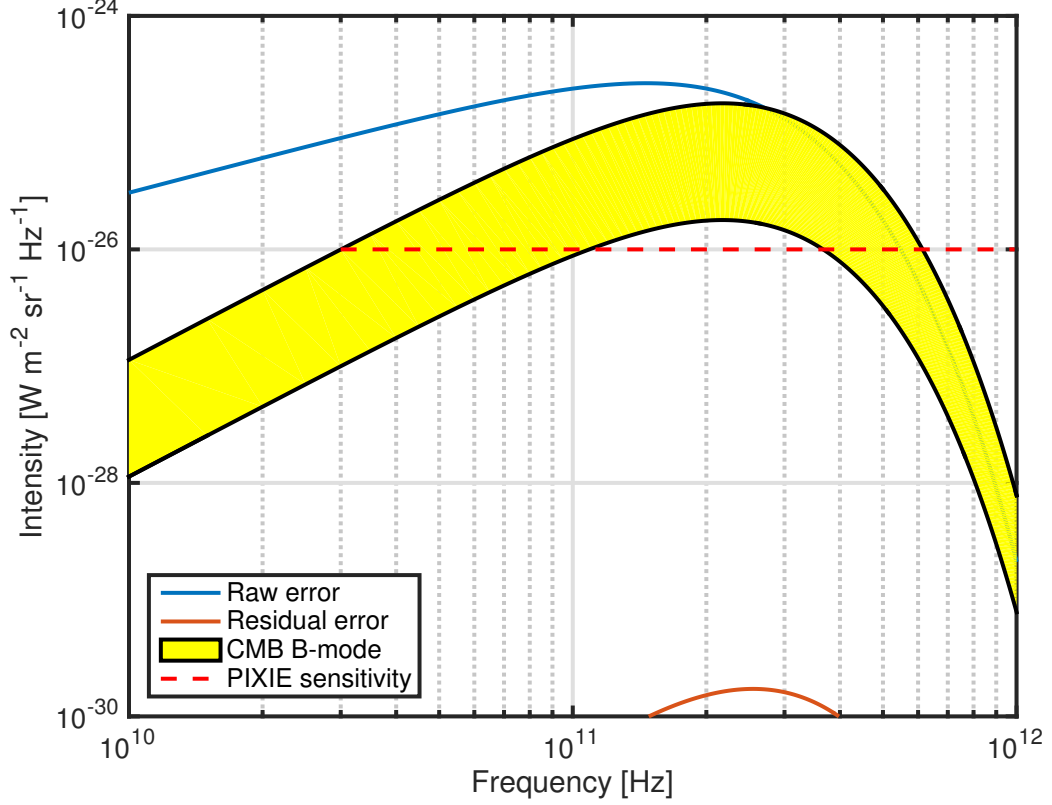


Figure 3.3 Error due to emissive non-optical components. Both the CMB signal and the raw error are proportional to \mathbf{B}'_{ν, T_0} , while the residual error is proportional to \mathbf{B}''_{ν, T_0} . Both the raw and residual error exhibit the ν^{-1} dependence of the diffraction coefficient κ_ν . We have conservatively assumed that we will know both δT and $\Delta\alpha_\nu$ to within $\sim 1\%$, so the plotted corrected error is a factor of 100 smaller than expressed in Equation 3.54. The B -mode band shows amplitudes for $0.01 < r < 0.1$.

The residual error given by Equation 3.54 will be of order 10^{-10} K.

3.3.5.4 Conclusion

In this section we show how systematic error terms from emissive non-optical components are identified and corrected. For reasons discussed in Section 3.3.4, we are only concerned with thermal emission from components upstream of polarizer B. Uncorrected, such error is hundreds of nK. After performing corrective actions the residual error is well below 1 nK (see Figure 3.3).

3.4 Geometric errors

In this section we treat geometric errors. Of particular concern are geometric errors that lead to polarization leaks, which reduce the polarization sensitivity of the instrument. For example, a polarizing grid whose wires are not parallel allows transmission of light that should be reflected and reflection of light that should be transmitted. A polarizing grid that is misaligned by some angle about the direction of propagation of radiation has a similar effect. Broken grid wires also reduce the polarization sensitivity of the instrument. In the following we look specifically at misalignments of polarizers A and D, which are representative of any grid non-ideality that yields polarization leaks.

We also consider transfer mirrors that are misaligned by some angle, but this case is best understood as a phase error in the Fourier transform. As such, it is treated in Section 3.5. Misalignments of the primary mirrors, folding flats, and secondary mirrors lead to beam mismatches on the sky and are left to a separate work.

3.4.1 Misalignment of polarizers A and D

Here we model polarizers A and D to be misaligned by some small angle $\Delta\theta$ about the \hat{z} -axis. Since polarizers A and D define the polarization sensitivity, a common error only rotates the polarization axis. This can lead to power leakage from E -modes to B -modes, an error that is well treated in the literature [e.g., 98], but it will not generate a polarized signal when the sky is unpolarized. Thus the concern is with differential errors. As such, polarizer A will be misaligned by $+\Delta\theta$, and polarizer D will be misaligned by $-\Delta\theta$. We will let all other optical surfaces, and their alignments, be ideal.

3.4.1.1 Modified operators

To account for small misalignments, we modify each polarizer's ideal reflection and transmission operators by applying the rotation operator $\mathbf{R}_Z(\pm\Delta\theta)$. Because the rotation angle $\Delta\theta$ will be small, the rotation operator for a misalignment of $\pm\Delta\theta$ is

$$\mathbf{R}_Z(\Delta\theta) = \begin{bmatrix} 1 & \mp\Delta\theta \\ \pm\Delta\theta & 1 \end{bmatrix}. \quad (3.55)$$

Then polarizer A's transmission and reflection operators are:

$$\begin{aligned} \mathbf{J}_t^L &= \mathbf{J}_t^R \\ &= \mathbf{R}_Z(\Delta\theta) \times \begin{bmatrix} 1 & 0 \\ 0 & 0 \end{bmatrix} \times \mathbf{R}_Z^\dagger(\Delta\theta); \end{aligned} \quad (3.56)$$

$$\begin{aligned} \mathbf{J}_r^L &= \mathbf{J}_r^R \\ &= \mathbf{R}_Z(\Delta\theta) \times \begin{bmatrix} 0 & 0 \\ 0 & -1 \end{bmatrix} \times \mathbf{R}_Z^\dagger(\Delta\theta), \end{aligned} \quad (3.57)$$

and the equivalent transmission and reflection operators for polarizer D are:

$$\begin{aligned} \mathbf{J}_t^L &= \mathbf{J}_t^R \\ &= \mathbf{R}_Z(-\Delta\theta) \times \begin{bmatrix} 1 & 0 \\ 0 & 0 \end{bmatrix} \times \mathbf{R}_Z^\dagger(-\Delta\theta); \end{aligned} \quad (3.58)$$

$$\begin{aligned} \mathbf{J}_r^L &= \mathbf{J}_r^R \\ &= \mathbf{R}_Z(-\Delta\theta) \times \begin{bmatrix} 0 & 0 \\ 0 & -1 \end{bmatrix} \times \mathbf{R}_Z^\dagger(-\Delta\theta). \end{aligned} \quad (3.59)$$

3.4.1.2 Calculated signal

Treating all optical surfaces as having zero emissivity, and assuming all components are perfectly aligned except polarizers A and D, we get the following fringe pattern:

$$\tilde{\mathbf{P}}_x^L = \frac{1}{2} \int (\mathcal{C}^2 - \mathcal{B}^2 + 4\Delta\theta\mathcal{B}\mathcal{C}) \cos\left(\frac{4\nu z}{c}\right) d\nu. \quad (3.60)$$

We take the inverse Fourier transform and express the spectrum as the sum of the ideal instrument's measurement and an error term:

$$\tilde{\mathbf{S}}_x^L(\nu) = \mathcal{C}_\nu^2 - \mathcal{B}_\nu^2 + \epsilon_x^L(\nu), \quad (3.61)$$

where the error term is given by

$$\epsilon_x^L(\nu) = 4\Delta\theta\mathcal{B}_\nu\mathcal{C}_\nu. \quad (3.62)$$

This error is proportional to the \hat{y} -polarized signal incident on the left side of the instrument multiplied by the \hat{x} -polarized signal incident on the right side. It will vanish when the calibrator is deployed since there can be no cross-polar response between mutually incoherent sources. Therefore the error is easily measured by differencing the signal measured with and without the calibrator. In addition this error vanishes in the absence of a polarized sky. To see this, it is useful to transform the error from instrument-fixed to sky-fixed coordinates (see Section 2.2.3).

With both sides of the instrument open to the sky, the error due to misalignments in sky-fixed coordinates is

$$\epsilon_x^L(\nu) = 2\Delta\theta (U^{sky} \cos 2\gamma + Q^{sky} \sin 2\gamma), \quad (3.63)$$

where Q^{sky} and U^{sky} are the Stokes parameters in sky-fixed coordinates and γ is the spacecraft rotation angle.

As is clear from Equation 3.63, the error signal will vanish if the sky is unpolarized. Furthermore, it is a calibration term; it has the same form as the signal measured by the ideal instrument, except it is multiplied by the misalignment angle $\Delta\theta$. Misalignments of $\sim 1/2^\circ$ will keep this term at the 1% level. No further steps need to be taken to correct this error.

3.4.2 Conclusion

We show in this section how systematic error signals due to misaligned optical components originate, are identified, and are corrected. While we looked specifically at the case of rotated polarizers, the results and corrective actions applied are similar for any optical defect that causes a cross-polar response. Uncorrected, we get an error signal proportional to the misalignment angle, but it is easily measured and corrected by deploying the calibrator. By transforming the error from instrument-fixed to sky-fixed coordinates, we recognize that the error term is in fact a calibration term, so its presence reduces the signal-to-noise ratio by lowering our sensitivity to polarized signals, but it will not create a polarized signal from an unpolarized source.

If we model polarizer A to be both misaligned and emissive, we get an additional systematic error term similar in form to that given by Equation 3.36, except it will be multiplied by the misalignment angle $\Delta\theta$. As a result, it will be a factor of $\sim 10^3$ smaller than the dominant emissive grid systematic, showing up at the sub-nK level without any corrections. The same operations that mitigate the dominant error given by Equation 3.36 apply to this term.

3.5 Mirror transport mechanism (MTM) errors

In this section we treat non-idealities in the mirror transport mechanism, which can lead to systematic error terms or contribute to the noise. If the zeroth sample of the

interferogram is not at the null or zero phase position, where the path length of light traveling in either FTS beam is the same, there will be a corresponding phase error that asymmetrizes the interferogram. If the mirror stroke is not symmetric about the null position, the interferogram will also be asymmetric. Geometric misalignments of transfer mirrors lead to phase errors in the Fourier transform (this is not strictly a MTM error, but is best understood in this context). Uncertainties in the mirror position, which can relate to both timing and position errors, can lead to the presence of additional sidebands in the measured spectrum. We look at each of these errors in the general case, including a discussion of the steps that can be taken to mitigate them. Then we see how they affect the measurements.

3.5.1 Phase errors

3.5.1.1 The ideal interferogram

The theoretical treatment in the following closely follows the derivations presented by [99], [100], [101] and [102]. An alternative approach is presented by [103].

Consider the ideal case where both the interferogram and mirror stroke are symmetric about the null. In this case, the signal measured by a detector, say the left side \hat{x} detector, will be given by

$$\mathbf{P}_x^L(\ell) = \int_{-\infty}^{\infty} \mathbf{S}_x^L(\nu) \cos(2\pi\nu\ell) d\nu, \quad (3.64)$$

up to some constant factor. Here ℓ is the optical path difference between the two FTS beams, and ν is frequency expressed in wavenumber. The interferogram $\mathbf{P}_x^L(\ell)$ is a function of the MTM position $z \simeq \ell/4$, and the corresponding spectrum $\mathbf{S}_x^L(\nu)$ is a function of frequency ν . The peak of the interferogram occurs at the null position $\ell = 0$, and the interferogram is symmetric about this peak position (see Figure 3.4). To recover the spectrum $\mathbf{S}_x^L(\nu)$ for the symmetric case, the full complex Fourier

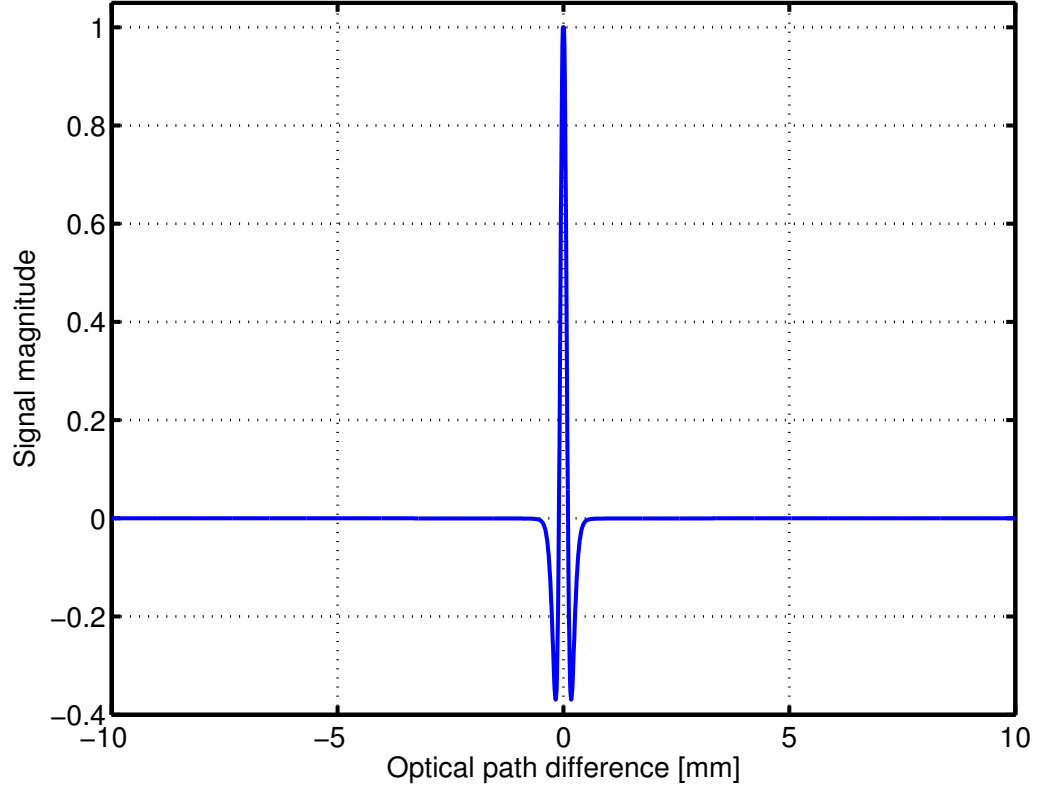


Figure 3.4 The ideal two-sided interferogram showing the Fourier transform of the polarized CMB. Because the interferogram is symmetric about the null position, the spectrum can be recovered by performing the Fourier cosine transform on either half of the interferogram.

transform need not be applied. Rather we can apply just the even part (the Fourier cosine transform) to $\mathbf{P}_x^L(\ell)$. This operation gives, up to a constant factor,

$$\mathbf{S}_x^L(\nu) = \int_{-\infty}^{\infty} \mathbf{P}_x^L(\ell) \cos(2\pi\nu\ell) d\ell. \quad (3.65)$$

By symmetry, Equation 3.65 can also be written as

$$\mathbf{S}_x^L(\nu) = 2 \int_0^{\infty} \mathbf{P}_x^L(\ell) \cos(2\pi\nu\ell) d\ell. \quad (3.66)$$

The incident spectrum $\mathbf{S}_x^L(\nu)$ can be recovered independently by taking the Fourier cosine transform of either half of the full two-sided interferogram.

Equation 3.65 assumes that the mirror throw is infinite. This will not be the

case, so we need to include an apodization function $A(\ell)$ that takes into account the finite throw of the mirror. For *PIXIE*, the maximum mirror throw will be ± 2.7 mm, corresponding to a total optical path difference $L = \pm 10$ mm. We will sample the interferogram at 256 Hz, and a complete mirror stroke from one extreme to the other takes 3 seconds. Assuming that the MTM moves at a constant speed, this means individual samples will be spaced $26 \mu\text{m}$ apart from one another in path difference or $5.3 \mu\text{m}$ in physical difference. In the ideal case, $A(\ell)$ is even symmetric about the null position, so its spectrum is given by its Fourier cosine transform:

$$A(\nu) = \int_{-\infty}^{\infty} A(\ell) \cos(2\pi\nu\ell) d\ell. \quad (3.67)$$

Then the actual spectrum $\tilde{\mathbf{S}}_x^L(\nu)$ measured by the detector is given by the convolution of $\mathbf{S}_x^L(\nu)$ and $A(\nu)$:

$$\tilde{\mathbf{S}}_x^L(\nu) = \mathbf{S}_x^L(\nu) \star A(\nu), \quad (3.68)$$

where the \star operator is the convolution.

The *PIXIE* mirror scan strategy yields an apodization function given by

$$A(\ell) = \left(1 - \left(\frac{\ell}{L}\right)^4\right)^2, \quad (3.69)$$

where L is the optical path difference between the two beams at the mirror's maximum displacement from the null. For further details about *PIXIE*'s mirror scanning strategy and the resultant apodization, see [52].

3.5.1.2 Asymmetric apodization

The first class of MTM errors we treat comes about if the apodization function $A(\ell)$ is not symmetric about the null position. In this case, the apodization function becomes

$$\tilde{A}(\ell) = \left(1 - \left(\frac{\ell - \Delta\ell}{L}\right)^4\right)^2, \quad (3.70)$$

where $\Delta\ell$ is the displacement from the null about which $\tilde{A}(\ell)$ is symmetric. By the Fourier shift theorem, this gives a corresponding phase shift $\beta(\nu)$ in the frequency domain, where

$$\beta(\nu) = -2\pi\nu\Delta\ell. \quad (3.71)$$

Then the spectrum of the apodization function is

$$\tilde{A}(\nu) = A(\nu) \exp(i\beta(\nu)). \quad (3.72)$$

The offset $\Delta\ell$ is small relative to the sample spacing, so we express $\tilde{A}(\ell)$ as a Taylor series. Keeping terms through second order in $\Delta\ell$, it is

$$\tilde{A}(\ell) = A(\ell) + \Delta\ell \left(\frac{8\ell^3}{L^4} - \frac{8\ell^7}{L^8}\right) - \Delta\ell^2 \left(\frac{12\ell^2}{L^4} - \frac{28\ell^6}{L^8}\right), \quad (3.73)$$

where $A(\ell)$ is given by Equation 3.69. This is plotted in Figure 3.5.

The measured spectrum can therefore be expressed as the sum of the ideal apodized spectrum and an error term:

$$\tilde{\mathbf{S}}_x^L(\nu) = \mathbf{S}_x^L(\nu) \star A(\nu) + \epsilon_x^L(\nu), \quad (3.74)$$

where the error is given by

$$\epsilon_x^L(\nu) = \mathbf{S}_x^L(\nu) \star \mathcal{F} \left[\Delta\ell \left(\frac{8\ell^3}{L^4} - \frac{8\ell^7}{L^8}\right) - \Delta\ell^2 \left(\frac{12\ell^2}{L^4} - \frac{28\ell^6}{L^8}\right) \right]. \quad (3.75)$$

The operator \mathcal{F} is the Fourier transform.

The effect of the apodization error will be to distort the ideal spectrum. This error

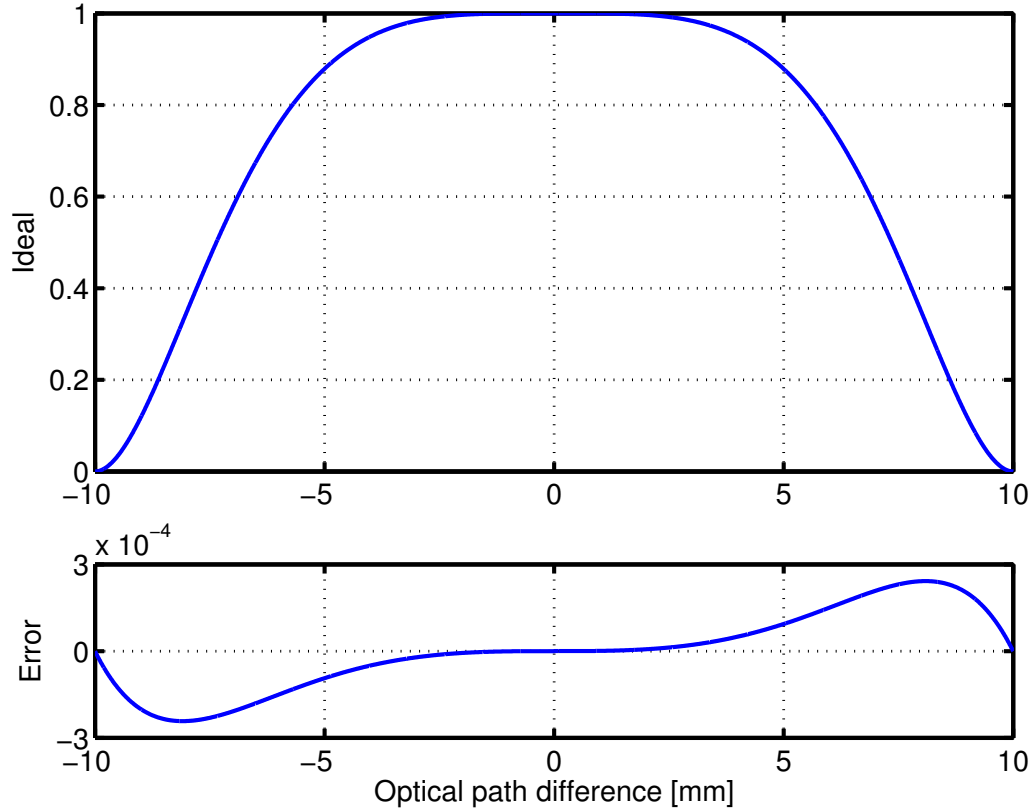


Figure 3.5 Ideal apodization function (top) and its non-ideal counterpart (bottom). Their relative magnitudes are calculated for $\Delta\ell = 1 \mu\text{m}$.

can be corrected by averaging the two sides of a full interferogram before taking the Fourier cosine transform of the resultant one sided interferogram. This is equivalent to taking a complex Fourier transform of the full stroke and keeping the real part, which we will do in practice. This works because the error in $\tilde{A}(\ell)$ is approximately anti-symmetric about the mirror's null position. After performing this operation, the apodization error falls to many orders of magnitude below expected *B*-mode signals (see Figure 3.6).

3.5.1.3 Asymmetric interferogram

If the zeroth sample is not at the null position, then the interferogram will no longer be symmetric about $\ell = 0$. In the following, we derive the analytic form for the asymmetric interferogram that results when the zeroth sample is not located at the

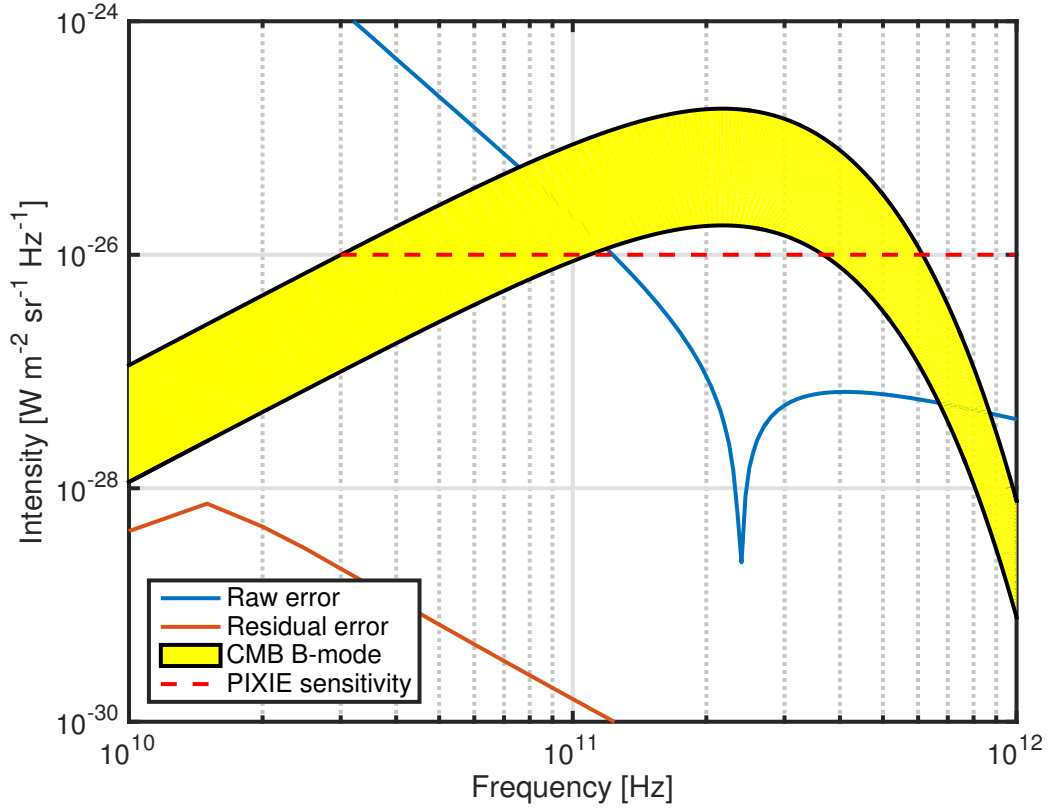


Figure 3.6 Error in foreground measurements due to asymmetries in the apodization function. We assume that the mirror stroke is symmetric about a position $\Delta\ell = 1 \mu\text{m}$. Because the error term in the apodization function is nearly odd-symmetric about the mirror's null position, its effects can be mitigated by first averaging the two sides of an interferogram, and then taking the Fourier cosine transform of the averaged one-sided interferogram. The resulting spectrum is many orders of magnitude below the expected B -mode signal, which shows amplitudes for $0.01 < r < 0.1$.

null. We then introduce the steps that can be taken to symmetrize the interferogram before taking its Fourier transform. We assume that the apodization function $A(\ell)$ is symmetric about the null and neglect its contribution to the resultant spectrum. For cases where both the interferogram and the apodization function are asymmetric, see [101].

If the interferogram does not have a sample at the null position, then we employ the Fourier shift theorem and the power measured by the detector is given by

$$\tilde{\mathbf{P}}_x^L(\ell) = \int_{-\infty}^{\infty} \mathbf{S}_x^L(\nu) \cos(2\pi\nu\ell + \varphi(\nu)) d\nu, \quad (3.76)$$

where $\varphi(\nu)$ is an asymmetric phase factor that follows $\varphi(-\nu) = -\varphi(\nu)$.

For a linear offset from the null position, the phase factor is given by

$$\varphi(\nu) = 2\pi\nu\Delta\ell, \quad (3.77)$$

where $\Delta\ell$ now corresponds to the displacement of the zeroth sample from the null position. Then the measured power can be re-expressed as

$$\tilde{\mathbf{P}}_x^L(\ell) = \int_{-\infty}^{\infty} \mathbf{S}_x^L(\nu) \exp(-2\pi i\nu\Delta\ell) \times \exp(-2\pi i\nu\ell) d\nu. \quad (3.78)$$

The interferogram is no longer symmetric, so to compute the spectrum we must take the complete Fourier transform of the full two-sided interferogram. This gives:

$$\tilde{\mathbf{S}}_x^L(\nu) = \mathbf{S}_x^L(\nu) \exp(-2\pi i\nu\Delta\ell). \quad (3.79)$$

For $\Delta\ell \ll L$, $\tilde{\mathbf{S}}_x^L(\nu)$ can be expanded as a Taylor series. Expressed as the sum of the ideal spectrum and associated error terms, it is

$$\tilde{\mathbf{S}}_x^L(\nu) = \mathbf{S}_x^L(\nu) + \epsilon_{rx}^L(\nu) + i\epsilon_{ix}^L(\nu), \quad (3.80)$$

where the real and imaginary error terms $\epsilon_{rx}^L(\nu)$ and $\epsilon_{ix}^L(\nu)$, respectively, are given by

$$\epsilon_{rx}^L(\nu) = \mathbf{S}_x^L(\nu) (2\pi(\nu\Delta\ell)^2), \quad (3.81)$$

$$\epsilon_{ix}^L(\nu) = \mathbf{S}_x^L(\nu) (2\pi\nu\Delta\ell). \quad (3.82)$$

The real part of the error shows up in second order and is proportional to $(\nu\Delta\ell)^2$. Assuming a null offset $\Delta\ell$ of 10 μm (i.e., $\sim 1/2$ sample), this term will be ~ 5 orders of magnitude smaller than the measured spectrum near the peak brightness of the CMB (see Figure 3.7).

For an ideal FTS, the imaginary component of an interferogram contains no signal, but only instrument noise. In this case, the imaginary part of the error provides a direct measurement of the phase factor $\varphi(\nu)$. This measurement allows us to symmetrize the measured interferogram such that we can recover the incident spectrum by applying the Fourier cosine transform to half the interferogram. The symmetrization process has important implications with regards to minimizing non-linear noise [99, 100].

To symmetrize the measured interferogram, we first define $\varphi(\ell)$ as the Fourier transform of the phase term, where up to some constant,

$$\varphi(\ell) = \int_{-\infty}^{\infty} \exp(2\pi i\nu\Delta\ell) \exp(-2\pi i\nu\ell) d\nu. \quad (3.83)$$

From our measurement of the imaginary component of the error, this will be a known quantity.

Next we take the convolution of the measured asymmetric interferogram $\tilde{\mathbf{P}}_x^L(\ell)$ and the phase term $\varphi(\ell)$:

$$\bar{\mathbf{P}}_x^L(\ell) = \tilde{\mathbf{P}}_x^L(\ell) \star \varphi(\ell). \quad (3.84)$$

$\bar{\mathbf{P}}_x^L(\ell)$ is symmetric about the null position, and from its Fourier cosine transform we compute $\mathbf{S}_x^L(\nu)$. Assuming that the zeroth sample offset $\Delta\ell$ is, to first order, constant the symmetrization process can be accomplished on a large subset of data from the measurement of a single two-sided interferogram. This process has been demonstrated in practice on measurements made by the *FIRAS* instrument that flew on the *COBE* satellite [104]. In fact, corrections to *FIRAS* data were successfully implemented that reduced the effective offset $\Delta\ell$ to the $1 \mu\text{m}$ level. We expect better performance from the lower-noise *PIXIE* data.

3.5.1.4 Misaligned transfer mirrors

When the transfer mirrors are misaligned, the phase difference ϕ between beams is not well-defined. Instead, the actual phase difference $\tilde{\phi}$ is given by all values in the range $\tilde{\phi} = \phi \pm \delta$, where 2δ is the optical path difference between light hitting opposite extrema of a misaligned optical surface. If the right block of transfer mirrors is misaligned by some small angle $\Delta\theta$ about its vertical axis of symmetry, then the phase factor δ is given by

$$\delta \simeq r\Delta\theta, \quad (3.85)$$

where r is the radius of the transfer mirror and we used $\sin \Delta\theta \simeq \Delta\theta$.

The measured interferogram $\tilde{\mathbf{P}}_x^L$ will then be given by the convolution of the ideal interferogram and a square pulse of unity amplitude and width δ . Taking the Fourier transform gives the measured spectrum:

$$\tilde{\mathbf{S}}_x^L(\nu) = \text{sinc}(2\nu\delta) \mathbf{S}_x^L(\nu). \quad (3.86)$$

In order to prevent significant attenuation of the sky signal, the 3 dB point of the sinc function should be at a frequency of ~ 6 THz. For *PIXIE*, this corresponds to a misalignment angle $\Delta\theta \simeq 35''$. Considerably tighter constraints are routinely achieved in FTSs optimized for infrared spectroscopy [e.g., 99]. Likewise for *PIXIE*-sized mirrors a misalignment angle of $\sim 35''$ corresponds to a machining tolerance of $\sim 250 \mu\text{m}$. This is an order of magnitude larger than typical machine precision.

3.5.1.5 Conclusion

We show how phase errors affect the signal measured by *PIXIE*. Offsets in the apodization function and the position of the zeroth sample lead to asymmetries in the interferogram. Misalignments of transfer mirrors attenuate the signal at frequencies defined by the misalignment angle. We correct apodization error by taking the Fourier transform of the full stroke, resulting in a residual error term proportional to some high order in $\Delta\ell$ (Figure 3.6). We correct zeroth sample offsets by measuring the imaginary component of the spectrum and symmetrizing the interferogram prior to taking its Fourier transform. The residual error is orders of magnitude below *PIXIE*'s sensitivity floor (Figure 3.7). The constraint on transfer mirror alignment is weak relative to what is achieved in FTSs optimized for shorter wavelength spectroscopy.

3.5.2 Sampling errors

Sampling errors are systematic or random offsets in the positions of interferogram samples. These can be caused by mechanical uncertainties in the mirror's position or uncertainties in the timing of samples. In the following, we develop a model for sampling errors and quantify their effect on the measured interferogram.

We first determine the maximum position error that allows foreground measurements to better than 0.01% and compare this requirement to the measured performance of a prototype MTM we built. Then following the methods by [104], we look

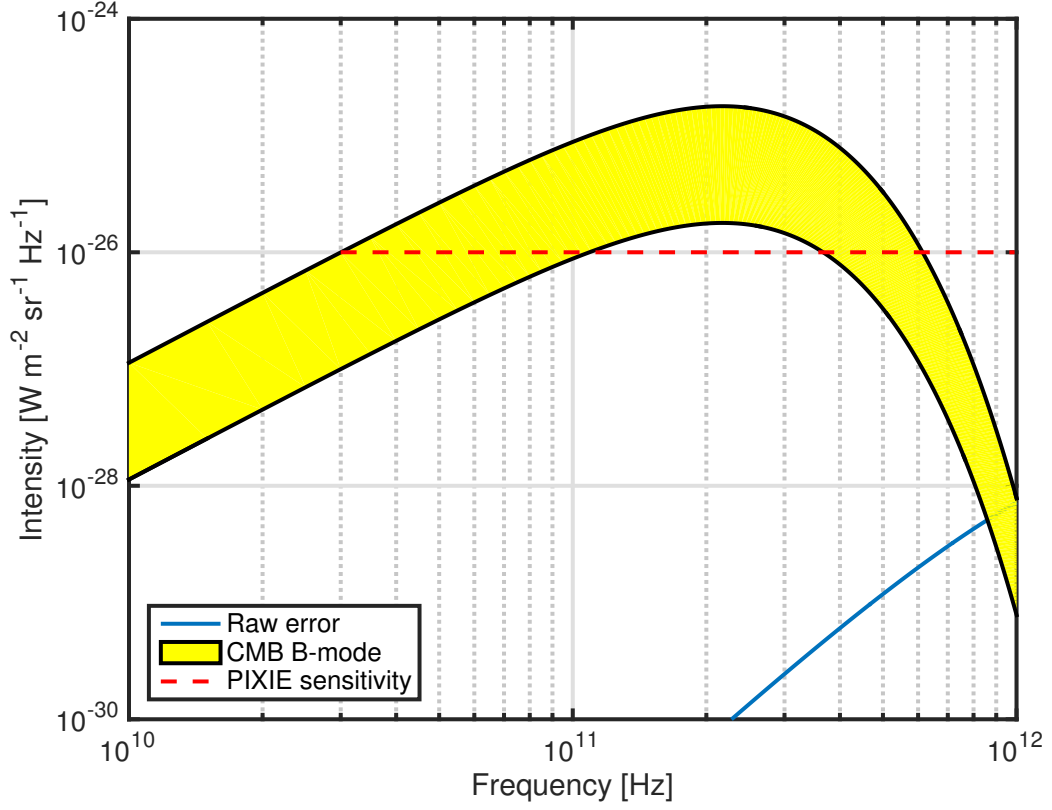


Figure 3.7 Sampling error spectrum due to a zeroth sample offset or instrumental vibrations. While the CMB signal is proportional to \mathbf{B}'_{ν, T_0} , the error signal is proportional to $\mathbf{B}'_{\nu, T_0} \nu^2$. We assume that the amplitude of the deviations or vibrations is $\Delta \ell = 1 \mu\text{m}$. The residual error after corrections is below the scale of this plot. The B -mode band shows amplitudes for $0.01 < r < 0.1$.

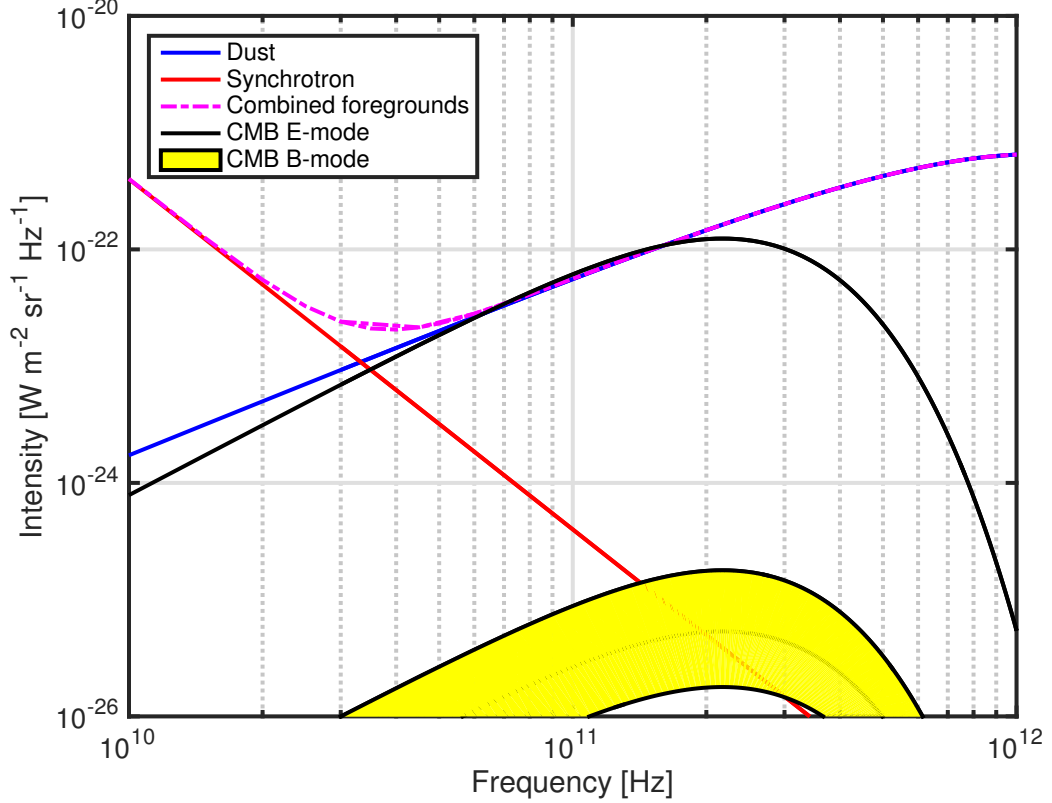


Figure 3.8 Model difference spectrum we expect to measure with *PIXIE*. The brightness temperature of each component is derived from [88]. The *B*-mode band shows amplitudes for $0.01 < r < 0.1$.

at two specific subclasses of sampling errors: errors in *PIXIE*'s absolute frequency scale and uncertainty in the MTM position.

3.5.2.1 Position errors

To quantify the magnitude of MTM errors that we can tolerate, we consider a sample difference spectrum that we expect to measure with *PIXIE*. In the model we include polarized emission from the CMB, galactic synchrotron radiation and thermal dust. Estimates of the brightness temperature of each component are derived from [88]. The model is shown in Figure 3.8.

The Fourier transform of the foreground spectrum gives the interferogram that *PIXIE* measures. From the derivative of the interferogram, we calculate the maximum

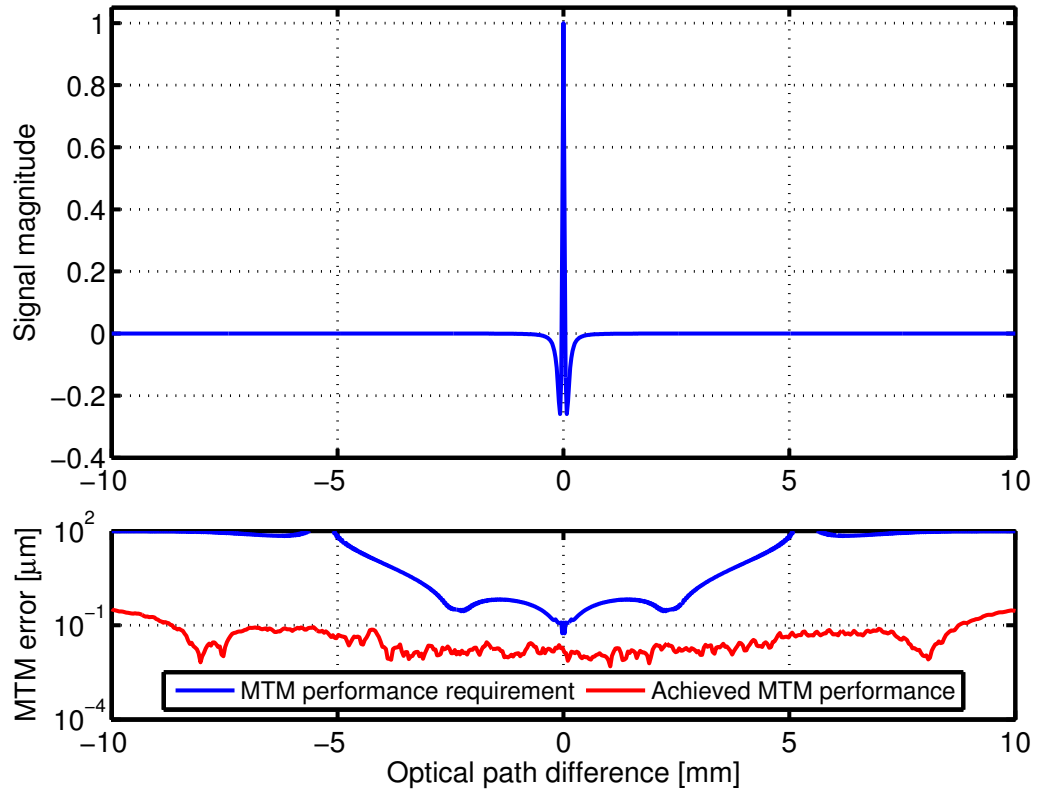


Figure 3.9 Interferogram showing the Fourier transform of the composite foreground spectrum (top, see Figure 3.8) and the single-pixel MTM position error requirement that gives us 0.01% accuracy in foreground intensity measurements (bottom). The blue curve shows the required performance, and the red curve shows the average measured performance of a prototype MTM that we built.

MTM position error that enables measurements of the polarized foregrounds to 0.01%, enabling accurate subtraction of foregrounds at the frequency of the CMB’s peak brightness. This result, along with the average measured performance of the prototype MTM, is shown in Figure 3.9. The residual foreground spectrum, after subtracting it to a part in 10^4 , is shown in Figure 3.10.

We do not require sub- μm position accuracy on every stroke, but rather we require the average error to be small, as in Figure 3.8. In addition, because most of the information about the CMB is near the center of the interferogram, we are especially tolerant of position errors near the extrema of the MTM stroke. In our tests, these errors could exceed $2\ \mu\text{m}$, but our requirements are an order of magnitude higher.

3.5.2.2 Frequency scale errors

Frequency scale errors can result from thermal contractions of the scale used to determine the MTM’s position. They can also result from optical beam divergence in the FTS. Such errors translate to temperature errors in the observed spectrum, and are easily corrected by observing known interstellar emission lines (See Section 2.3.5). This technique has been demonstrated in practice; from interstellar line emission calibration, errors in the *FIRAS* frequency scale were corrected to the 0.1% level [104]. This corresponds to position errors of $\sim 10^{-3}\ \mu\text{m}$, well below our requirements (see Figure 3.8).

3.5.3 Harmonic oscillations of the instrument

In the ideal case, the interferogram measured by the detectors is given by Equation 3.64. In the presence of harmonic instrumental vibrations, it becomes

$$\tilde{\mathbf{P}}_x^L(\ell) = \int_{-\infty}^{\infty} \mathbf{S}_x^L(\nu) \exp(-2\pi i\nu\delta\ell) \times \exp(-2\pi i\nu\ell) d\nu. \quad (3.87)$$

Here $\delta\ell = \Delta\ell \sin(\omega t + \phi)$, where $\Delta\ell$ is the amplitude of the vibration-induced perturbation to the mirror position, ω is the angular frequency of the perturbation, and ϕ is its phase. The perturbation can either come from vibrations in the MTM's physical position or from sample timing errors since $\ell(t) = vt$, where v is the speed of the MTM and t is the sample time. Both can result from harmonic vibrations of the instrument [104].

The measured spectrum $\tilde{\mathbf{S}}_x^L(\nu)$ is computed by taking the complete Fourier transform of the two-sided interferogram:

$$\tilde{\mathbf{S}}_x^L(\nu) = \mathbf{S}_x^L(\nu) \exp(-2\pi i \nu \Delta\ell \sin(\omega t + \phi)). \quad (3.88)$$

For small perturbation amplitudes, where $\Delta\ell$ is much smaller than typical sample spacing, the measured spectrum given by Equation 3.88 is expanded as a Taylor series. Keeping terms through second order in $\Delta\ell$, it is

$$\tilde{\mathbf{S}}_x^L(\nu) \simeq \mathbf{S}_x^L(\nu) (1 - 2\pi i \nu \Delta\ell \sin(\omega t + \phi) - 2\pi^2 \nu^2 \Delta\ell^2 \sin^2(\omega t + \phi)). \quad (3.89)$$

On average, the imaginary component of the above expression will be zero. Then the measured spectrum is real and can be expressed as the sum of the ideal spectrum and an error term:

$$\tilde{\mathbf{S}}_x^L(\nu) = \mathbf{S}_x^L(\nu) + \epsilon_x^L(\nu), \quad (3.90)$$

where the error is given by

$$\epsilon_x^L(\nu) = -\mathbf{S}_x^L(\nu) (\pi \nu \Delta\ell)^2. \quad (3.91)$$

This error shows up in second order in $\Delta\ell$ and will be several orders of magnitude

smaller than the ideal signal spectrum. Furthermore, it is proportional to ν^2 so it has different spectral content from the sky signal. The solution used to correct this error from *FIRAS* [104] is available for *PIXIE* data.

3.5.3.1 Conclusion

In this section we consider the role of frequency scale errors and vibration-induced perturbations to the sample location. To correct for the former, we calibrate the frequency scale by observing interstellar line emission. Correcting for the latter to acceptable levels is accomplished by averaging interferograms, causing the imaginary component to drop out and leaving a symmetric interferogram whose spectrum can be computed with the Fourier cosine transform. The results of this analysis are shown in Figure 3.7.

3.6 Spin-synchronous errors

Long term drifts in instruments have many sources, from temperature changes, to radiation damage, to outgassing. Here we are encouraged by the *FIRAS* experience which included only a single source of drift attributed to the helium defusing out of one of the thermometers on the external calibrator. Long term drifts on *PIXIE* can be detected (and corrected) by observing the calibrator. Random drifts are not confused with polarization. Only spin synchronous drifts (specifically those at twice the spin rate) are coupled to the polarization modulation provided by the spin. These could be modulated by thermal effects as the spacecraft rotates in the sunlight, or magnetic effects.

In this section we treat errors which occur at the fundamental frequency or at higher harmonics of the spacecraft's rotation. Polarized light incident on the *PIXIE* FTS and measured by the detectors will be amplitude modulated at twice the space-

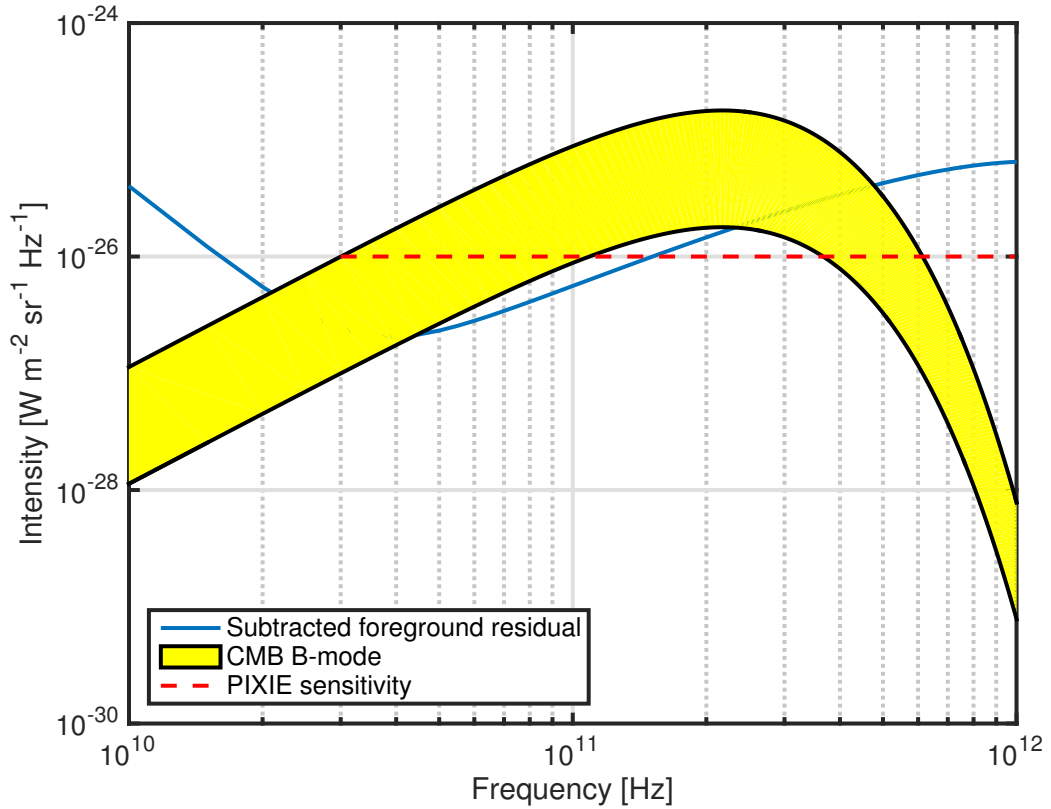


Figure 3.10 Effect of sample position errors on foreground subtractions. We require that sampling errors be small enough that we can measure foregrounds to better than 0.01%, enabling accurate foreground subtraction at the peak brightness of the CMB. The *B*-mode band shows amplitudes for $0.01 < r < 0.1$.

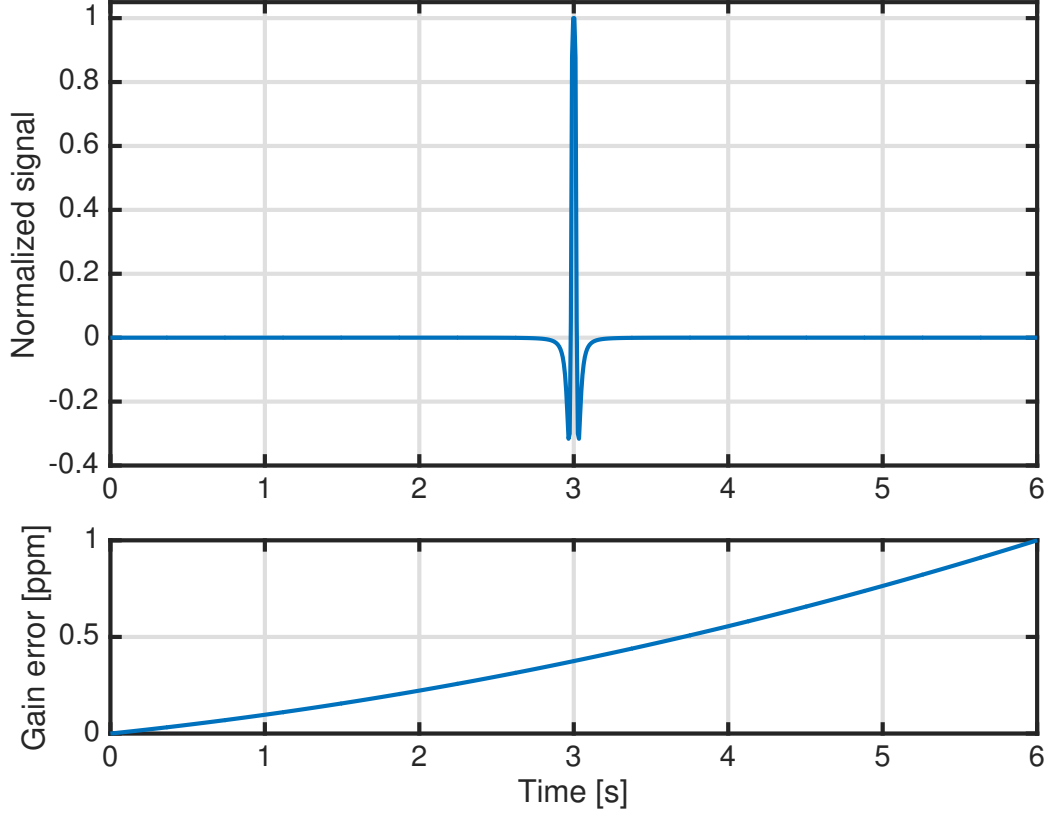


Figure 3.11 Model interferogram exhibiting gain error. This interferogram is the Fourier transform of a typical sky signal multiplied by some gain error. Because most of the information about the CMB is contained in $\sim 25\%$ of any given interferogram, a drift $\Delta G/G = 1 \times 10^{-6}$ over the 6 seconds it takes to measure a two-sided interferogram corresponds to a drift $\Delta G/G \simeq 1 \times 10^{-7}$ in each interferogram’s critical region. The gain drift is easily corrected by averaging the two sides of the interferogram before taking its Fourier transform, identical to how we correct for asymmetries in the apodization function.

craft’s spin frequency (see Section 2.2.3). No spin-synchronous errors give rise to amplitude modulated signals that are confused with polarized sky signals. We use the example of spin-synchronous gain drifts to show how spin-synchronous errors show up in the measured signal and are corrected to acceptable levels.

3.6.1 Gain drifts

Spin-synchronous gain drifts can occur, for example, if the temperature of readout electronics varies as the spacecraft spins. As a FTS with multimoded detectors, *PIXIE*

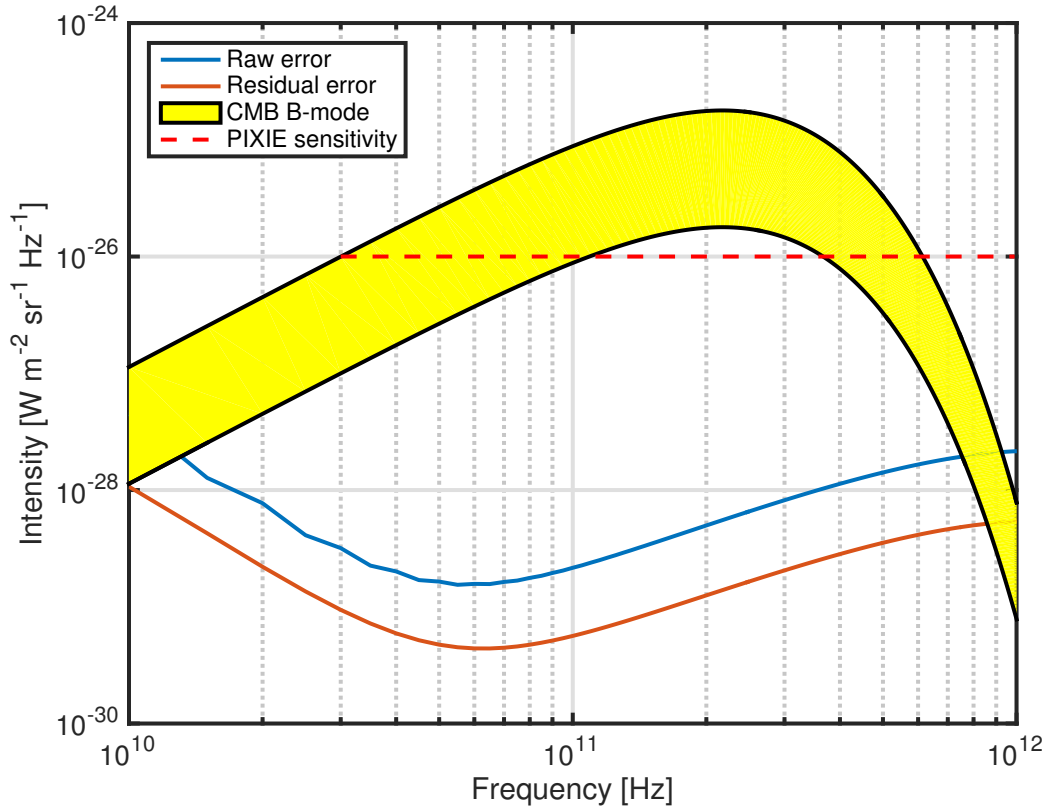


Figure 3.12 Error due to spin-synchronous gain drifts. We show the effect of gain errors on foreground subtraction. As expected, the gain errors that multiply the measured interferogram distort the spectrum in the first few frequency bins. The *B*-mode band shows amplitudes for $0.01 < r < 0.1$.

is particularly well equipped to deal with such effects. Imagine a case where the gain G drifts at the instrument's spin frequency. This would occur if the electronics were on one side of the spacecraft, going through one thermal cycle per each 1 minute rotation. Because independent measurements of the sky occur every three seconds, we model such a drift as a low order polynomial that multiplies the measured interferogram.

An example two-sided interferogram that exhibits a gain drift is shown in Figure 3.11. It shows the Fourier transform of a typical sky signal (Figure 3.8) multiplied by a gain drift. We allow a gain drift $\Delta G/G = 1 \times 10^{-6}$ over the six seconds required to take the measurement. This value is based on performance achieved by *DMR* on *COBE*. In low Earth orbit, *DMR* observed no evidence for spin synchronous gain errors at levels greater than $\Delta G/G \simeq 1 \times 10^{-5}$ [105]. *FIRAS* published no evidence of spin-synchronous gain drifts, therefore we take *DMR*'s performance to be a relevant published limit. Spinning ~ 1.25 times faster than *COBE*, *PIXIE*'s spin-synchronous gain drifts should be a factor of ~ 1.25 smaller for a complete rotation. But one *PIXIE* measurement takes 3 seconds, so we expect an order of magnitude improvement over *DMR* for a given measurement.

Before taking corrective actions, we make several observations that illustrate why *PIXIE* is particularly tolerant of gain errors. First, because periodic gain variations are well approximated by a low order polynomial that multiplies the interferogram, gain error will show up only in the first few frequency bins of the spectrum, away from the peak brightness of the CMB. This is a significant advantage over instruments where different frequency channels with separate detectors and read out schemes are each subject to independent gain drifts. Second, gain errors will affect both polarized and unpolarized signals in the same way, whereas only polarized signals are amplitude modulated by spacecraft rotation. Thus deploying the calibrator enables us to measure gain drifts.

Corrections to gain error are made by averaging two consecutive single-sided in-

terferograms before taking the Fourier transform. This works because the gain curve will average to nearly a constant value over the relevant timescales. For foreground measurements, the residual gain error near the peak brightness of the CMB is at the 10^{-11} K level, well below *PIXIE*'s sensitivity floor of a few nK (see Figure 3.12). In practice, we expect to do better than this by measuring the gain curve with the calibrator deployed.

3.6.2 Conclusion

In this section we examined spin-synchronous effects, noting that the absence of amplitude modulation at the frequency of spacecraft rotation means a given signal is not polarized. Taking the specific example of spin-synchronous gain drifts, we show that uncorrected, gain errors give a signal that is much smaller than the expected *B*-mode signal. Averaging a two-sided interferogram before taking the Fourier transform suppresses spin-synchronous gain error by an additional order of magnitude. Other spin-synchronous effects can be treated in a similar way, largely because the rotational period of the instrument (1 minute) is much longer than the time it takes to make an independent measurement of the CMB (~ 750 ms).

3.7 *PIXIE* as a two-element radio array

The standard treatment of *PIXIE*'s measured signal (Equation 3.6) ignores the spatial separation between its two primary mirrors. Taking the separation into account, we may think of *PIXIE* as a two-element radio interferometer. Here we model *PIXIE* as such, solving for its interferometric response to the Stokes parameters of the sky. We show that there is no interferometric response to Stokes *I* and *Q* in instrument-fixed coordinates. The interferometric response to Stokes *U* and *V* in instrument-fixed coordinates shows up in the Fourier sine transform of the measured interferogram.

The response, however, is highly oscillatory and is anti-symmetric with regard to the beam pattern, so large scale cancellation will occur when integrating over *PIXIE*'s tophat beam pattern. In addition, because the interferometric response is limited to the imaginary component of the spectrum, it will not interfere with estimates of the ideal signal.

Light from a common source will travel a different path length to the two mirrors. This path difference gives rise to a phase difference between light incident on the mirrors. If we define the baseline separation between the mirrors as the vector \mathbf{b} , and the source position on the sky as the vector \mathbf{s} , then the phase factor $\beta(\nu)$ between beams is given by

$$\beta(\nu) = \nu\tau, \quad (3.92)$$

where τ is given by

$$\tau = \mathbf{b} \cdot \mathbf{s}/c. \quad (3.93)$$

With both beams open to the sky, the vectors E^L and E^R describe light incident on the left and right sides of the instrument, respectively:

$$\begin{aligned} E^L &= \mathcal{A}\hat{x} + \mathcal{B}\hat{y}, \\ E^R &= \mathcal{A} \exp(i\nu\tau)\hat{x} + \mathcal{B} \exp(i\nu\tau)\hat{y}. \end{aligned} \quad (3.94)$$

The power measured by the left side \hat{x} detector is then:

$$\begin{aligned} \tilde{\mathbf{P}}_x^L &= \frac{1}{2} \int \left((\mathcal{A}^2 + \mathcal{B}^2) + (\mathcal{A}^2 - \mathcal{B}^2) \cos\left(\frac{4\nu z}{c}\right) \right. \\ &\quad \left. + (\text{Im}(\mathcal{A}\mathcal{B}^*) \cos(\nu\tau) - \text{Re}(\mathcal{A}\mathcal{B}^*) \sin(\nu\tau)) \sin\left(\frac{4\nu z}{c}\right) \right) d\nu. \end{aligned} \quad (3.95)$$

Expressing Equation 3.95 in terms of the Stokes parameters, we get:

$$\tilde{\mathbf{P}}_x^L = \frac{1}{2} \int \left(I + Q \cos\left(\frac{4\nu z}{c}\right) + (V \cos(\nu\tau) - U \sin(\nu\tau)) \sin\left(\frac{4\nu z}{c}\right) \right) d\nu, \quad (3.96)$$

where the Stokes parameters I , Q , U , and V are given by:

$$\begin{aligned} I &= \langle \mathcal{A}^2 + \mathcal{B}^2 \rangle, \\ Q &= \langle \mathcal{A}^2 - \mathcal{B}^2 \rangle, \\ U &= 2 \operatorname{Re} \langle \mathcal{A}\mathcal{B}^* \rangle, \\ V &= 2 \operatorname{Im} \langle \mathcal{A}\mathcal{B}^* \rangle. \end{aligned} \quad (3.97)$$

Equation 3.96 consists of a DC term, a term modulated by the cosine of the mirror movement (the ideal interferogram), and a term modulated by the sine of the mirror movement (the interferometric response). Several factors combine to make the interferometric response term small. The millimeter sky is dominated by the CMB and diffuse dust cirrus, neither of which is thought to emit circular polarization, so we can neglect the term proportional to Stokes V . The term proportional to Stokes U will be dominated by CMB E -mode polarization and diffuse foreground emission. To estimate its magnitude, we integrate the Stokes U term over the primary beam pattern.

Since the baseline \mathbf{b} separating the two mirrors is normal to the antenna boresight, the phase lag τ will vanish for a point source on axis and it is anti-symmetric for off-axis sources. Expanding the sky signal in a polar coordinate system $[\theta, \phi]$ centered on the antenna boresight, the phase term is re-expressed as:

$$\begin{aligned} \nu\tau &= 2\pi \frac{b}{\lambda} \theta \cos(\phi) \\ &= \frac{\nu b}{c} \theta \cos(\phi), \end{aligned} \quad (3.98)$$

where θ is the radial distance from the boresight, ϕ is the angle from the centerline

connecting the two primary mirrors, and λ is the wavelength of light.

Substituting the polar coordinate phase term (Equation 3.98) into Equation 3.96 and integrating over the beam, we get the following response to Stokes U :

$$\tilde{\mathbf{P}}_x^L|_U = \frac{1}{2} \int \left(\int_{beam} U(\nu, \theta, \phi) \sin\left(\frac{2\pi\nu b}{c}\theta \cos(\phi)\right) d\theta d\phi \right) \sin\left(\frac{4\nu z}{c}\right) d\nu. \quad (3.99)$$

The beam integral in Equation 3.99 is frequency dependent, with the ratio b/λ ranging from $b/\lambda = 60$ at $\lambda = 1$ cm to $b/\lambda = 12000$ at $\lambda = 50$ μm . Then the phase term is highly oscillatory across the $\theta = 1.1^\circ$ tophat radius, so the sky structure $U(\theta, \phi)$ will largely cancel in the beam integral. In addition, we can totally eliminate *PIXIE*'s sensitivity to either Stokes U or V by deploying the calibrator.

3.8 Conclusion

Using *PIXIE* as an example, we demonstrate how systematic errors in a polarizing FTS designed for CMB observations arise, are identified, and are mitigated. In general, the corrective actions that mitigate systematic errors in *PIXIE* are simple. Emission errors are generally corrected by actively modulating and controlling the temperature of the optics and taking sums and differences of measured signals. Geometric errors are part of *PIXIE*'s optical efficiency and are measured with the calibrator. Errors from the MTM and spin-synchronous drifts are corrected by taking averages. The errors are easily identified because *PIXIE* is sensitive to their amplitude and spectral content (see Figures 3.13 and 3.14, and Table 3.1).

All residual errors are mitigated well below the predicted B -mode spectrum without placing unreasonable constraints on *PIXIE*'s design, construction, or observing strategy. *PIXIE* does not rely on mathematically exact cancellation of potential errors, but instead a series of inherent symmetries that need not be exact when mul-

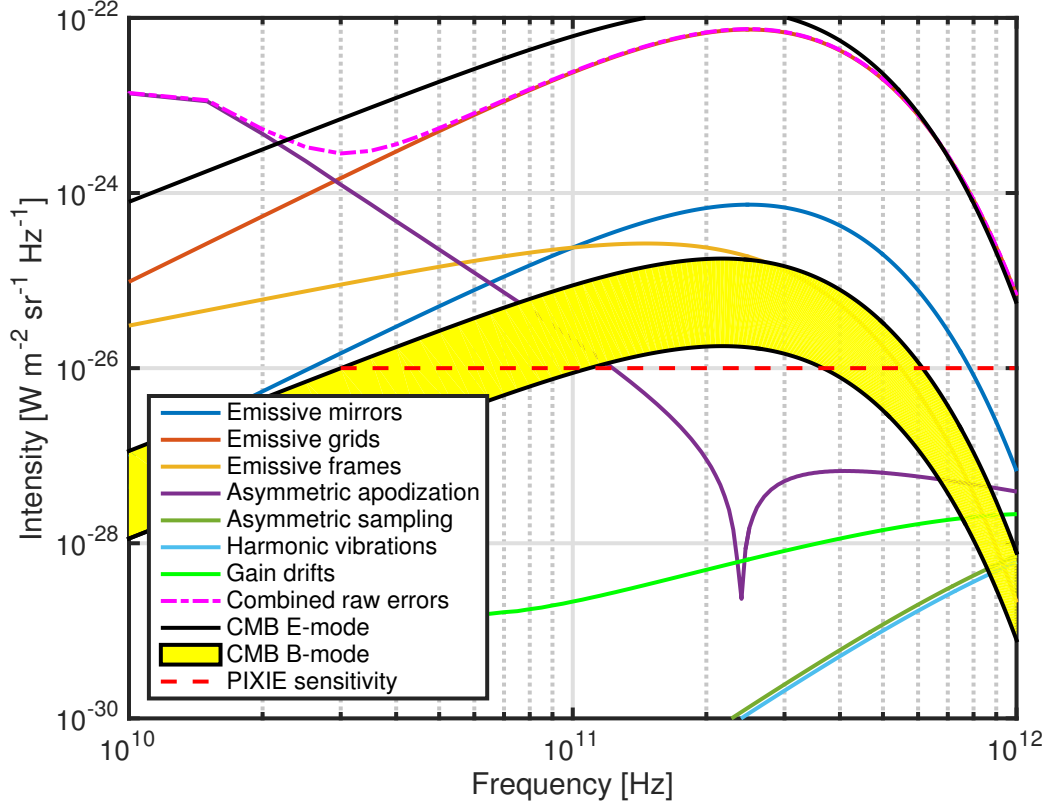


Figure 3.13 Spectra of the raw systematic errors and their combined spectrum.

tiplied together.

An instrument that demonstrates excellent control of systematic effects and has broad frequency coverage is best suited to measure the *B*-mode polarization of the CMB. With a factor of ~ 1000 fewer detectors and a factor of ~ 100 more frequency channels than state-of-the-art imagers, an instrument like *PIXIE* provides a simple, compelling, and proven avenue to accomplish this goal.

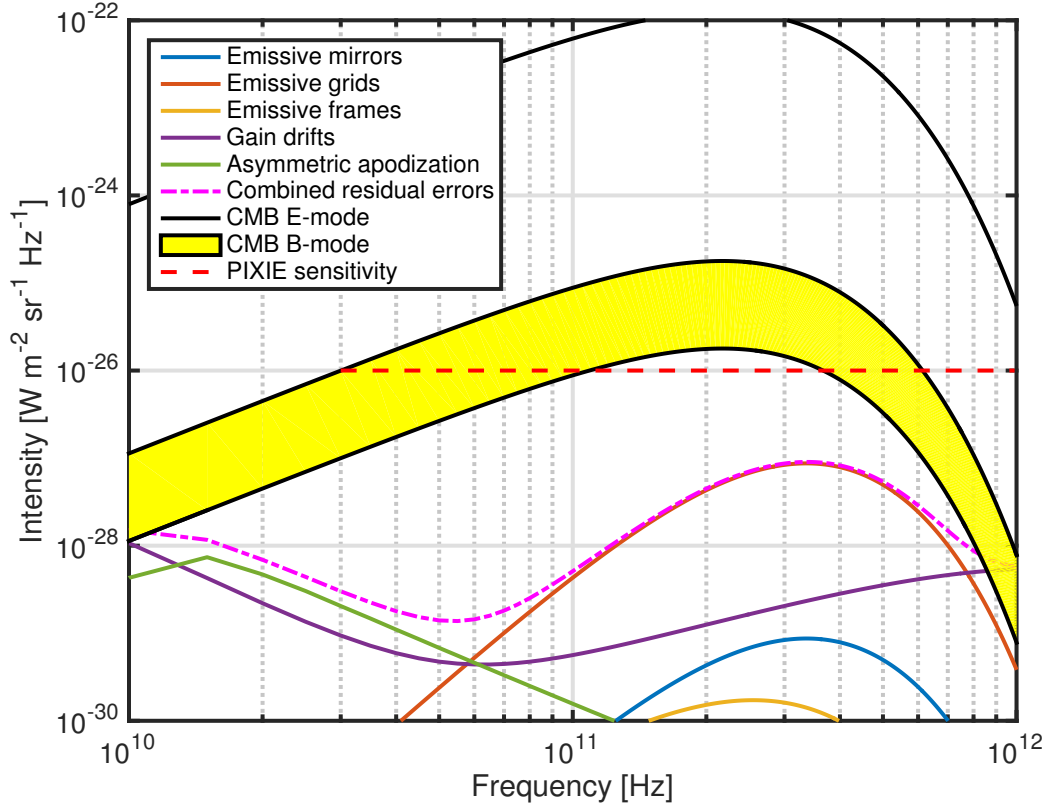


Figure 3.14 Spectra of residual systematic errors and their combined spectrum. Note that the residuals from asymmetric sampling and harmonic vibrations are below the scale of this plot. These results are summarized in Table 1. The *B*-mode band shows amplitudes for $0.01 < r < 0.1$.

Systematic error type	Raw level [K]	Mitigated level [K]	Section
Emissive mirrors	10^{-7}	10^{-12}	3.3.2
Emissive grids	10^{-5}	10^{-10}	3.3.3
Emissive frames	10^{-7}	10^{-12}	3.3.5.1
Asymmetric apodization	10^{-10}	10^{-13}	3.5.1.2
Asymmetric sampling	10^{-13}	10^{-15}	3.5.1.3
Harmonic vibrations	10^{-13}	10^{-15}	3.5.3
Gain drifts	10^{-11}	10^{-12}	3.6.1

Table 3.1 Systematic error magnitudes at 215 GHz before and after mitigation.

Chapter 4

Bolometers

4.1 Introduction

The majority of this chapter appears in [59]. As discussed previously, *PIXIE*'s design and experimental approach represent a significant departure from the focal plane imagers most commonly used for CMB measurements. This is especially true for the detectors. Instead of requiring several thousand diffraction-limited, ultra-low-noise detectors, *PIXIE* can achieve nK-scale sensitivity across 2.5 decades in frequency with just four multimode polarization-sensitive bolometers based on silicon thermistors. With a large etendue $A\Omega$ of $4 \text{ cm}^2 \text{ sr}$ per detector, the detectors are designed for a high optical load ($\sim 120 \text{ pW}$), but their noise equivalent power (NEP) is near the thermodynamic limit and is subdominant to photon noise from the CMB. Using high impedance silicon thermistor-based bolometers allows the use of simple and mature junction field effect transistor (JFET)-based voltage amplifiers. Developing detectors for a FTS with a large but mechanically robust absorbing area (~ 30 times that of *Planck*'s spider-web bolometers [106]), large enough bandwidth and appropriate geometry to measure optical frequencies from 30 GHz to 6 THz, and sufficiently low NEP ($\leq 1 \times 10^{-16} \text{ W}\sqrt{\text{Hz}}$) requires meeting a unique set of design, fabrication, and

performance criteria. These are described in this chapter.

4.2 Detector design and fabrication

4.2.1 Overview

A cartoon of a *PIXIE* bolometer and a cross sectional view of a hybridized pair of bolometers are shown in Figures 2.5 and 2.6, respectively. The bolometer fabrication and ion implantation are performed in the Detector Development Lab (DDL) at NASA/GSFC. The bolometer consists of an optical absorber structure coupled to silicon thermistor-based thermometers that operate at ~ 200 mK under optical and electrical bias. The thermometers are coupled to the chip frame held at the bath temperature (~ 100 mK). The absorber structure (Section 4.2.2) is a large-area (1.61 cm²) grid of freestanding, micromachined, degenerately doped silicon wires. The thermistors are located on silicon membranes (“endbanks”, Section 4.2.3) at either end of the absorber structure. Each endbank consists of a gold bar for thermalization and two thermistors that are independently biased and read out for laboratory characterization, but will be wired in series or parallel in flight in order to match resistances and minimize the number of readout and bias lines. The endbanks are coupled to the chip frame (Section 4.2.4) through a series of silicon legs. On the chip frame are wirebond pads for bias and readout of the thermistors and an array of indium bumps enabling the hybridization of a pair of bolometer chips. When hybridized, orthogonal absorbers will be separated by < 20 μm , such that the two bolometers will sample orthogonal polarizations of nearly the same electric field.

4.2.2 Absorber structure

Shown in Figures 4.1 and 4.2, the bolometer absorber structure consists of an array of parallel micromachined silicon wires that absorbs one linear polarization [107]. They

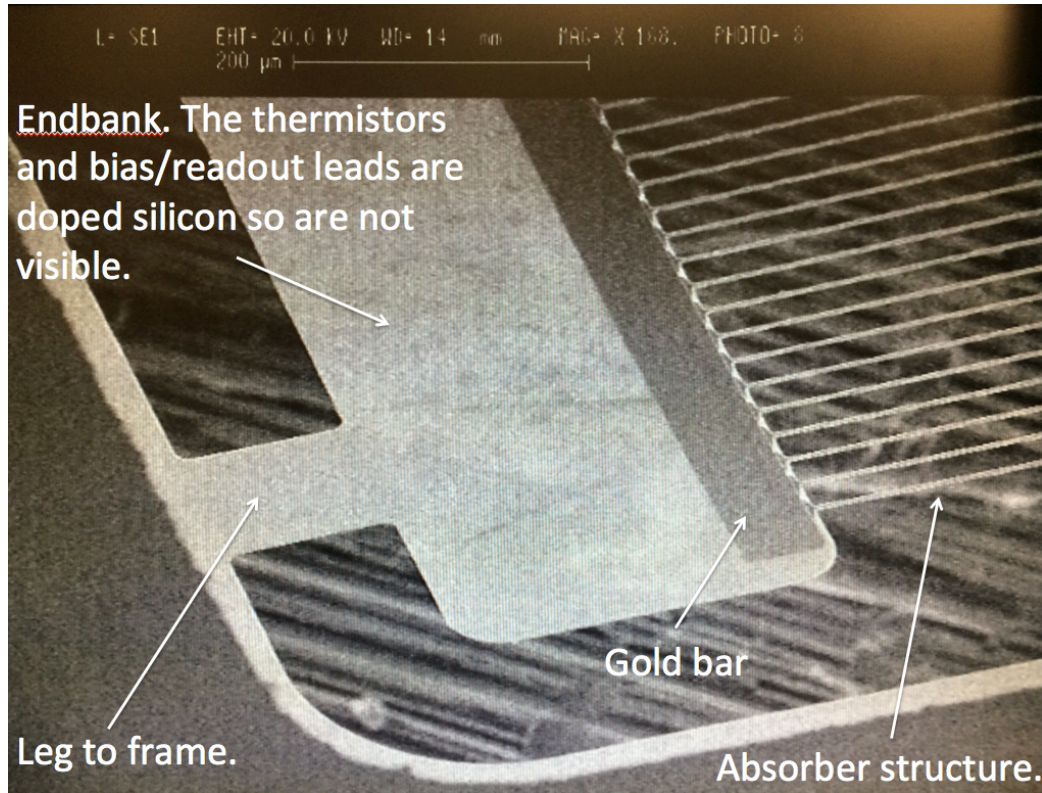


Figure 4.1 Scanning electron micrograph of a completed bolometer showing the interface between the absorber structure and the endbank.

are $3 \mu\text{m}$ wide, $1.35 \mu\text{m}$ thick, 15.8 mm long, and are on a $30 \mu\text{m}$ pitch, making them effective absorbers for frequencies up to $\sim 5 \text{ THz}$. The wires are degenerately doped with phosphorous to be metallic at all temperatures. The absorber structure's effective sheet resistance is designed to be $377 \Omega/\square$, impedance matching it to free space. The string width and thickness are highly uniform across the array. The thickness is set by the device layer thickness on the starting silicon-on-insulator (SOI) substrate, and they are etched to width with an inductively-coupled plasma (ICP) reactive ion etch (RIE) process.

In previous generations of devices, we found that the doping process induced compressive stress in absorber strings along the axis of absorption, causing individual strings to buckle and protrude $\pm 15 \mu\text{m}$ from the chip frame. This is problematic for a hybridized pair of chips which are separated by $< 20 \mu\text{m}$, since absorbers could

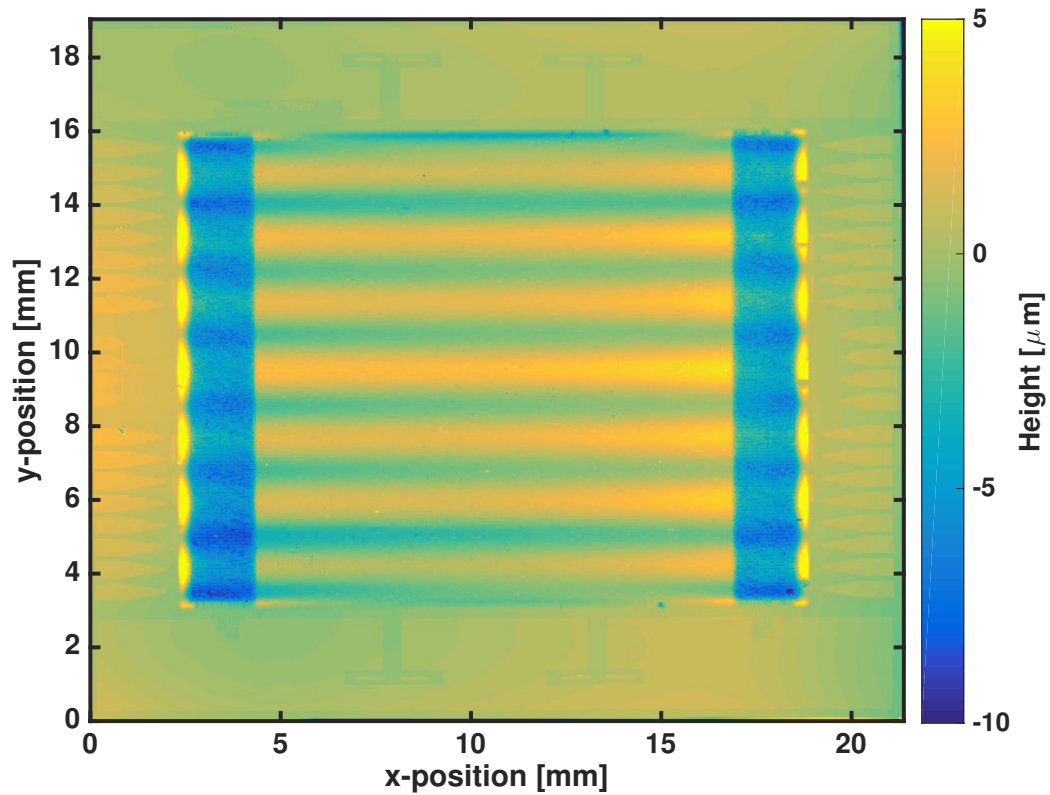


Figure 4.2 White light interferometer image showing the flatness of the absorber achieved after implementing the tensioning scheme. Along the \hat{x} -direction (the direction of absorption), the absorbers are flat to less than $2 \mu\text{m}$. The periodic structure visible along the \hat{y} -direction is set by the endbank leg placement, but with an amplitude of $< 5 \mu\text{m}$ and a period of several mm, they absorbers are essentially flat. The chip frame is visible around the edge of the image. Since the strings never protrude more than $\sim 5 \mu\text{m}$ above the frame, a hybridized pair can be offset by fewer than $20 \mu\text{m}$ without risk of strings colliding during launch.

collide and break, particularly during vibrations at launch. To prevent this, and to raise the resonant frequencies of the strings to well above the frequencies they will experience at launch, we deposited a highly-tensile Al_2O_3 film on individual strings outside the active absorbing area. This feature effectively pulls the strings taught (see Figure 4.2), and based on our elastic model should keep the amplitude of any string vibrations to less than $0.4 \mu\text{m}$ rms over the band of excitation frequencies expected during launch (20 Hz - 10 kHz).

We also estimated the bolometer sensitivity to cosmic ray hits. To minimize the impact of cosmic ray hits, the time constant of the absorber structure should be much shorter than the hit rate. Based on *Planck*'s measured hit rate [108], and scaling for our geometry, we expect one cosmic ray hit every two seconds. Measurements and thermal models of our absorber structure yield a time constant of a few ms, so particle hits can easily be flagged and removed during data processing without corrupting an entire interferogram.

4.2.3 Endbanks

Each bolometer chip has two endbanks, one at each end of the absorber structure (Figure 4.1). The endbanks consist of a gold bar for thermalization and two doped silicon thermistors on a crystalline silicon membrane. The gold bar also sets the heat capacity of the endbank. The endbank membrane is the same thickness ($1.35 \mu\text{m}$) as the absorber strings and is also formed from the device layer of the SOI substrate. Endbanks are connected to the chip frame through eight silicon legs.

The thermistors are doped to operate below their metal-insulator transition. The electron transport mechanism in this regime is variable range hopping (VRH) [109], which yields the following resistance-temperature relationship:

$$R(T) = R_0 \times \exp \sqrt{\frac{T_0}{T}}, \quad (4.1)$$

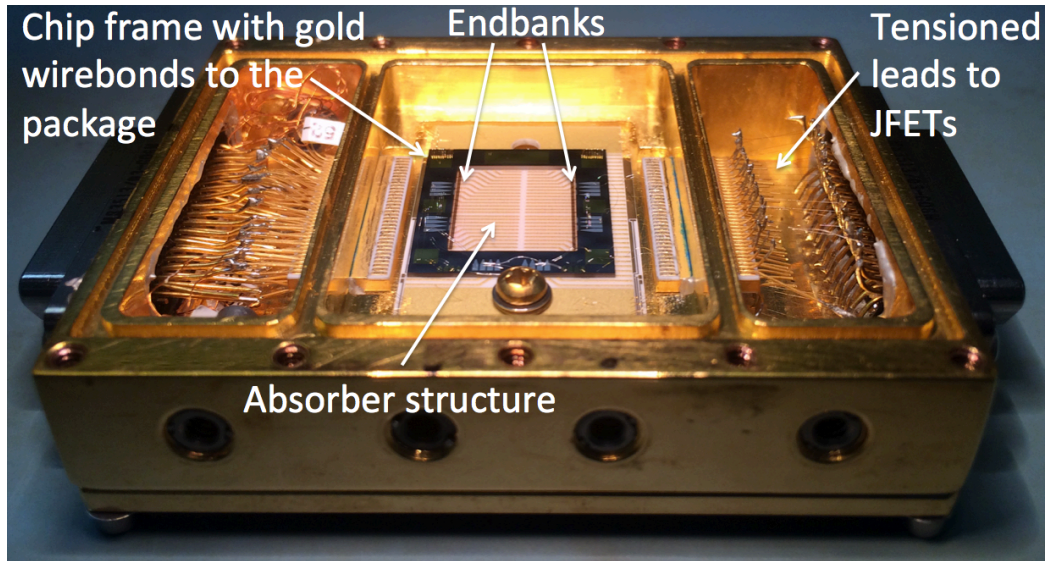


Figure 4.3 Single bolometer packaged for dark tests in the *Astro-E2/Suzaku* dewar. This bolometer was fabricated with 3/4-length absorbers, enabling it to fit in a package designed for an x-ray microcalorimeter array.

where R_0 and T_0 are constants determined largely by the device geometry and doping concentration, respectively.

We also developed a detailed thermal model of the endbank that takes into account heat flow between each thermal element (absorber strings, gold bar, thermistor and legs). This will be discussed in greater detail in Section 4.3.

4.2.4 Frame

The bolometer frame is maintained at the refrigerator bath temperature. Under normal operation, the bath will be kept at ~ 100 mK. The chip is maintained at this temperature through a series of gold wire bonds connecting gold heat sink areas on the chip to the package. The frame is designed such that any two bolometer chips can be indium bump hybridized together, though we can also characterize individual bolometers in the light or dark (Figure 4.3). The frame has several arrays of indium bumps. Some are designed for mechanical purposes, and others are electrical, allowing the thermistors on one chip to be read out through wirebond pads on the other chip.

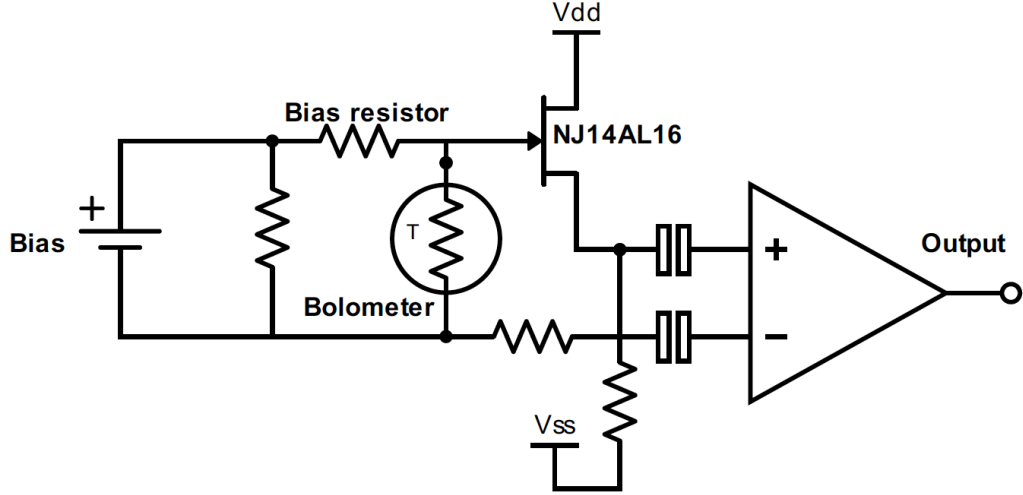


Figure 4.4 Basic bias and readout circuit used for dark detector characterization. This is not a complete schematic, but rather a representation of what is used. The bias resistor and bolometer operate at 100 mK. The JFET and voltage divider are at 130 K. The bias supply and final amplification stages are at room temperature.

4.3 Cryogenic detector performance

We measured detector load curves and noise in a dark cryogenic environment at a range of temperatures (100 – 2000 mK). A photograph of a packaged bolometer and a schematic of the basic bias and readout circuit are shown in Figures 4.3 and 4.4. The package, bias and readout system, and dewar were originally built to characterize the silicon thermistor-based x-ray microcalorimeters developed for the *Astro-E2/Suzaku* mission [110]. The thermistor is wired in series with a bias resistor. The bias resistor’s resistance is much greater than the thermistor’s operating resistance, so the thermistor is under current bias. Tensioned leads connect the bolometer to a cryogenic JFET amplifier, mitigating capacitive microphonic contamination of the signal band. For *PIXIE*, we use InterFET NJ14AL16 JFETs [111] that operate at 130 K in a source-follower configuration. These are the same model JFETs that were flown as part of the *XRS* instrument on *Astro-E2/Suzaku* [110] and the *SXS* instrument on *Astro-H/Hitomi* [112]. They convert the high source impedance of the thermistors ($M\Omega$ -

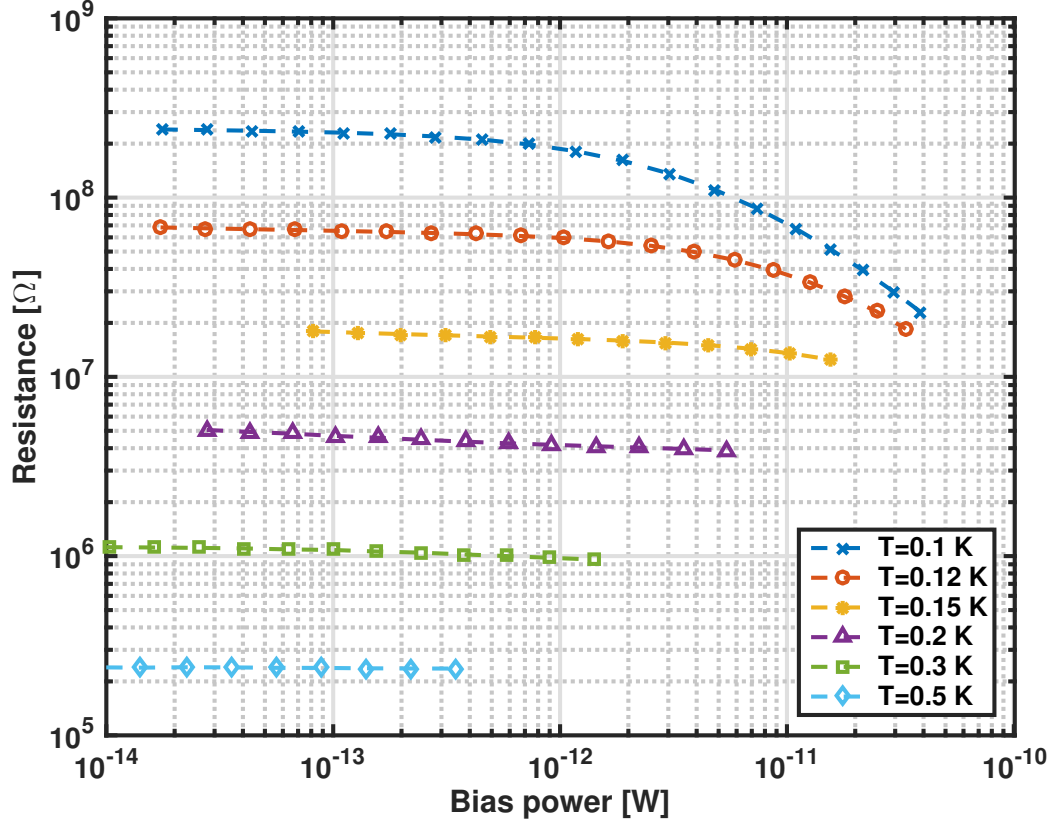


Figure 4.5 Series of measured load curves plotted to show the bolometer resistance E/I as a function of bias power $I \times E$, where E is the voltage drop across the thermistor and I is the thermistor bias current. Data are shown for a pair of thermistors wired in series on one of the two endbanks. The data from the other endbank are similar. Because the bias circuit is optimized for low temperature, high impedance operation, it could not supply enough current for us to observe thermistor self-heating at the higher bath temperatures. From the low bias resistances, where the thermistor is isothermal with the bath, we can extract the VRH parameters.

scale) to the low output impedance of the JFETs (1.8 k Ω). The JFETs have excellent noise performance ($i_n = 0.5 \text{ fA}/\sqrt{\text{Hz}}$ at 100 Hz, where i_n is the current noise spectral density). The low impedance signal is then AC coupled to a room temperature amplifier.

4.3.1 Load curves

A series of measured load curves is shown in Figure 4.5, plotted to show thermistor resistance as a function of bias power. From the measured resistances under low

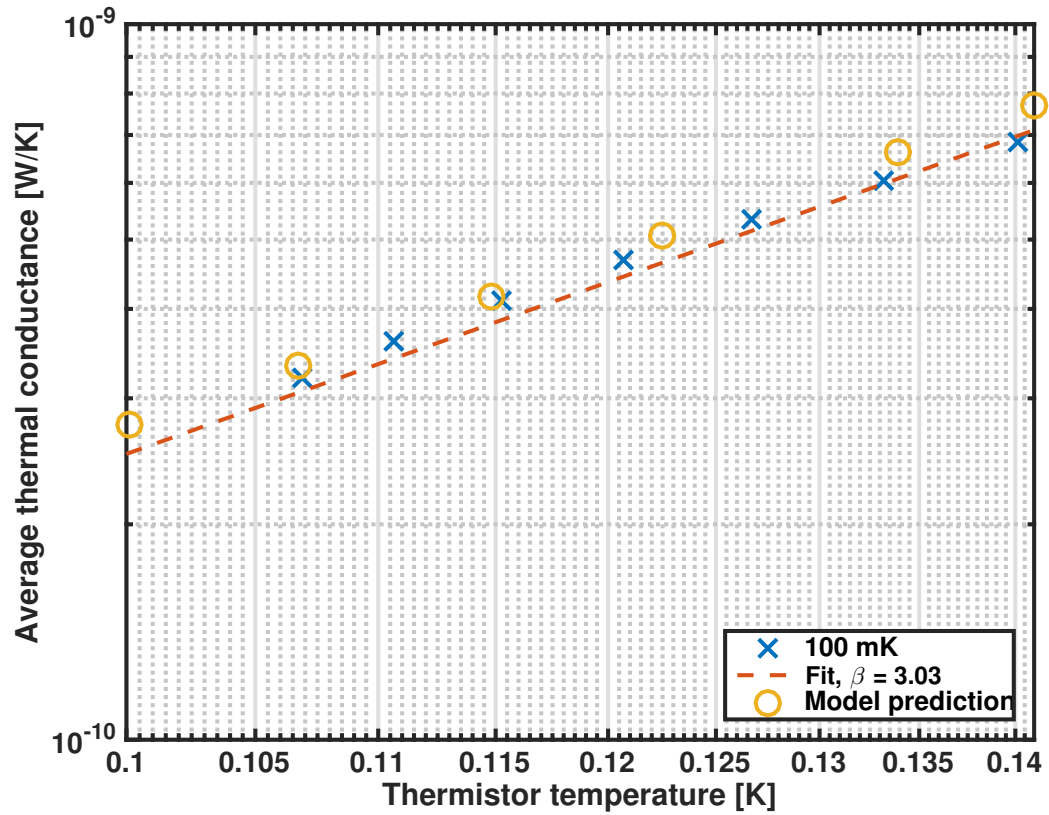


Figure 4.6 Average thermal conductance \bar{G} as a function of thermistor temperature. The legend shows the bath temperature corresponding to the measurement. Shown in circles is the model prediction.

electrical bias, where the thermistor is isothermal with the bath, we determine the VRH parameters R_0 and T_0 (Equation 4.1). For this device, fitting to the data gives $T_0 = 15.11$ K and $R_0 = 911 \Omega$. The expected operating resistance under optical bias is $5.42 \text{ M}\Omega$, matching well the measured noise impedance of the JFETs ($5.48 \text{ M}\Omega$).

The average thermal conductance \bar{G} between the thermistors and the bath is calculated from the high bias end of the load curves where self-heating is observed. In a steady state, the bias power P_{bias} is equal to the heat flow from the thermistor to the bath, so \bar{G} is given by

$$\bar{G} = \frac{P_{\text{bias}}}{T_1 - T_2}, \quad (4.2)$$

where T_1 is the thermistor temperature (calculated from Equation 4.1), and T_2 is the bath temperature. This is plotted for the 100 mK data in Figure 4.6. We then fit to the measured \bar{G} with a function $\tilde{G} = G_0 \times T^\beta$, shown in Figure 4.6. The fit is close to the expected value for phonon conduction at these temperatures ($\beta = 3$).

The DC electrical responsivity S_e is also determined from the load curves. Following the notation of Jones [113, 114], the responsivity is given by the following expression:

$$S_e = \frac{R - Z}{2IR}, \quad (4.3)$$

where R is the resistance E/I and Z is the dynamic resistance dE/dI , determined from the load curve. The measured responsivity S_e is plotted as a function of current I for a few temperatures in Figure 4.7.

We compared the measured bolometer characteristics to predictions from a thermal model that takes into account heat exchanges between the gold bar, the thermistors, and the legs. Given the endbank geometry, we solve for the etendue between each thermal component, then determine the heat flow between each of them. Heat

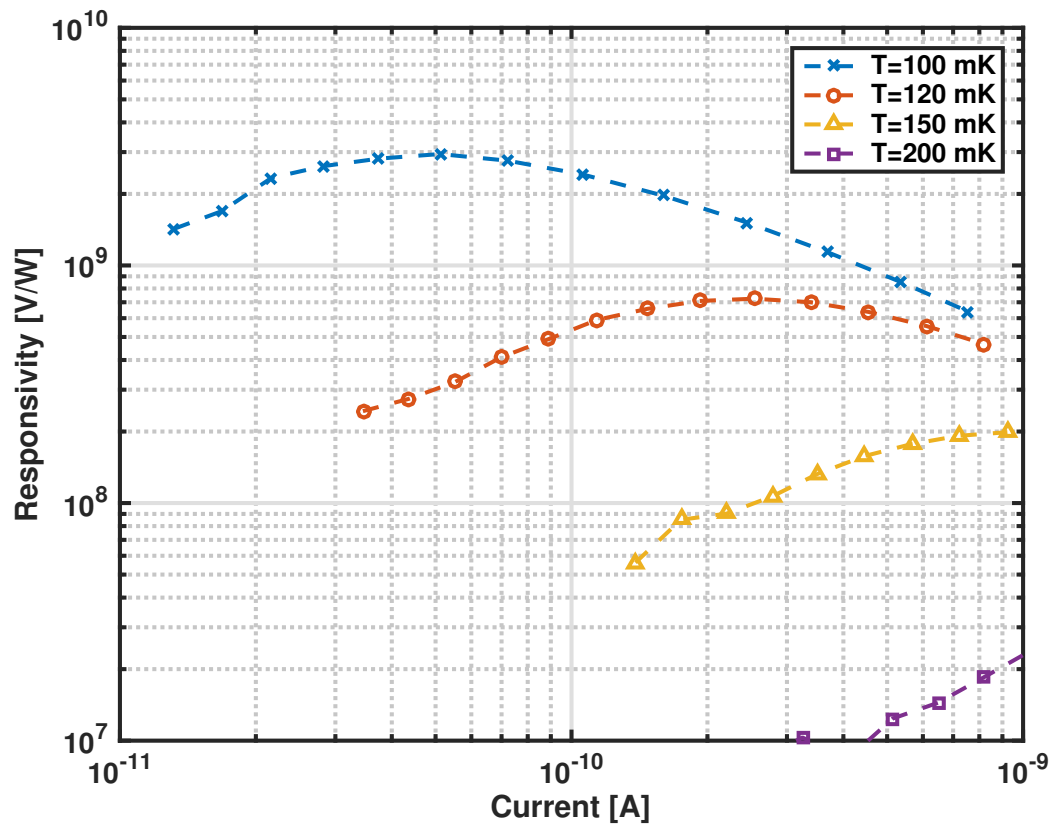


Figure 4.7 DC electrical responsivity S_e as a function of bias current for a few bath temperatures.

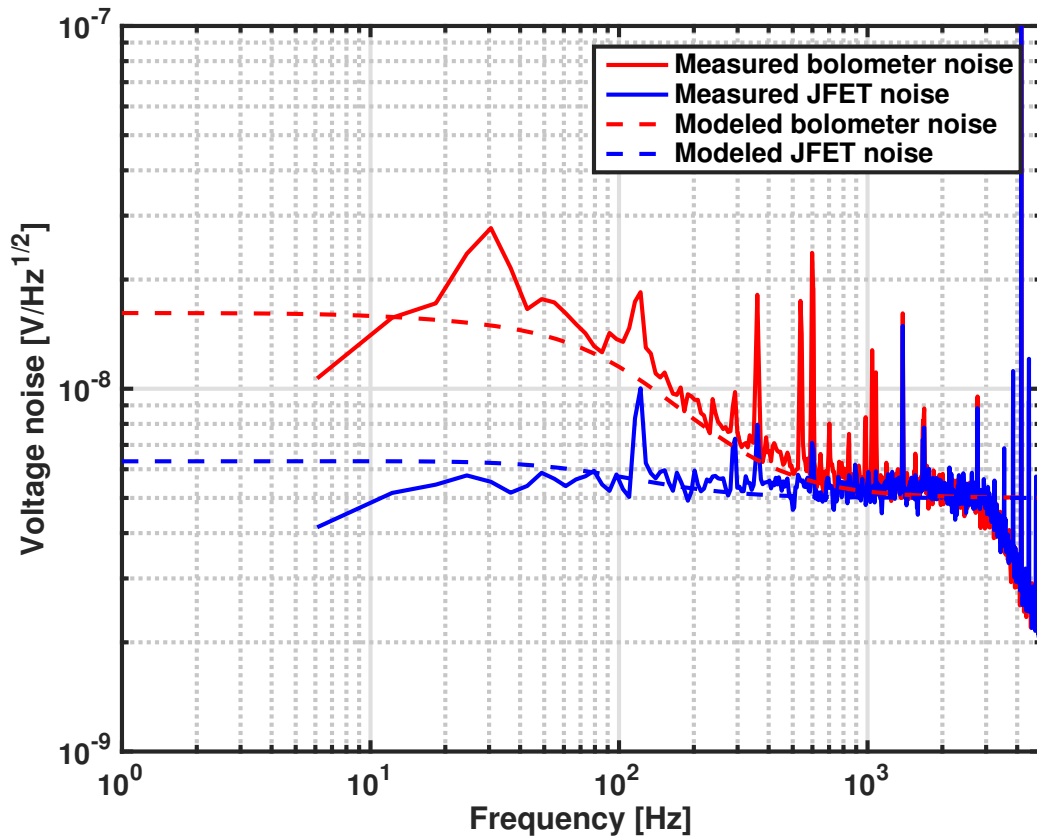


Figure 4.8 Measured noise spectrum along with the fit from our thermal model. Note that the measurement was AC coupled, so both measured signals drop off at low frequency. Running this model for the optical and electrical bias conditions in expected in flight, we calculate a bolometer NEP of $7.93 \times 10^{-17} \text{ W}/\sqrt{\text{Hz}}$. This is well below the expected photon noise from the CMB across the entire *PIXIE* bandwidth (see Figure 4.9).

flow between components on the endbank is via ballistic phonon conduction, where the phonon mean free path ℓ_{mfp} is much greater than the endbank dimensions. This assumption is based on thermal transport measurements made on far infrared microwave kinetic inductance detectors (MKIDs) [115], where ℓ_{mfp} in silicon at 100 mK was measured to be ≥ 1 mm [116]. For heat flowing out of the legs, we account for a mean free path reduction due to phonon scattering off the leg edges. The model is then used to predict the DC thermal conductance (Figure 4.6) and the noise (Section 4.3.2).

4.3.2 Noise analysis

Noise spectra were measured at a range of temperatures and bias currents. When *PIXIE* observes the CMB the bolometers will operate under large optical bias (~ 120 pW). This results in a large temperature difference between the thermistors and the bath. It is therefore necessary to take into account non-equilibrium effects in the noise [65].

Accounting for non-equilibrium effects, the NEP of a simple bolometer in the dark is given by

$$\text{NEP}_{\text{bolometer}}^2 = \gamma_1 4k_b T^2 G + \frac{1}{S^2} \left(\gamma_2 4k_b T R + e_n^2 + \gamma_3 i_n^2 R + \gamma_4 \text{NEP}_{\text{excess}}^2 \right), \quad (4.4)$$

where the constants γ_1 , γ_2 , and γ_3 account for non-equilibrium effects, e_n^2 and i_n^2 are the amplifier's voltage and current noise spectral densities, and $\text{NEP}_{\text{excess}}$ accounts for other sources of noise, for example parasitic resistance in the leads or stray light. The factor of $1/S^2$, where S is the bolometer's electrical responsivity, refers the Johnson, amplifier, and excess noise to the bolometer's input. Multiplying the NEP^2 by S^2 gives the voltage power spectral density of the bolometer.

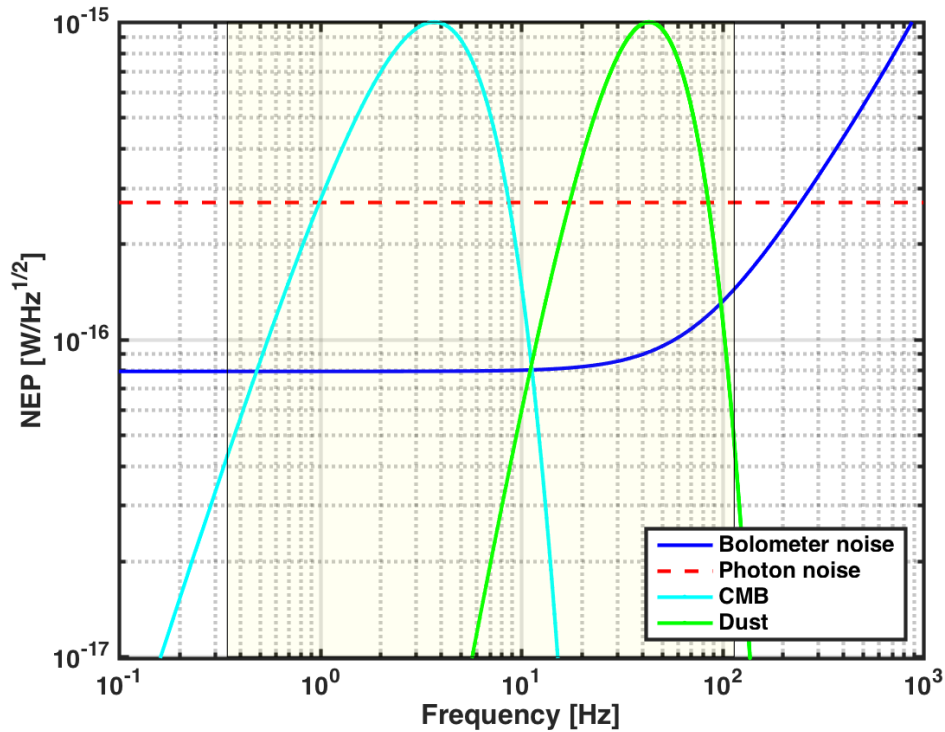


Figure 4.9 Predicted bolometer NEP calculated for the optical and electrical bias conditions in expected in flight. The shaded region shows the *PIXIE* FTS band. The instrument is photon noise limited across the entire FTS band. Also plotted (not to scale) are the CMB and dust spectra to illustrate how radio frequencies from the sky map to audio frequencies in the *PIXIE* FTS. The values for the dust temperature and spectral index are based on results from the *Planck* experiment [117].

With relevant parameters taken from load curve analysis (Section 4.3.1), and accounting for non-equilibrium effects, we calculated the expected bolometer noise under a few bias conditions, and compared them to measured noise spectra. An example noise spectrum and fit is shown in Figure 4.8. Fits are consistently good for multiple measured bias conditions. Running the model for the bias conditions expected during flight, we expect to be photon noise limited across the entire *PIXIE* bandwidth (Figure 4.9).

4.4 Next-generation detector assembly

The data presented in this chapter were taken in a setup originally designed to test thermistor-based x-ray microcalorimeters built for the *Astro-E2/Suzaku* mission [110]. The *Astro-E2* thermistors have similar operating characteristics to the *PIXIE* bolometers, but some design constraints for that application do not apply to *PIXIE*, and vice versa. For example, the *Astro-E2* detectors have 32 independent channels. Due to the bias power dissipated by individual JFETs in the cold front end amplifier (~ 3.5 mW), each pixel could only afford a single JFET. Better common mode rejection (CMR) and simpler circuitry could be achieved by employing a differential pair of JFETs per detector channel. With just 4 channels for the entire instrument, each *PIXIE* channel can have a differential pair of JFETs without excessive power dissipation.

The role of bandwidth is also different when comparing a *PIXIE* bolometer to an x-ray microcalorimeter. An absorbed x-ray is an impulse (delta function) in the detector's time stream. Therefore in the frequency domain, the signal's spectral content is white across the bandwidth of the detector. The microcalorimeters developed for *Astro-E2* were DC biased and they could achieve their desired sensitivity while losing some bandwidth (~ 15 Hz) to the $1/f$ noise of the JFETs. For *PIXIE*, however, different sub-bands correspond to different measured sky frequencies (see Figure 4.9). As a result the *PIXIE* detectors must be AC biased in flight to move the measured spectra to frequencies above the amplifier's $1/f$ knee. Otherwise the signal-to-noise ratio in the CMB band ($\omega \leq 15$ Hz) would be < 1 . To avoid microphonic contamination of the signal band, the tensioned leads for an AC biased detector must have a higher fundamental resonant frequencies than those for a DC biased instrument.

While the *Astro-E2/Suzaku* setup is capable of dark characterization of the *PIXIE* detectors, a different design optimized for *PIXIE* is required for the space mission. In this section, we report on the design, assembly, and initial tests of a *PIXIE*-specific detector assembly (DA) that we built. While not yet a flight-like prototype,

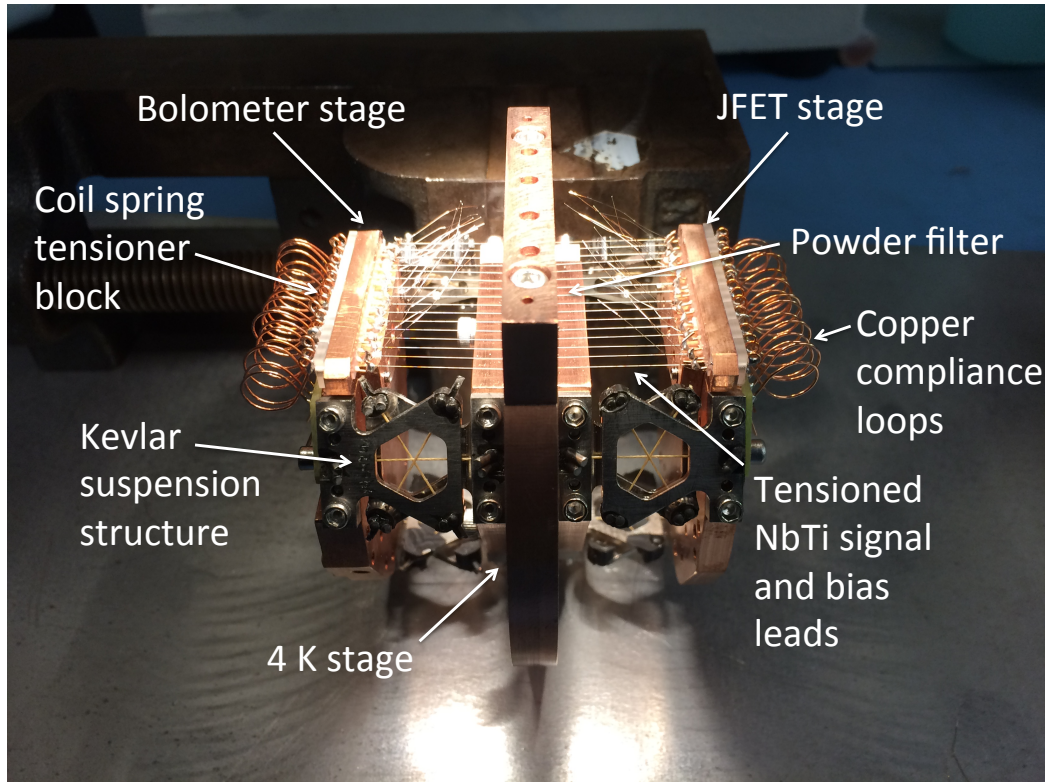


Figure 4.10 Next-generation *PIXIE* detector assembly with its main constituents highlighted. This photograph was taken after the tensioned leads were installed.

this detector assembly incorporates many of the design elements required for the flight mission, including tensioned leads that accommodate AC bias, fully differential readout with two JFETs per detector channel, and the ability to perform dark or optical characterization of a single detector or hybridized pair of detectors.

4.4.1 Overview

Shown in Figures 4.10 and 4.14, the detector assembly features three copper plates which are enclosed within a copper can. The plates operate at 3 different temperatures. The central plate is attached directly to the cryocooler stage of the refrigerator. It is thermally and mechanically coupled to the copper can. In the system used for initial tests, this stage maintained a temperature of ~ 2.6 K independent of loading. The amplifier plate is thermally isolated from the central plate by a series of Kevlar

suspensions. Under operation, the amplifier plate is heated to ~ 130 K, where the JFETs have a local minimum in their noise versus temperature. To keep the amplifier plate's time constant fast enough to control its temperature, two brass wires thermally short the amplifier plate to the central plate. The detector plate is thermally isolated from the central plate by Kevlar suspensions. A cold finger couples the detector plate to the coldest stage of the refrigerator. We used a two-stage ADR whose coldest stage can reach 30 mK. Under normal operation, the detector plate is maintained at 100 mK.

An amplifier circuit board mounts to the JFET plate. A 500 mW-rated surface mount resistor and a Cernox thermometer provide temperature control. The bias and readout harness, made of 3 mil diameter CuNi-clad stainless steel wire, is soldered directly to the board. Bare die JFETs, 16 mil on a side, are glued to the circuit board with Arathane. Gold wirebonds electrically connect the JFETs to the amplifier board.

Tensioned signal and bias leads go from the amplifier plate to the detector plate. The leads are 48 mm long. On either side of the central plate they are 20 mm long. The leads are made of 3 mil diameter CuNi-clad NbTi wire. Each wire (there are 16 in total) is held under tension with a pair of stainless steel coil springs, one on each end. The tensioned leads pass through a powder filter cast into the central plate. The powder filter consists of stainless steel powder bound by Loctite 493 super glue. The filter is 8 mm long and prevents the transmission of infrared radiation down the wires.

The bolometer circuit board mounts to the detector plate. A bolometer chip is fixed to the board with a pair of titanium spring clips. Bias resistors (2 per channel) are glued to the bolometer board with Arathane. The bias resistors have a nominal resistance of $40\text{ M}\Omega$. They are made of thin film SiCr on a quartz substrate. Electrical contact from the bolometer board to the bias resistors and bolometer is made with aluminum wirebonds.

4.4.2 Thermal design

We calculated the thermal loads between the JFET plate and the central plate, and also between the central plate and the bolometer plate. The results are shown in Tables 4.1, 4.2, and 4.3. Table 4.1 assumes that the powder filter has infinite thermal conductance and therefore sinks the tensioned leads at $T = 2.6$ K. Table 4.2 accounts for the finite thermal conductance of the powder filter, allowing it to be warmer than the central plate. Solving for the steady-state temperature of the powder filter, we find that it can reach a temperature as high as 16.51 K. Finally, Table 4.3 shows the behavior we expect should the tensioned leads be stripped of their CuNi cladding.

In the model, we consider heat flow through the NbTi wires, the CuNi cladding, and the Kevlar suspensions. Table 4.4 summarizes the relevant material parameters used in the calculations. Heat flow through normal metal (NbTi or CuNi) is calculated using literature values for the material's electrical conductivity and the Wiedemann-Franz law. Heat flow through superconducting metal (NbTi) and insulators (Kevlar, super glue) is calculated from literature values for the respective material's measured thermal conductivity in the relevant temperature range. Values for the formulation of super glue we used are unavailable in the literature, so we instead considered a range of measured values for epoxies. The calculated heat flow through the powder filter includes the Kapitza boundary resistance between the tensioned wires and the superglue, using literature values for this resistance at a Nb-epoxy interface [118]. It should be noted, however, that the Kapitza term is subdominant to the bulk term.

Not shown in the tables, we also account for heat flow by the emission and absorption of radiation. We are only concerned with radiation emitted by the JFET stage; radiation emitted by 2.6 K surfaces is negligible. Using the Stefan-Boltzmann law, and solving for the geometry of the JFET plate with an assumed emissivity of 50% for oxidized copper, we find the JFET stage emits 25 mW. While a significant heat load, it is easily handled by the cryocooler.

Heat flow from JFET stage (130 K) to powder filter (2.6 K)		Heat flow from powder filter (2.6 K) to bolometer stage (0.1 K)	
Material	Power [W]	Material	Power [W]
NbTi	6.44×10^{-4}	NbTi	2.78×10^{-7}
CuNi	3.20×10^{-3}	CuNi	1.27×10^{-6}
Kevlar	1.03×10^{-2}	Kevlar	6.48×10^{-7}
Total	1.41×10^{-2}	Total	2.20×10^{-6}

Table 4.1 Results of thermal model assuming that the powder filter is at $T = 2.6$ K.

Heat flow from JFET stage (130 K) to powder filter (16.51 K)		Heat flow from powder filter (16.51 K) to bolometer stage (0.1 K)	
Material	Power [W]	Material	Power [W]
NbTi	5.95×10^{-4}	NbTi	2.09×10^{-5}
CuNi	3.13×10^{-3}	CuNi	5.12×10^{-5}
Total	3.73×10^{-3}	Total	7.21×10^{-5}

Table 4.2 Results of thermal model accounting for the powder filter’s finite thermal conductance. The balance in power (3.65 mW) flows out through the powder filter. Note that the Kevlar suspensions are not included here. They are sunk directly to the central plate so their values will be the same as in Table 4.1.

The model results indicate that the presence of CuNi cladding makes a large contribution to the thermal loads on the various temperature stages, significantly limiting refrigerator hold time. In particular, cladding between the JFET stage and the powder filter causes the powder filter to get hot, so it does not serve as an effective 2.6 K heat sink. Cladding between the bolometer stage and the powder filter then conducts excess heat to the bolometer stage. Predictions are compared with measured performance in Section 4.4.5.

4.4.3 Filter design

At the central plate the tensioned leads pass through a lossy dielectric powder filter. The powder filter formulation we use is described by [126]. It consists of stainless

Heat flow from JFET stage (130 K) to powder filter (2.6 K)		Heat flow from powder filter (2.6 K) to bolometer stage (0.1 K)	
Material	Power [W]	Material	Power [W]
NbTi	6.43×10^{-4}	NbTi	2.78×10^{-7}
Kevlar	1.03×10^{-2}	Kevlar	6.48×10^{-7}
Total	1.09×10^{-2}	Total	9.26×10^{-7}

Table 4.3 Results of thermal model accounting for the powder filter’s finite thermal conductance and removing the CuNi cladding. In this case the powder filter does not heat above the central plate temperature.

Material Thermal Properties			
Material	Temp. range [K]	κ [$\text{W m}^{-1} \text{K}^{-1}$]	Ref.
NbTi	$T < 10.5$	$0.027 \left(\frac{T}{\text{K}}\right)^2$	[119]
NbTi	$T > 10.5$	$0.0407 \left(\frac{T}{\text{K}}\right)$	[120]
CuNi	$T < 240$	$0.072 \left(\frac{T}{\text{K}}\right) < \kappa < 0.21 \left(\frac{T}{\text{K}}\right)$	[121, 122]
Kevlar	$T < 2.6$	$0.0024 \left(\frac{T}{\text{K}}\right)^{2.1}$	[123]
Kevlar	$T > 2.6$	$0.0022 \left(\frac{T}{\text{K}}\right)^{1.58}$	[124]
Epoxy	$4 < T < 10$	$0.0017 \left(\frac{T}{\text{K}}\right) + 0.013 < \kappa < 0.023 \left(\frac{T}{\text{K}}\right)$	[125]

Table 4.4 Thermal properties of detector assembly materials.

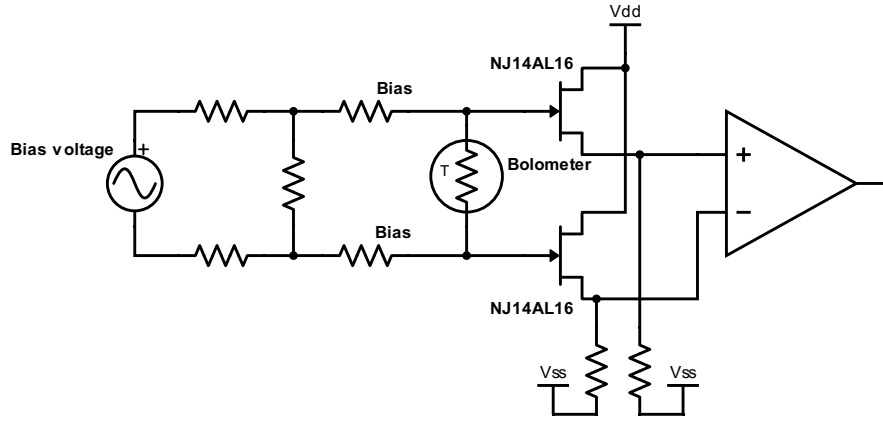


Figure 4.11 *PIXIE* differential readout schematic. The bolometer and bias resistors operate at 100 mK. The JFETs and voltage divider operate at 130 K. The bias voltage supply and differential amplifier operate at room temperature. Both JFETs are biased off the same V_{ss} and V_{dd} lines, so care must be taken in choosing JFETs with similar IV characteristics. As shown the bolometer is AC biased, but the bias electronics can operate in either AC or DC bias mode.

steel powder cast with super glue. The filter is cast directly around the CuNi-clad NbTi wires. Given the geometry of the filter and its composition, we calculate its transmission spectrum using results by [126] and [127]. We expect the filter to achieve > 100 dB attenuation at frequencies greater than 50 GHz. Multiplying the filter response by a Planck spectrum at 130 K, and integrating, the filter transmits < 0.01 fW.

4.4.4 Amplifier design

As shown in Figure 4.11, the front end amplifier features two JFETs per detector channel, enabling differential readout at the 130 K plate. The JFETs are in a source-follower configuration. The gain of a source follower is just less than 1 (for a derivation, see [128]). Its purpose is to act as a transimpedance buffer, converting the high source impedance of the bolometer ($M\Omega$ -scale) to the low output impedance of the JFETs ($k\Omega$ -scale). A room temperature voltage amplifier provides additional gain.

To minimize the number of wires going in and out of the cryostat, the JFETs share bias lines (see Figure 4.11). Thus care must be taken to use JFETs with similar IV characteristics. We were provided with 40 NJ14AL16 bare die JFETs by the x-ray microcalorimeter group at NASA/GSFC. They were probed at room temperature using a Keithley 4200-SCS Semiconductor Characterization System. The instrument was configured to measure the JFET drain current I_d as a function of the voltage between the gate and source V_{gs} and the voltage between the drain and source V_{ds} . Electrical contact to the JFET wirebond pads was made with tungsten needles coupled to micrometer-actuated x-y-z stages.

Of the 40 JFETs that were probed at room temperature, 16 had suitably-similar IV characteristics to be biased off the same lines. A typical suite of IV curves from a tested device is shown in Figure 4.12 and a scatter plot showing the spread in bias characteristics of the 40 JFETs is shown in Figure 4.13.

4.4.5 Preliminary tests

In preliminary tests, all components of the detector assembly worked. The assembly survived thermal cycling between room temperature and 2.6 K. Temperature stability of the JFET stage at ~ 130 K was achieved. All the JFETs were successfully operated at the same bias point. Unfortunately, the heat load on the coldest stage was too high to achieve 100 mK temperature stability. Instead, the stage could reach a base temperature of less than 100 mK, but its temperature would then rise at rates of ~ 10 mK per minute. As a result, the bolometer installed in the package could not be calibrated.

In order to characterize the heat flow to the bolometer plate, we measured the current in the ADR magnet versus time at a variety of JFET board temperatures, ranging from 35 K (lowest readout temperature of the Cernox thermometer) to 95 K. Assuming that the magnet current is proportional to the thermal energy in the

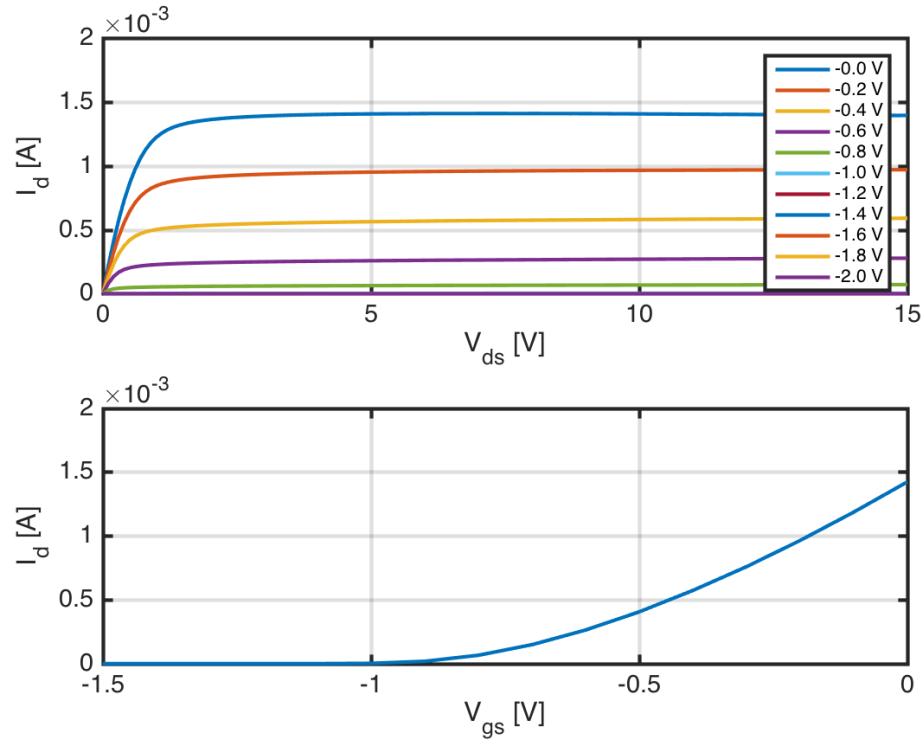


Figure 4.12 Suite of IV curves from a typical measured device. From these curves important device characteristics are extracted, including the pinch-off voltage V_{po} , the transconductance g_m , and the on-off voltage V_{on} . The legend in the upper plot gives V_{gs} corresponding to each curve. In the lower plot, V_{ds} was 5 V, so the device was operated in the saturation regime.

system, the slope of the current versus time curve is proportional to the heat flowing to the bolometer stage. After calculating the slopes, we fit a power law of the form $P = A \times T^n$ to the slope versus JFET temperature curve. If the heat flow P were radiative, we would expect a temperature exponent n of 4. If the flow were in normal metal leads, we would expect a temperature exponent n of 2. As shown in Figure 4.15, we find the latter is the case. This is most likely due to heat conduction down the CuNi cladding of the tensioned leads. We will repeat the experiment in the near future with the CuNi chemically stripped from the leads. Other factors could also be responsible for the high conduction, for example coefficient of thermal expansion (CTE) mismatches between the Cu plate, the powder filter, and the wires, which could result in vacuum interfaces between the components at low temperature. Initial

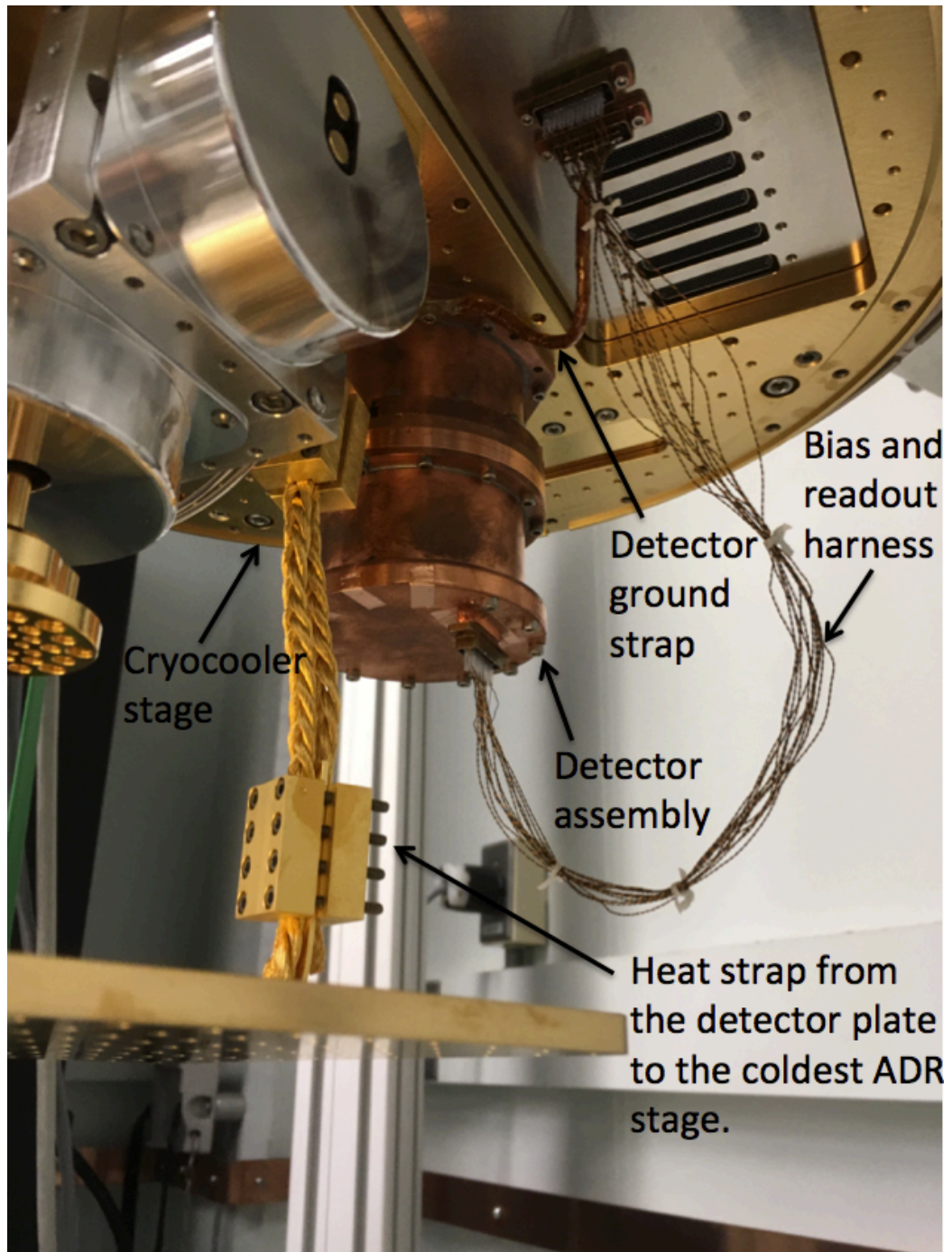


Figure 4.14 *PIXIE* sub-Kelvin experimental setup. The DA is bolted directly to the ~ 2.6 K cryocooler stage. A thermal strap couples the detector plate to the coldest ADR stage. It is comprised of gold plated and annealed 99.999% pure copper flags clamped to a pair of annealed and gold plated copper braids that provide strain relief. The ground strap ensures that the readout electronics and detector assembly share ground.

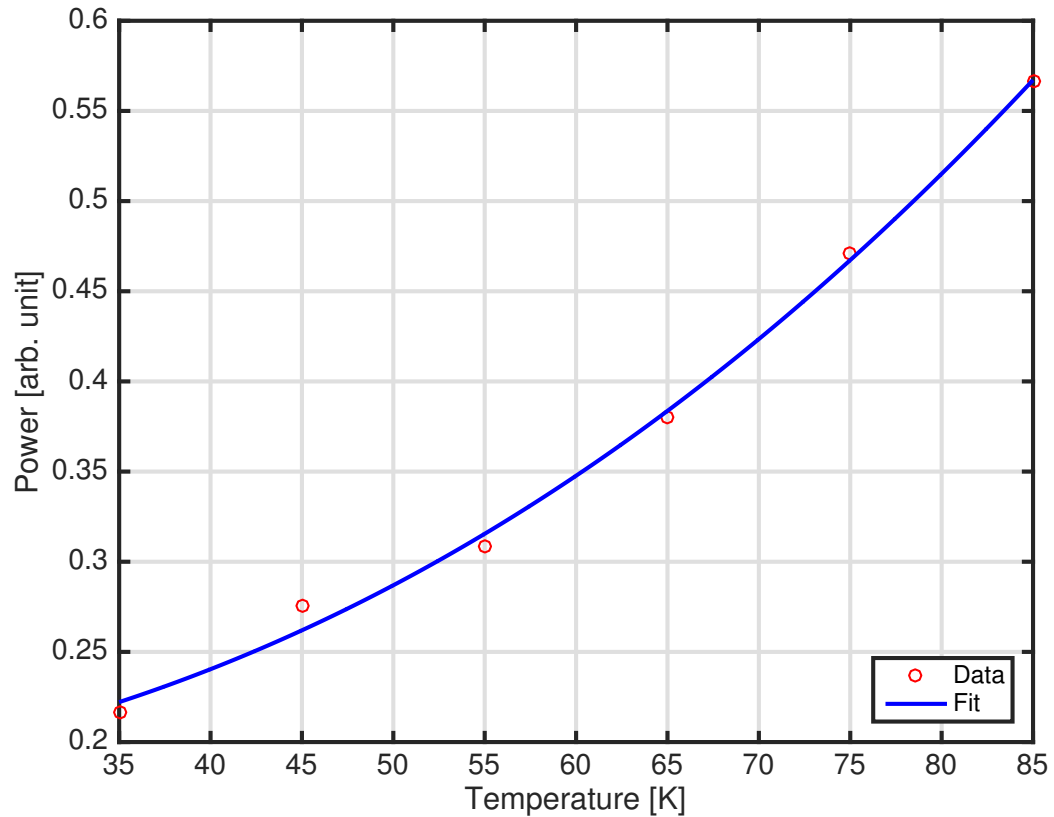


Figure 4.15 Power flowing to the bolometer plate as a function of JFET temperature. The power law fit to the data gives a best-fit exponent of 2.3, close to the expected exponent (2) for heat flowing in normal metal. Stripping the CuNi cladding should alleviate the temperature instability.

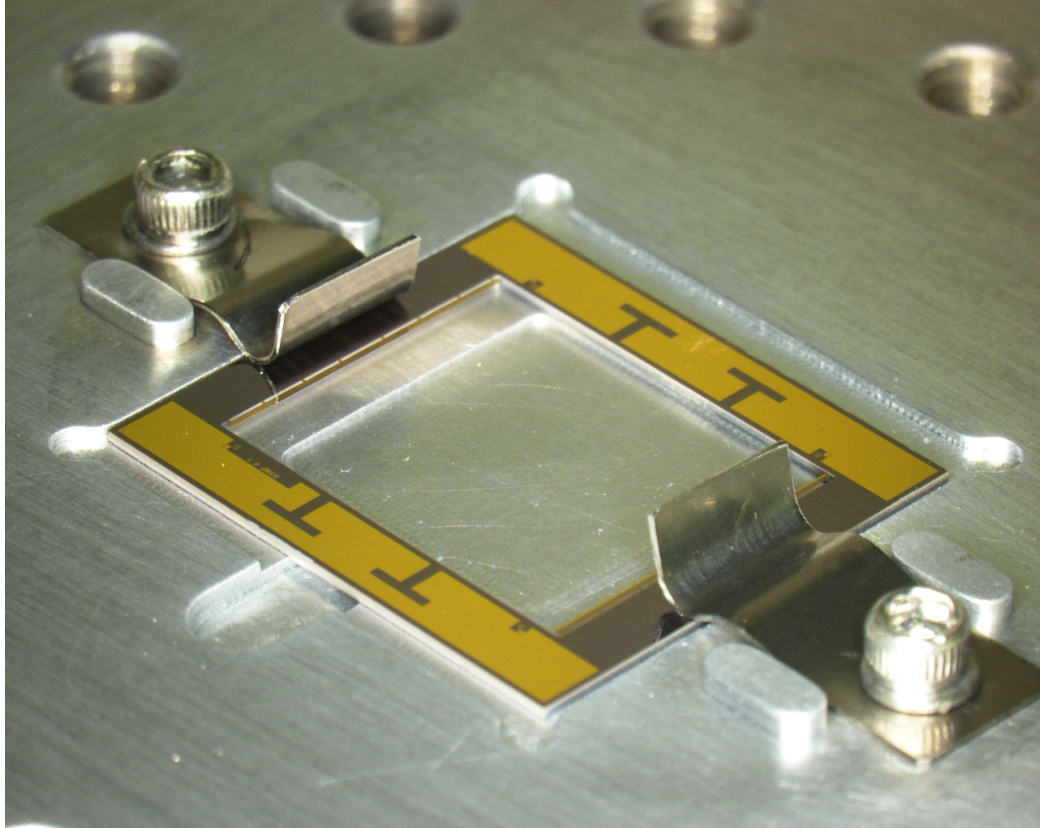


Figure 4.16 *PIXIE* detector packaged for vibration testing. The detector is mounted in a recessed cavity machined into a 6061 aluminum plate. The plate was designed to have vibrational modes at frequencies much higher than the vibration table is capable of generating. The detector is held in place with titanium spring clips. The clips were staked with Arathane (not shown) to prevent movement during the vibration test. Barely visible adjacent to the spring clips are the bolometer endbanks. The absorber structure is transparent.

GEVS-specified vibration levels are significantly harsher than the hardware would experience on a MIDEX rocket. GEVS is meant to encompass almost all launch vehicles. The vibration table only moves in one axial direction at a time. Shaking the hardware along three axes requires repeated single axis tests, reorienting the hardware between tests.

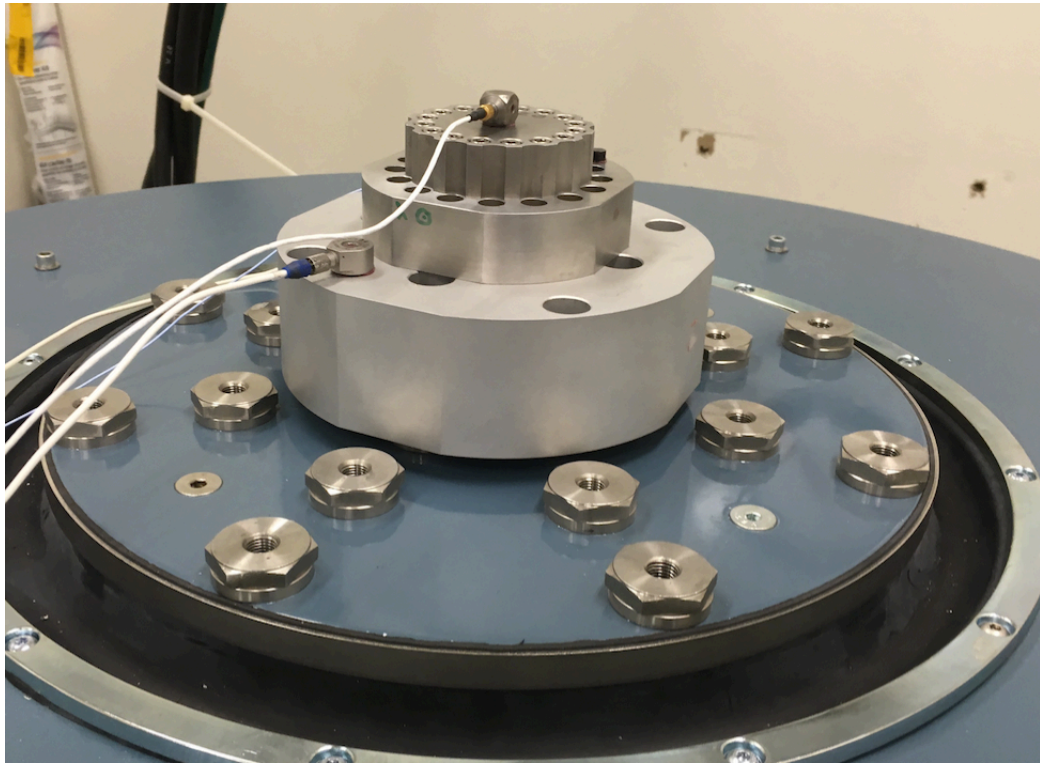


Figure 4.17 *PIXIE* vibration package mounted on the vibration table at NASA/GSFC. The pictured configuration is for vertical (\hat{z}) vibrations. Visible on the package are both control (on the vibration table interface plate) and measurement (on the bolometer lid) accelerometers.

4.5.1 Vibration package

Shown in Figures 4.16 and 4.17, we designed a package to mount the detector to the vibration table. The package consists of three parts machined from 6061 aluminum alloy: a vibration table interface plate, a bolometer mounting plate, and a lid. The vibration table interface plate matches the bolt pattern of the vibration table. The bottom of the plate is machined so that only bosses make contact with the vibration table. This prevents slipping at the table-adapter interface, mitigating the possibility of frequency upconversion of vibrational modes from the table to the plate. The bolometer mounting plate bolts to the vibration table interface plate. The underside of the plate is milled out, with the exception of the area immediate surrounding the bolts. Again this prevents slipping and potential upconversion of vibrational modes. On the top surface of the bolometer mounting plate is a recess to fit the bolometer outer frame and a 225 μm -deep backshort beneath the detector's absorber structure to simulate a flight-like package. The bolometer is held in place with a pair of spring clips made from 0.005"-thick titanium foil. Arathane staking prevents the spring clip screws from loosening during vibration testing. A lid mounts to the bolometer mounting plate. It has a cavity milled out of its bottom surface to accommodate the spring clips. The lid is not strictly necessary for the vibration testing, but rather it keeps the bolometer clean and free of debris during the tests.

Control and measurement accelerometers are mounted to the detector package with wax. The control accelerometer measures single axis acceleration. It provides closed-loop feedback control to the vibration table. It mounts to the vibration table interface plate. The measurement accelerometer is a three axis type (i.e., it measures acceleration along the \hat{x} , \hat{y} and \hat{z} directions). It mounts to the package lid and is meant to measure the vibration environment that the detector experiences.

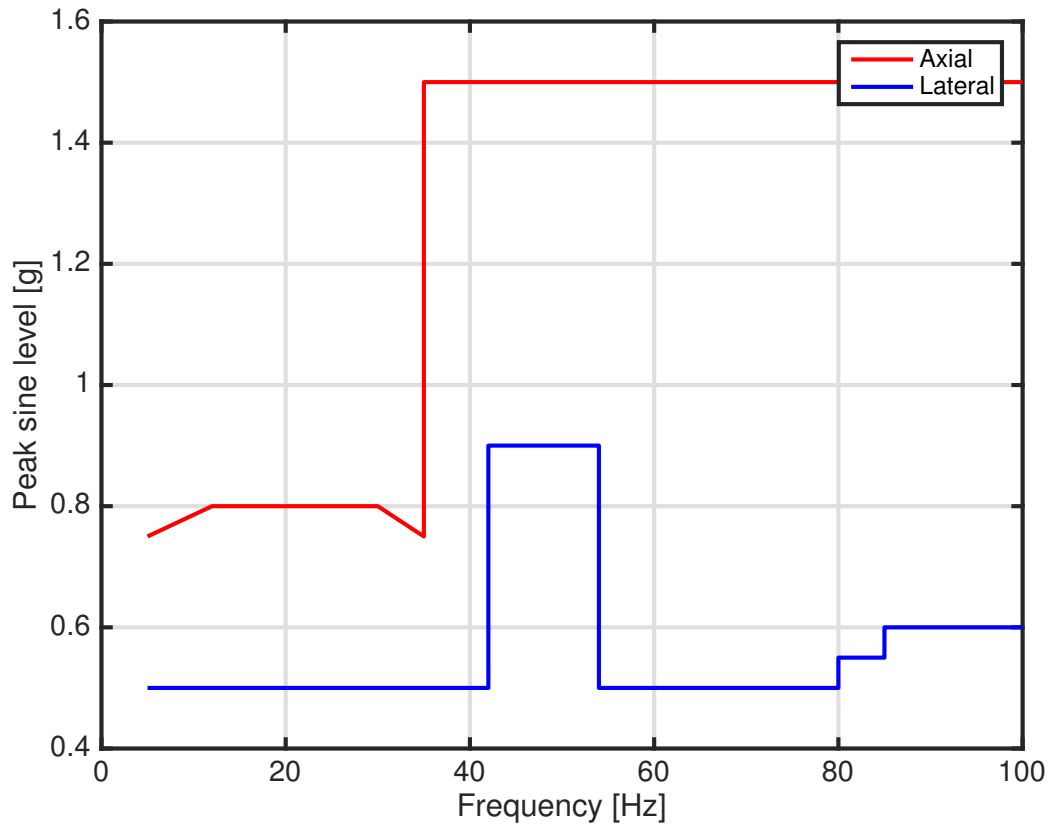


Figure 4.18 Axial and lateral vibration levels that MIDEX hardware must survive.

4.5.2 MIDEX-specified vibration test

Shown in Figure 4.18, the MIDEX manual [129] specifies swept sine vibration levels that MIDEX hardware must be able to withstand in axial and lateral directions, without explicitly stating the launch vehicle that will carry the payload. In the nominal *PIXIE* instrument design, the detector will be positioned vertically, where the lateral direction is normal to the absorber structure, and the axial direction is in plane with the absorber. The vibration test was performed as such, with the detector subjected to the axial-specified vibrations along both axes that form the absorber plane, and lateral-specified vibrations in the direction normal to the absorber. In this test, the control accelerometer and the measurement accelerometer agreed, indicating that the assembly acted linearly and the test was well defined.

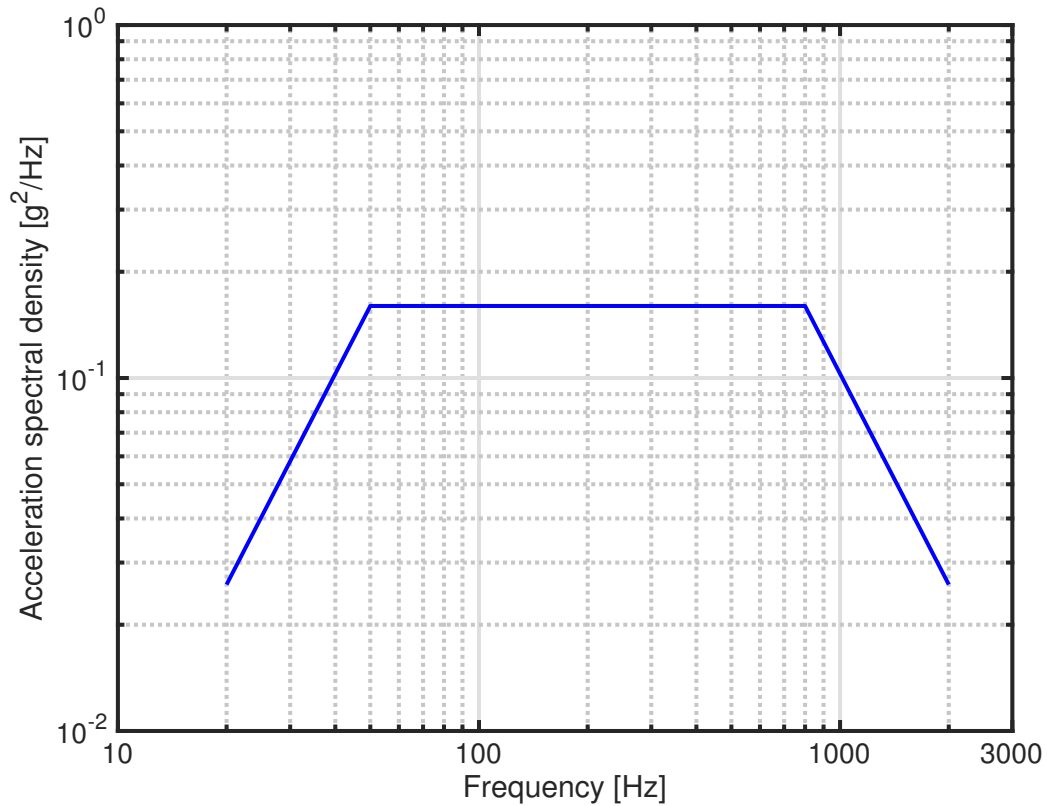


Figure 4.19 GEVS-specified vibration power spectral density. For our test, we notched several frequencies that were subharmonics of the acoustic resonant frequency of the air trapped in the package lid cavity, ensuring that the test is a vibrational and not acoustic. The integrated power in the above spectrum is $14.1 g_{rms}$.

4.5.3 GEVS-specified vibration test

Whereas the MIDEX manual specifies swept sine vibration levels at defined peak magnitudes, the GEVS manual specifies random vibrational power spectral density that hardware must withstand. This power spectrum is shown in Figure 4.19. For our particular case, we notched frequencies at subharmonics of the expected resonant frequency of the air trapped inside the package lid (~ 4.5 kHz). Without detailed characterization of the vibration table's non-linearities, the test could otherwise be ill-defined; we would expect a vibration test and instead get an acoustic test. We vibrated the detector at the GEVS-specified levels along all three axes.

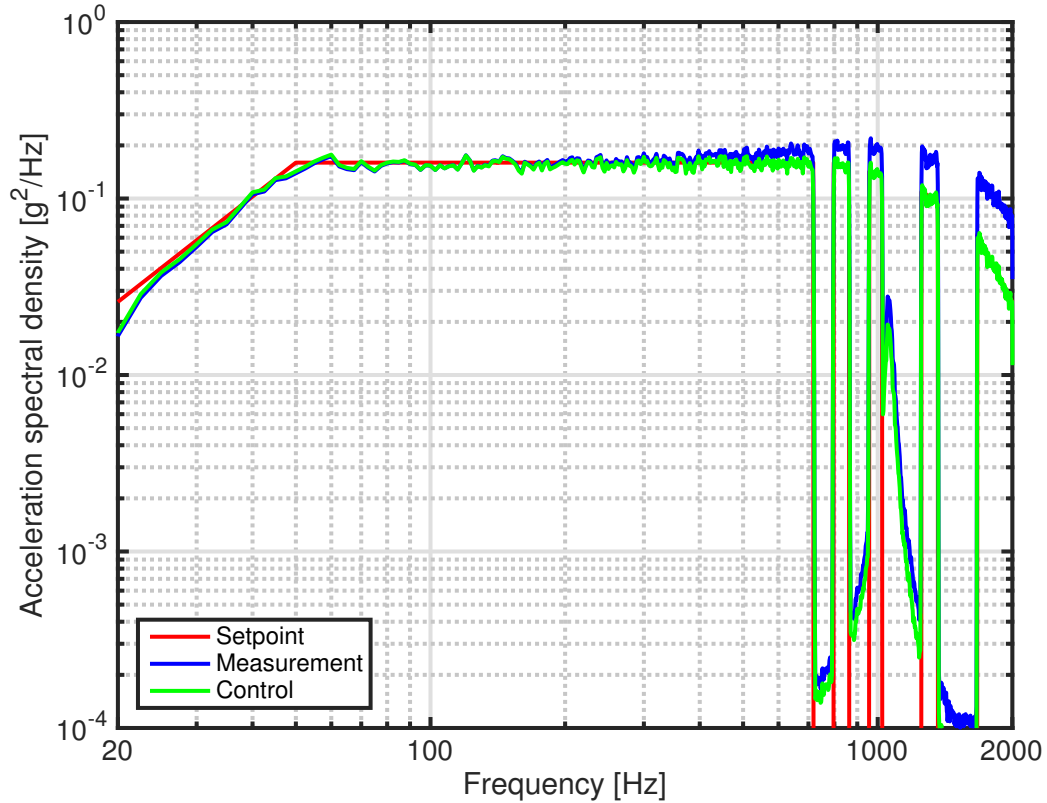


Figure 4.20 Results of GEVS random vibration test along the bolometer’s axis of absorption. The notches at high frequencies occur at subharmonics of the lid cavity’s resonant frequency. At low frequencies the measurement and control accelerometers follow the table’s setpoint, but at high frequencies there are some departures. The table appears to have a resonance at just over 1000 Hz, indicated by the spike in both the control and measurement data despite having notched that frequency. In addition, the measurement accelerometer deviates from the control accelerometer by roughly a factor of 2 at high frequencies, possibly indicating some non-linearity in the bolometer package.

4.5.4 Results

In the MIDEX test, the data from the measurement accelerometers agreed well with the target setpoints and the measurement accelerometers. This indicated that the experimental setup was linear in the frequency and acceleration regime during this test. During the GEVS test, some non-linearities were present, as indicated by discrepancies between the data measured by the measurement and control accelerometers, and acceleration setpoints of the table (see Figure 4.20).

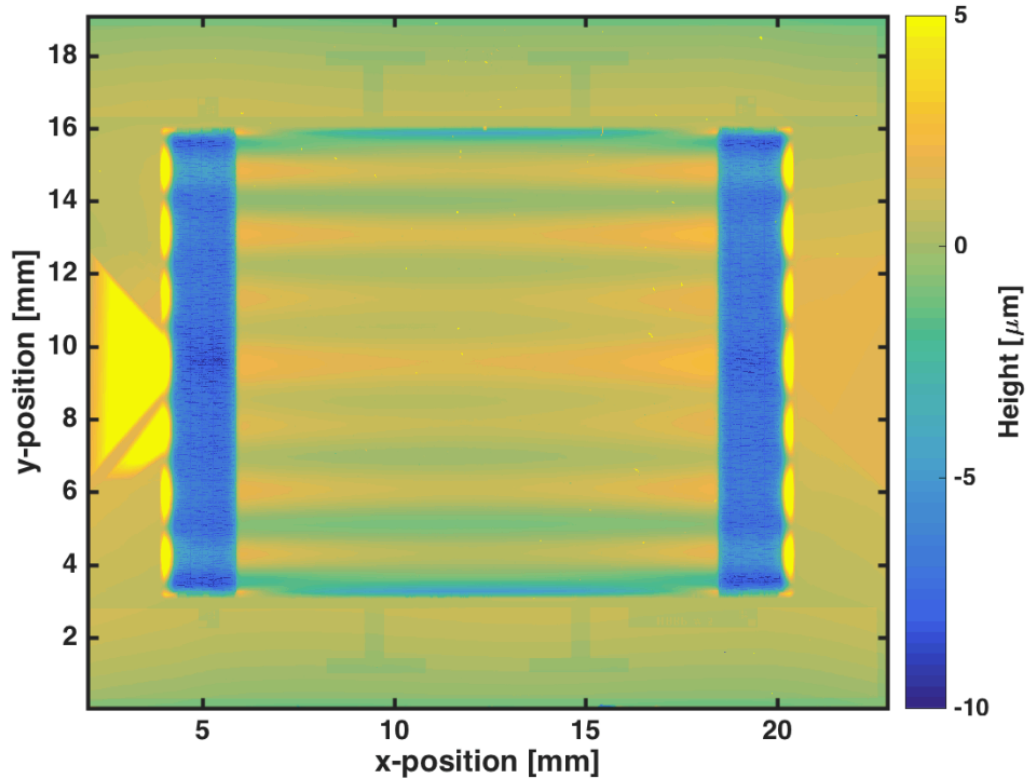


Figure 4.21 Interferometer measurement of the absorber after testing at GEVS levels. The only discernible difference between this measurement and a measurement taken before the vibration test is the increased number of particles, which show up as yellow specks. Upon inspection with a high magnification optical microscope, these particles appear to be shavings of metal that were likely formed by rubbing between the bolts securing the lid to the bolometer plate and the lid's through holes.

To assess any potential damage sustained by the detector during vibration testing, we performed microscope inspections of the absorber between each axial measurement, and white light interferometer measurements of the detector before testing, after MIDEEX testing, and after GEVS testing. The microscope inspections were at fairly low magnification, due to microscope availability and time constraints, but were enough to verify that the absorber structure was intact after each axial test.

As shown in Figure 4.21, the detector sustained no damage during vibration testing. The only difference between this measurement and a measurement before vibration testing is the presence of an increased number of small metallic particles, which likely came from rubbing between the lid and the bolts that secure it to the bolometer plate. These would have been easily redistributed during inspections of the chip. A detailed inspection of the absorber with a high magnification optical microscope confirmed that the detector sustained no damage during the vibration test. Based on these results, the detector is sufficiently robust to survive the vibration environment expected at launch.

4.6 Conclusion

We designed, fabricated, and characterized large area polarization-sensitive bolometers for the *PIXIE* experiment. Multimode bolometers designed for a FTS like *PIXIE* require a different optimization from bolometers developed for focal-plane imagers. In particular, they must handle a large, near-constant optical bias (~ 120 pW), but still operate with sensitivity near the thermodynamic limit across the relevant bandwidth. They also must have a large and mechanically robust absorbing area that is sensitive to all optical frequencies of interest, but relatively insensitive to particle hits.

Mechanical characterization of the fabricated *PIXIE* bolometers with scanning electron microscopy and white light interferometry shows that our tensioning scheme

successfully flattens the absorber strings, enabling indium bump hybridization of a pair of bolometer chips. The resonant frequencies of the tensioned absorbers are also expected to be well above the vibrational frequencies the detectors will experience at launch. We confirmed that the absorbers are robust in vibration environments significantly harsher than they will experience at launch. Next we will subject a hybridized pair of bolometers to environmental testing.

The dark data provide significant insight into the performance of the *PIXIE* bolometers, particularly regarding the thermal behavior of the endbanks. Our thermal model agrees well with the data, and the results indicate that the *PIXIE* bolometers satisfy the sensitivity and bandwidth requirements of the space mission (see Figure 4.9).

We designed and built a next-generation detector assembly for cryogenic characterization of the *PIXIE* bolometers. In the immediate future, we will employ it to further characterize the bolometers, specifically targeting the absorber structure. These measurements will include thermal transport measurements of absorbers in the dark, AC impedance measurements, and optical measurements with a cryogenic fiber optic source.

Chapter 5

Conclusion and Outlook

It has been over 20 years since a FTS flew to measure the CMB, and it is easy to overlook the important contributions that FTS measurements have made to CMB studies. It is also easy to forget that the FTS is a proven technology; cryogenic versions have performed reliably from balloon, sounding rocket, and satellite platforms. *PIXIE* has the potential to make enormous contributions to many areas of physics. A detection of the inflationary *B*-mode polarization signal of the CMB would establish inflation as a physical reality, probing physics at energies inaccessible by other means. Similarly, if *PIXIE* does not detect the *B*-mode signal, and instead sets an upper limit on the tensor-to-scalar ratio $r < 4 \times 10^{-4}$, the simplest inflationary models must be revisited. Measurements of distortions to the CMB Planck spectrum would provide critical information about the transfer of energy in the early universe. The superposition of *T*-, μ -, and *y*-type distortion signals will fill in critical details about the time dependence of the early universe's composition. Measurements of athermal spectral distortions from atomic transitions will provide additional information about the composition of the early universe and its energy environment. In addition, spectral distortion measurements open a window to observations of the universe's "dark ages."

PIXIE's foreground measurements will enable the primary science goals and remain an invaluable dataset for future far infrared and mm-wave experiments. It will map line emission sources across the sky with excellent spectral resolution and absolute frequency calibration. These maps can be used to calibrate future instruments that make measurements in the *PIXIE* band. Broadband measurements of the galactic synchrotron and thermal dust emission made by *PIXIE* will enable accurate fits to the synchrotron spectral index and the dust emission spectrum through its peak, giving us the best chance at effectively subtracting them and preventing corruption of CMB measurements.

PIXIE's highly symmetric design allows significant control of instrumental systematic effects. The amplitude and spectral content of systematic error signals can be determined analytically. The processes to correct systematic effects are in general simple. Emission errors are corrected by averaging. Geometric errors are contributions to the instrument's optical efficiency. They will not generate a polarized signal when the sky is unpolarized. Mirror transport mechanism errors are corrected by symmetrizing interferograms before taking the Fourier transform. Many MTM error solutions have already been tested on *FIRAS* data. Long-term instrumental drifts are not confused with polarization. Uncorrected, they can affect the first few bins of the Fourier transform. But averaging mitigates them as well.

We have made significant steps in developing multimode bolometers for *PIXIE* that will be suitable for the flight instrument. They are mechanically robust in the vibration environment they will experience at launch. We also need to confirm that they will survive the acoustic environment at launch. This will be confirmed in the near future. The dark data indicate that the bolometers have adequate sensitivity and bandwidth to meet the requirements of the space mission. Continued work in the immediate future will aim to measure the time constant(s) of the absorber structure, confirming that their performance is not limited under optical bias.

In December 2016, building and flying the *PIXIE* experiment was proposed in response to NASA's 2016 Medium Explorer (MIDEX) Announcement of Opportunity (AO). If the proposal is successful, the experiment will launch in 2022 or 2023.

Bibliography

- [1] A. A. Penzias and R. W. Wilson, “A Measurement of Excess Antenna Temperature at 4080 Mc/s.,” *ApJ*, vol. 142, pp. 419–421, July 1965.
- [2] J. C. Mather, “The Cosmic Background Explorer /COBE/,” *Optical Engineering*, vol. 21, pp. 769–774, Aug. 1982.
- [3] N. W. Boggess, J. C. Mather, R. Weiss, C. L. Bennett, E. S. Cheng, E. Dwek, S. Gulkis, M. G. Hauser, M. A. Janssen, T. Kelsall, S. S. Meyer, S. H. Moseley, T. L. Murdock, R. A. Shafer, R. F. Silverberg, G. F. Smoot, D. T. Wilkinson, and E. L. Wright, “The COBE mission - Its design and performance two years after launch,” *ApJ*, vol. 397, pp. 420–429, Oct. 1992.
- [4] J. C. Mather, E. S. Cheng, D. A. Cottingham, R. E. Eplee, Jr., D. J. Fixsen, T. Hewagama, R. B. Isaacman, K. A. Jensen, S. S. Meyer, P. D. Noerdlinger, S. M. Read, L. P. Rosen, R. A. Shafer, E. L. Wright, C. L. Bennett, N. W. Boggess, M. G. Hauser, T. Kelsall, S. H. Moseley, Jr., R. F. Silverberg, G. F. Smoot, R. Weiss, and D. T. Wilkinson, “Measurement of the cosmic microwave background spectrum by the COBE FIRAS instrument,” *ApJ*, vol. 420, pp. 439–444, Jan. 1994.
- [5] D. J. Fixsen, E. S. Cheng, J. M. Gales, J. C. Mather, R. A. Shafer, and E. L. Wright, “The Cosmic Microwave Background Spectrum from the Full COBE FIRAS Data Set,” *ApJ*, vol. 473, p. 576, Dec. 1996.

- [6] H. P. Gush, M. Halpern, and E. H. Wishnow, “Rocket measurement of the cosmic-background-radiation mm-wave spectrum,” *Physical Review Letters*, vol. 65, pp. 537–540, July 1990.
- [7] H. P. Gush, E. H. Wishnow, and M. Halpern, “Rocket measurement of the submillimeter cosmic background spectrum.,” Society of Photo-Optical Instrumentation Engineers, 1993.
- [8] R. A. Alpher, H. Bethe, and G. Gamow, “The Origin of Chemical Elements,” *Physical Review*, vol. 73, pp. 803–804, Apr. 1948.
- [9] R. K. Sachs and A. M. Wolfe, “Perturbations of a Cosmological Model and Angular Variations of the Microwave Background,” *ApJ*, vol. 147, p. 73, Jan. 1967.
- [10] J. Silk, “Cosmic Black-Body Radiation and Galaxy Formation,” *ApJ*, vol. 151, p. 459, Feb. 1968.
- [11] R. A. Sunyaev and Y. B. Zeldovich, “Small-Scale Fluctuations of Relic Radiation,” *Astrophysics and Space Science*, vol. 7, pp. 3–19, Apr. 1970.
- [12] P. J. E. Peebles and J. T. Yu, “Primeval Adiabatic Perturbation in an Expanding Universe,” *ApJ*, vol. 162, p. 815, Dec. 1970.
- [13] C. L. Bennett, M. Bay, M. Halpern, G. Hinshaw, C. Jackson, N. Jarosik, A. Kogut, M. Limon, S. S. Meyer, L. Page, D. N. Spergel, G. S. Tucker, D. T. Wilkinson, E. Wollack, and E. L. Wright, “The Microwave Anisotropy Probe Mission,” *ApJ*, vol. 583, pp. 1–23, Jan. 2003.
- [14] Planck Collaboration, P. A. R. Ade, N. Aghanim, M. Arnaud, M. Ashdown, J. Aumont, C. Baccigalupi, M. Baker, A. Balbi, A. J. Banday, and et al.,

- “Planck early results. I. The Planck mission,” *Astron. & Astrophys.*, vol. 536, p. A1, Dec. 2011.
- [15] P. de Bernardis, E. Aquilini, A. Boscaleri, M. de Petris, M. Gervasi, L. Martinis, S. Masi, V. Natale, P. Palumbo, E. Scaramuzzi, and L. Valenziano, “ARGO: a balloon-borne telescope for measurements of the millimeter diffuse sky emission,” *Astron. & Astrophys.*, vol. 271, p. 683, Apr. 1993.
- [16] G. S. Tucker, H. P. Gush, M. Halpern, I. Shinkoda, and W. Towlson, “Anisotropy in the Microwave Sky: Results from the First Flight of the Balloon-borne Anisotropy Measurement (BAM),” *ApJ*, vol. 475, pp. L73–L76, Feb. 1997.
- [17] P. D. Mauskopf, P. A. R. Ade, P. de Bernardis, J. J. Bock, J. Borrill, A. Boscaleri, B. P. Crill, G. DeGasperis, G. De Troia, P. Farese, P. G. Ferreira, K. Ganga, M. Giacometti, S. Hanany, V. V. Hristov, A. Iacoangeli, A. H. Jaffe, A. E. Lange, A. T. Lee, S. Masi, A. Melchiorri, F. Melchiorri, L. Miglio, T. Montroy, C. B. Netterfield, E. Pascale, F. Piacentini, P. L. Richards, G. Romeo, J. E. Ruhl, E. Scannapieco, F. Scaramuzzi, R. Stompor, and N. Vittorio, “Measurement of a Peak in the Cosmic Microwave Background Power Spectrum from the North American Test Flight of Boomerang,” *ApJ*, vol. 536, pp. L59–L62, June 2000.
- [18] K. Ganga, L. Page, E. Cheng, and S. Meyer, “The amplitude and spectral index of the large angular scale anisotropy in the cosmic microwave background radiation,” *ApJ*, vol. 432, pp. L15–L18, Sept. 1994.
- [19] A. de Oliveira-Costa, M. J. Devlin, T. Herbig, A. D. Miller, C. B. Netterfield, L. A. Page, and M. Tegmark, “Mapping the Cosmic Microwave Background Anisotropy: Combined Analysis of QMAP Flights,” *ApJ*, vol. 509, pp. L77–L80, Dec. 1998.

- [20] S. Tanaka, D. Alsop, E. Cheng, A. Clapp, D. Cottingham, M. Devlin, M. Fischer, J. Gundersen, C. Hagmann, W. Holmes, V. Hristov, T. Koch, E. Kreysa, A. Lange, M. Lim, P. Lubin, P. Mauskopf, P. Meinhold, P. Richards, G. Smoot, and P. Timbie, “The Millimeter Wave Anisotropy Experiment (MAX),” *Astrophysical Letters and Communications*, vol. 32, p. 223, 1995.
- [21] S. Hanany, P. Ade, A. Balbi, J. Bock, J. Borrill, A. Boscaleri, P. de Bernardis, P. G. Ferreira, V. V. Hristov, A. H. Jaffe, A. E. Lange, A. T. Lee, P. D. Mauskopf, C. B. Netterfield, S. Oh, E. Pascale, B. Rabii, P. L. Richards, G. F. Smoot, R. Stompor, C. D. Winant, and J. H. P. Wu, “MAXIMA-1: A Measurement of the Cosmic Microwave Background Anisotropy on Angular Scales of 10^{-5° ,” *ApJ*, vol. 545, pp. L5–L9, Dec. 2000.
- [22] M. S. Kowitt, E. S. Cheng, D. A. Cottingham, K. Farooqui, D. J. Fixsen, K. Ganga, C. A. Inman, S. S. Meyer, L. A. Page, L. Piccirillo, J. L. Puchalla, J. Ruhl, R. K. Schaefer, R. F. Silverberg, P. T. Timbie, G. Wilson, and J. W. Zhou, “The MSAM/TopHat Program of Anisotropy Measurements,” *Astrophysical Letters and Communications*, vol. 32, p. 273, 1995.
- [23] A. A. Fraisse, P. A. R. Ade, M. Amiri, S. J. Benton, J. J. Bock, J. R. Bond, J. A. Bonetti, S. Bryan, B. Burger, H. C. Chiang, C. N. Clark, C. R. Contaldi, B. P. Crill, G. Davis, O. Doré, M. Farhang, J. P. Filippini, L. M. Fissel, N. N. Gandilo, S. Golwala, J. E. Gudmundsson, M. Hasselfield, G. Hilton, W. Holmes, V. V. Hristov, K. Irwin, W. C. Jones, C. L. Kuo, C. J. MacTavish, P. V. Mason, T. E. Montroy, T. A. Morford, C. B. Netterfield, D. T. O’Dea, A. S. Rahlin, C. Reintsema, J. E. Ruhl, M. C. Runyan, M. A. Schenker, J. A. Shariff, J. D. Soler, A. Trangsrud, C. Tucker, R. S. Tucker, A. D. Turner, and D. Wiebe, “SPIDER: probing the early Universe with a suborbital polarimeter,” *Journal of Cosmology and Astroparticle Physics*, vol. 4, p. 047, Apr. 2013.

- [24] R. Subrahmanyan, M. J. Kesteven, R. D. Ekers, M. Sinclair, and J. Silk, “An Australia Telescope survey for CMB anisotropies,” *Mon. Not. R. Astron. Soc.*, vol. 315, pp. 808–822, July 2000.
- [25] K. S. Dawson, W. L. Holzapfel, J. E. Carlstrom, M. Joy, S. J. LaRoque, and E. D. Reese, “A Preliminary Detection of Arcminute-Scale Cosmic Microwave Background Anisotropy with the BIMA Array,” *ApJ*, vol. 553, pp. L1–L4, May 2001.
- [26] J. C. Baker, K. Grainge, M. P. Hobson, M. E. Jones, R. Kneissl, A. N. Lasenby, C. M. M. O’Sullivan, G. Pooley, G. Rocha, R. Saunders, P. F. Scott, and E. M. Waldram, “Detection of cosmic microwave background structure in a second field with the Cosmic Anisotropy Telescope,” *Mon. Not. R. Astron. Soc.*, vol. 308, pp. 1173–1178, Oct. 1999.
- [27] B. S. Mason, T. J. Pearson, A. C. S. Readhead, M. Shepherd, J. Sievers, P. Udomprasert, J. K. Cartwright, and S. Padin, “First results from the CBI,” in *20th Texas Symposium on relativistic astrophysics* (J. C. Wheeler and H. Martel, eds.), vol. 586 of *American Institute of Physics Conference Series*, pp. 178–183, Oct. 2001.
- [28] N. W. Halverson, E. M. Leitch, C. Pryke, J. Kovac, J. E. Carlstrom, W. L. Holzapfel, M. Dragovan, J. K. Cartwright, B. S. Mason, S. Padin, T. J. Pearson, A. C. S. Readhead, and M. C. Shepherd, “Degree Angular Scale Interferometer First Results: A Measurement of the Cosmic Microwave Background Angular Power Spectrum,” *ApJ*, vol. 568, pp. 38–45, Mar. 2002.
- [29] S. R. Dicker, S. J. Melhuish, R. D. Davies, C. M. Gutiérrez, R. Rebolo, D. L. Harrison, R. J. Davis, A. Wilkinson, R. J. Hoyland, and R. A. Watson, “Cosmic

- microwave background observations with the Jodrell Bank-IAC interferometer at 33GHz,” *Mon. Not. R. Astron. Soc.*, vol. 309, pp. 750–760, Nov. 1999.
- [30] B. Femenía, R. Rebolo, C. M. Gutiérrez, M. Limon, and L. Piccirillo, “The Instituto de Astrofísica de Canarias-Bartol Cosmic Microwave Background Anisotropy Experiment: Results of the 1994 Campaign,” *ApJ*, vol. 498, pp. 117–136, May 1998.
- [31] E. Torbet, M. J. Devlin, W. B. Dorwart, T. Herbig, A. D. Miller, M. R. Nolta, L. Page, J. Puchalla, and H. T. Tran, “A Measurement of the Angular Power Spectrum of the Microwave Background Made from the High Chilean Andes,” *ApJ*, vol. 521, pp. L79–L82, Aug. 1999.
- [32] E. M. Leitch, A. C. S. Readhead, T. J. Pearson, S. T. Myers, S. Gulkis, and C. R. Lawrence, “A Measurement of Anisotropy in the Cosmic Microwave Background on 7′-22′ Scales,” *ApJ*, vol. 532, pp. 37–56, Mar. 2000.
- [33] S. R. Platt, J. Kovac, M. Dragovan, J. B. Peterson, and J. E. Ruhl, “Anisotropy in the Microwave Sky at 90 GHz: Results from Python III,” *ApJ*, vol. 475, pp. L1–L4, Jan. 1997.
- [34] C. B. Netterfield, M. J. Devlin, N. Jarosik, L. Page, and E. J. Wollack, “A Measurement of the Angular Power Spectrum of the Anisotropy in the Cosmic Microwave Background,” *ApJ*, vol. 474, pp. 47–66, Jan. 1997.
- [35] S. E. Church, K. M. Ganga, P. A. R. Ade, W. L. Holzapfel, P. D. Mauskopf, T. M. Wilbanks, and A. E. Lange, “An Upper Limit to Arcminute-Scale Anisotropy in the Cosmic Microwave Background Radiation at 142 GHz,” *ApJ*, vol. 484, pp. 523–537, July 1997.
- [36] C. M. Gutiérrez, R. Rebolo, R. A. Watson, R. D. Davies, A. W. Jones, and A. N.

- Lasenby, “The Tenerife Cosmic Microwave Background Maps: Observations and First Analysis,” *ApJ*, vol. 529, pp. 47–55, Jan. 2000.
- [37] A. D. Miller, R. Caldwell, M. J. Devlin, W. B. Dorwart, T. Herbig, M. R. Nolte, L. A. Page, J. Puchalla, E. Torbet, and H. T. Tran, “A Measurement of the Angular Power Spectrum of the Cosmic Microwave Background from $L = 100$ to 400,” *ApJ*, vol. 524, pp. L1–L4, Oct. 1999.
- [38] J. B. Peterson, G. S. Griffin, M. G. Newcomb, D. L. Alvarez, C. M. Cantalupo, D. Morgan, K. W. Miller, K. Ganga, D. Pernic, and M. Thoma, “First Results from Viper: Detection of Small-scale Anisotropy at 40 GHz,” *ApJ*, vol. 532, pp. L83–L86, Apr. 2000.
- [39] R. B. Partridge, E. A. Richards, E. B. Fomalont, K. I. Kellerman, and R. A. Windhorst, “Small-Scale Cosmic Microwave Background Observations at 8.4 GHz,” *ApJ*, vol. 483, pp. 38–50, July 1997.
- [40] G. S. Tucker, G. S. Griffin, H. T. Nguyen, and J. B. Peterson, “A Search for Small-Scale Anisotropy in the Cosmic Microwave Background,” *ApJ*, vol. 419, p. L45, Dec. 1993.
- [41] C. L. Reichardt, P. A. R. Ade, J. J. Bock, J. R. Bond, J. A. Brevik, C. R. Contaldi, M. D. Daub, J. T. Dempsey, J. H. Goldstein, W. L. Holzapfel, C. L. Kuo, A. E. Lange, M. Lueker, M. Newcomb, J. B. Peterson, J. Ruhl, M. C. Runyan, and Z. Staniszewski, “High-Resolution CMB Power Spectrum from the Complete ACBAR Data Set,” *ApJ*, vol. 694, pp. 1200–1219, Apr. 2009.
- [42] H. C. Chiang, P. A. R. Ade, D. Barkats, J. O. Battle, E. M. Bierman, J. J. Bock, C. D. Dowell, L. Duband, E. F. Hivon, W. L. Holzapfel, V. V. Hristov, W. C. Jones, B. G. Keating, J. M. Kovac, C. L. Kuo, A. E. Lange, E. M. Leitch, P. V. Mason, T. Matsumura, H. T. Nguyen, N. Ponthieu, C. Pryke,

- S. Richter, G. Rocha, C. Sheehy, Y. D. Takahashi, J. E. Tolan, and K. W. Yoon, “Measurement of Cosmic Microwave Background Polarization Power Spectra from Two Years of BICEP Data,” *ApJ*, vol. 711, pp. 1123–1140, Mar. 2010.
- [43] Z. Hou, C. L. Reichardt, K. T. Story, B. Follin, R. Keisler, K. A. Aird, B. A. Benson, L. E. Bleem, J. E. Carlstrom, C. L. Chang, H.-M. Cho, T. M. Crawford, A. T. Crites, T. de Haan, R. de Putter, M. A. Dobbs, S. Dodelson, J. Dudley, E. M. George, N. W. Halverson, G. P. Holder, W. L. Holzapfel, S. Hoover, J. D. Hrubes, M. Joy, L. Knox, A. T. Lee, E. M. Leitch, M. Lueker, D. Luong-Van, J. J. McMahon, J. Mehl, S. S. Meyer, M. Millea, J. J. Mohr, T. E. Montroy, S. Padin, T. Plagge, C. Pryke, J. E. Ruhl, J. T. Sayre, K. K. Schaffer, L. Shaw, E. Shirokoff, H. G. Spieler, Z. Staniszewski, A. A. Stark, A. van Engelen, K. Vanderlinde, J. D. Vieira, R. Williamson, and O. Zahn, “Constraints on Cosmology from the Cosmic Microwave Background Power Spectrum of the 2500 deg² SPT-SZ Survey,” *ApJ*, vol. 782, p. 74, Feb. 2014.
- [44] J. W. Fowler, V. Acquaviva, P. A. R. Ade, P. Aguirre, M. Amiri, J. W. Appel, L. F. Barrientos, E. S. Battistelli, J. R. Bond, B. Brown, B. Burger, J. Chervenak, S. Das, M. J. Devlin, S. R. Dicker, W. B. Doriese, J. Dunkley, R. Dünner, T. Essinger-Hileman, R. P. Fisher, A. Hajian, M. Halpern, M. Hasselfield, C. Hernández-Monteagudo, G. C. Hilton, M. Hilton, A. D. Hincks, R. Hlozek, K. M. Huffenberger, D. H. Hughes, J. P. Hughes, L. Infante, K. D. Irwin, R. Jimenez, J. B. Juin, M. Kaul, J. Klein, A. Kosowsky, J. M. Lau, M. Limon, Y.-T. Lin, R. H. Lupton, T. A. Marriage, D. Marsden, K. Martocci, P. Mauskopf, F. Menanteau, K. Moodley, H. Moseley, C. B. Netterfield, M. D. Niemack, M. R. Nolta, L. A. Page, L. Parker, B. Partridge, H. Quintana, B. Reid, N. Sehgal, J. Sievers, D. N. Spergel, S. T. Staggs, D. S. Swetz, E. R. Switzer, R. Thornton, H. Trac, C. Tucker, L. Verde, R. Warne, G. Wilson,

- E. Wollack, and Y. Zhao, “The Atacama Cosmology Telescope: A Measurement of the $600 < \ell < 8000$ Cosmic Microwave Background Power Spectrum at 148 GHz,” *ApJ*, vol. 722, pp. 1148–1161, Oct. 2010.
- [45] S. Dodelson, *Modern cosmology*. 2003.
- [46] M. Kamionkowski, A. Kosowsky, and A. Stebbins, “A Probe of Primordial Gravity Waves and Vorticity,” *Physical Review Letters*, vol. 78, pp. 2058–2061, Mar. 1997.
- [47] U. Seljak and M. Zaldarriaga, “Signature of Gravity Waves in the Polarization of the Microwave Background,” *Physical Review Letters*, vol. 78, pp. 2054–2057, Mar. 1997.
- [48] J. Chluba and R. A. Sunyaev, “The evolution of CMB spectral distortions in the early Universe,” *Mon. Not. R. Astron. Soc.*, vol. 419, pp. 1294–1314, Jan. 2012.
- [49] J. Chluba, E. Dimastrogiovanni, M. A. Amin, and M. Kamionkowski, “Evolution of CMB spectral distortion anisotropies and tests of primordial non-Gaussianity,” *ArXiv e-prints*, Oct. 2016.
- [50] D. J. Fixsen, “The Temperature of the Cosmic Microwave Background,” *ApJ*, vol. 707, pp. 916–920, Dec. 2009.
- [51] Planck Collaboration, R. Adam, P. A. R. Ade, N. Aghanim, Y. Akrami, M. I. R. Alves, F. Argüeso, M. Arnaud, F. Arroja, M. Ashdown, and et al., “Planck 2015 results. I. Overview of products and scientific results,” *Astron. & Astrophys.*, vol. 594, p. A1, Sept. 2016.
- [52] A. Kogut, D. J. Fixsen, D. T. Chuss, J. Dotson, E. Dwek, M. Halpern, G. F. Hinshaw, S. M. Meyer, S. H. Moseley, M. D. Seiffert, D. N. Spergel, and E. J.

- Wollack, “The Primordial Inflation Explorer (PIXIE): a nulling polarimeter for cosmic microwave background observations,” *Journal of Cosmology and Astroparticle Physics*, vol. 7, p. 25, July 2011.
- [53] A. Kogut, D. T. Chuss, J. Dotson, E. Dwek, D. J. Fixsen, M. Halpern, G. F. Hinshaw, S. Meyer, S. H. Moseley, M. D. Seiffert, D. N. Spergel, and E. J. Wollack, “The Primordial Inflation Explorer (PIXIE),” in *Society of Photo-Optical Instrumentation Engineers (SPIE) Conference Series*, vol. 9143 of *Society of Photo-Optical Instrumentation Engineers (SPIE) Conference Series*, p. 1, Aug. 2014.
- [54] A. Kogut, J. Chluba, D. J. Fixsen, S. Meyer, and D. Spergel, “The Primordial Inflation Explorer (PIXIE),” in *Society of Photo-Optical Instrumentation Engineers (SPIE) Conference Series*, vol. 9904 of *Proc. SPIE*, p. 99040W, July 2016.
- [55] D. P. Woody and P. L. Richards, “Near-millimeter spectrum of the microwave background,” *ApJ*, vol. 248, pp. 18–37, Aug. 1981.
- [56] P. André, C. Baccigalupi, A. Banday, D. Barbosa, B. Barreiro, J. Bartlett, N. Bartolo, E. Battistelli, R. Battye, G. Bendo, A. Benoît, J.-P. Bernard, M. Bersanelli, M. Béthermin, P. Bielewicz, A. Bonaldi, F. Bouchet, F. Boulanger, J. Brand, M. Bucher, C. Burigana, Z.-Y. Cai, P. Camus, F. Casas, V. Casasola, G. Castex, A. Challinor, J. Chluba, G. Chon, S. Colafrancesco, B. Comis, F. Cuttaia, G. D’Alessandro, A. Da Silva, R. Davis, M. de Avillez, P. de Bernardis, M. de Petris, A. de Rosa, G. de Zotti, J. Delabrouille, F.-X. Désert, C. Dickinson, J. M. Diego, J. Dunkley, T. Enßlin, J. Errard, E. Falgarone, P. Ferreira, K. Ferrière, F. Finelli, A. Fletcher, P. Fosalba, G. Fuller, S. Galli, K. Ganga, J. García-Bellido, A. Ghribi, M. Giard, Y. Giraud-Héraud, J. Gonzalez-Nuevo, K. Grainge, A. Gruppuso, A. Hall, J.-C. Hamilton,

M. Haverkorn, C. Hernandez-Monteagudo, D. Herranz, M. Jackson, A. Jaffe, R. Khatri, M. Kunz, L. Lamagna, M. Lattanzi, P. Leahy, J. Lesgourgues, M. Liguori, E. Liuzzo, M. Lopez-Caniego, J. Macias-Perez, B. Maffei, D. Maino, A. Mangilli, E. Martinez-Gonzalez, C. J. A. P. Martins, S. Masi, M. Massardi, S. Matarrese, A. Melchiorri, J.-B. Melin, A. Mennella, A. Mignano, M.-A. Miville-Deschênes, A. Monfardini, A. Murphy, P. Naselsky, F. Nati, P. Natoli, M. Negrello, F. Noviello, C. O’Sullivan, F. Paci, L. Pagano, R. Paladino, N. Palanque-Delabrouille, D. Paoletti, H. Peiris, F. Perrotta, F. Piacentini, M. Piat, L. Piccirillo, G. Pisano, G. Polenta, A. Pollo, N. Ponthieu, M. Remazeilles, S. Ricciardi, M. Roman, C. Rosset, J.-A. Rubino-Martin, M. Salatino, A. Schillaci, P. Shellard, J. Silk, A. Starobinsky, R. Stompor, R. Sunyaev, A. Tartari, L. Terenzi, L. Toffolatti, M. Tomasi, N. Trappe, M. Tristram, T. Trombetti, M. Tucci, R. Van de Weijgaert, B. Van Tent, L. Verde, P. Vielva, B. Wandelt, R. Watson, and S. Withington, “PRISM (Polarized Radiation Imaging and Spectroscopy Mission): an extended white paper,” *Journal of Cosmology and Astroparticle Physics*, vol. 2, p. 6, Feb. 2014.

- [57] BICEP2/Keck and Planck Collaborations, P. A. R. Ade, N. Aghanim, Z. Ahmed, R. W. Aikin, K. D. Alexander, M. Arnaud, J. Aumont, C. Bacigalupi, A. J. Banday, and et al., “Joint Analysis of BICEP2/Keck Array and Planck Data,” *Physical Review Letters*, vol. 114, p. 101301, Mar. 2015.
- [58] M. Remazeilles, C. Dickinson, H. K. K. Eriksen, and I. K. Wehus, “Sensitivity and foreground modelling for large-scale cosmic microwave background B-mode polarization satellite missions,” *Mon. Not. R. Astron. Soc.*, vol. 458, pp. 2032–2050, May 2016.
- [59] P. C. Nagler, K. T. Crowley, K. L. Denis, A. M. Devasia, D. J. Fixsen, A. J.

- Kogut, G. Manos, S. Porter, and T. R. Stevenson, “Multimode bolometer development for the PIXIE instrument,” *ArXiv e-prints*, Nov. 2016.
- [60] D. J. Fixsen, D. T. Chuss, A. Kogut, P. Mirel, and E. J. Wollack, “The calibration of PIXIE,” in *Society of Photo-Optical Instrumentation Engineers (SPIE) Conference Series*, vol. 9914 of *Proc. SPIE*, p. 991439, July 2016.
- [61] A. Kogut, D. J. Fixsen, and R. S. Hill, “Polarization properties of a broadband multi-moded concentrator,” *Journal of the Optical Society of America A*, vol. 32, p. 1040, June 2015.
- [62] P. J. Shirron, M. O. Kimball, D. J. Fixsen, A. J. Kogut, X. Li, and M. J. DiPirro, “Design of the PIXIE adiabatic demagnetization refrigerators,” *Cryogenics*, vol. 52, pp. 140–144, Apr. 2012.
- [63] D. J. Fixsen, A. Kogut, R. S. Hill, P. C. Nagler, L. T. Seals, and J. M. Howard, “Dealing with beam structure in PIXIE,” in *Society of Photo-Optical Instrumentation Engineers (SPIE) Conference Series*, vol. 9914 of *Proc. SPIE*, p. 99141B, July 2016.
- [64] J. Aumont, L. Conversi, C. Thum, H. Wiesemeyer, E. Falgarone, J. F. Macías-Pérez, F. Piacentini, E. Pointecouteau, N. Ponthieu, J. L. Puget, C. Rosset, J. A. Tauber, and M. Tristram, “Measurement of the Crab nebula polarization at 90 GHz as a calibrator for CMB experiments,” *Astron. & Astrophys.*, vol. 514, p. A70, May 2010.
- [65] J. C. Mather, “Bolometer noise: nonequilibrium theory,” *Applied Optics*, vol. 21, pp. 1125–1129, Mar. 1982.
- [66] A. H. Guth, “Inflationary universe: A possible solution to the horizon and flatness problems,” *Phys. Rev. D*, vol. 23, pp. 347–356, Jan. 1981.

- [67] R. H. Brandenberger, “Alternatives to the Inflationary Paradigm of Structure Formation,” in *International Journal of Modern Physics Conference Series*, vol. 1 of *International Journal of Modern Physics Conference Series*, pp. 67–79, 2011.
- [68] R. A. Sunyaev and Y. B. Zeldovich, “Small-Scale Fluctuations of Relic Radiation,” *Astrophysics and Space Science*, vol. 7, pp. 3–19, Apr. 1970.
- [69] Planck Collaboration, N. Aghanim, M. Arnaud, M. Ashdown, J. Aumont, C. Baccigalupi, A. J. Banday, R. B. Barreiro, J. G. Bartlett, N. Bartolo, and et al., “Planck 2015 results. XXII. A map of the thermal Sunyaev-Zeldovich effect,” *Astron. & Astrophys.*, vol. 594, p. A22, Sept. 2016.
- [70] Planck Collaboration, P. A. R. Ade, N. Aghanim, M. Arnaud, M. Ashdown, J. Aumont, C. Baccigalupi, A. J. Banday, R. B. Barreiro, N. Bartolo, and et al., “Planck 2015 results. XXI. The integrated Sachs-Wolfe effect,” *Astron. & Astrophys.*, vol. 594, p. A21, Sept. 2016.
- [71] E. Wolf, “Coherence properties of partially polarized electromagnetic radiation,” *Il Nuovo Cimento*, vol. 13, no. 6, pp. 1165–1181, 1959.
- [72] J. N. Goldberg, A. J. Macfarlane, E. T. Newman, F. Rohrlich, and E. C. G. Sudarshan, “Spin-s Spherical Harmonics and δ ,” *Journal of Mathematical Physics*, vol. 8, pp. 2155–2161, Nov. 1967.
- [73] D. Baumann, M. G. Jackson, P. Adshead, A. Amblard, A. Ashoorioon, N. Bartolo, R. Bean, M. Beltrán, F. de Bernardis, S. Bird, X. Chen, D. J. H. Chung, L. Colombo, A. Cooray, P. Creminelli, S. Dodelson, J. Dunkley, C. Dvorkin, R. Easther, F. Finelli, R. Flauger, M. P. Hertzberg, K. Jones-Smith, S. Kachru, K. Kadota, J. Khoury, W. H. Kinney, E. Komatsu, L. M. Krauss, J. Lesgourgues, A. Liddle, M. Liguori, E. Lim, A. Linde, S. Matarrese, H. Mathur,

- L. McAllister, A. Melchiorri, A. Nicolis, L. Pagano, H. V. Peiris, M. Peloso, L. Pogosian, E. Pierpaoli, A. Riotto, U. Seljak, L. Senatore, S. Shandera, E. Silverstein, T. Smith, P. Vaudrevange, L. Verde, B. Wandelt, D. Wands, S. Watson, M. Wyman, A. Yadav, W. Valkenburg, and M. Zaldarriaga, “Probing Inflation with CMB Polarization,” in *American Institute of Physics Conference Series* (S. Dodelson, D. Baumann, A. Cooray, J. Dunkley, A. Fraisse, M. G. Jackson, A. Kogut, L. Krauss, M. Zaldarriaga, and K. Smith, eds.), vol. 1141 of *American Institute of Physics Conference Series*, pp. 10–120, June 2009.
- [74] J. Chluba, “Science with CMB spectral distortions,” *ArXiv e-prints*, May 2014.
- [75] Y. B. Zeldovich and R. A. Sunyaev, “The Interaction of Matter and Radiation in a Hot-Model Universe,” *Astrophysics and Space Science*, vol. 4, pp. 301–316, July 1969.
- [76] R. A. Sunyaev and R. Khatri, “Unavoidable CMB Spectral Features and Blackbody Photosphere of Our Universe,” *International Journal of Modern Physics D*, vol. 22, p. 1330014, June 2013.
- [77] H. Tashiro, “CMB spectral distortions and energy release in the early universe,” *Progress of Theoretical and Experimental Physics*, vol. 2014, p. 06B107, June 2014.
- [78] G. R. Blumenthal and R. J. Gould, “Bremsstrahlung, Synchrotron Radiation, and Compton Scattering of High-Energy Electrons Traversing Dilute Gases,” *Reviews of Modern Physics*, vol. 42, pp. 237–271, 1970.
- [79] G. F. Smoot, “CMB Synchrotron Foreground,” in *Microwave Foregrounds* (A. de Oliveira-Costa and M. Tegmark, eds.), vol. 181 of *Astronomical Society of the Pacific Conference Series*, p. 61, 1999.

- [80] A. M. Hillas, “The Origin of Ultra-High-Energy Cosmic Rays,” *Annual Review of Astronomy and Astrophysics*, vol. 22, pp. 425–444, 1984.
- [81] Planck Collaboration, R. Adam, P. A. R. Ade, N. Aghanim, M. I. R. Alves, M. Arnaud, M. Ashdown, J. Aumont, C. Baccigalupi, A. J. Banday, and et al., “Planck 2015 results. X. Diffuse component separation: Foreground maps,” *Astron. & Astrophys.*, vol. 594, p. A10, Sept. 2016.
- [82] M. Vidal, C. Dickinson, R. D. Davies, and J. P. Leahy, “Polarized radio filaments outside the Galactic plane,” *Mon. Not. R. Astron. Soc.*, vol. 452, pp. 656–675, Sept. 2015.
- [83] L. La Porta, C. Burigana, W. Reich, and P. Reich, “The impact of Galactic synchrotron emission on CMB anisotropy measurements. I. Angular power spectrum analysis of total intensity all-sky surveys,” *Astron. & Astrophys.*, vol. 479, pp. 641–654, Mar. 2008.
- [84] Planck Collaboration, A. Abergel, P. A. R. Ade, N. Aghanim, M. I. R. Alves, G. Aniano, C. Armitage-Caplan, M. Arnaud, M. Ashdown, F. Atrio-Barandela, and et al., “Planck 2013 results. XI. All-sky model of thermal dust emission,” *Astron. & Astrophys.*, vol. 571, p. A11, Nov. 2014.
- [85] D. P. Finkbeiner, M. Davis, and D. J. Schlegel, “Extrapolation of Galactic Dust Emission at 100 Microns to Cosmic Microwave Background Radiation Frequencies Using FIRAS,” *ApJ*, vol. 524, pp. 867–886, Oct. 1999.
- [86] A. Kogut and D. J. Fixsen, “Foreground Bias from Parametric Models of Far-IR Dust Emission,” *ApJ*, vol. 826, p. 101, Aug. 2016.
- [87] Planck Collaboration, P. A. R. Ade, N. Aghanim, M. I. R. Alves, C. Armitage-Caplan, M. Arnaud, M. Ashdown, F. Atrio-Barandela, J. Aumont, C. Bacci-

- galupi, and et al., “Planck 2013 results. XIII. Galactic CO emission,” *Astron. & Astrophys.*, vol. 571, p. A13, Nov. 2014.
- [88] Planck Collaboration, R. Adam, P. A. R. Ade, N. Aghanim, M. I. R. Alves, M. Arnaud, M. Ashdown, J. Aumont, C. Baccigalupi, A. J. Banday, and et al., “Planck 2015 results. X. Diffuse component separation: Foreground maps,” *ArXiv e-prints*, Feb. 2015.
- [89] J. S. Greaves, W. S. Holland, P. Friberg, and W. R. F. Dent, “Polarized CO Emission from Molecular Clouds,” *ApJ*, vol. 512, pp. L139–L142, Feb. 1999.
- [90] G. Puglisi, G. Fabbian, and C. Baccigalupi, “A 3D model for CO molecular line emission as a potential CMB polarization contaminant,” *ArXiv e-prints*, Jan. 2017.
- [91] P. C. Nagler, D. J. Fixsen, A. Kogut, and G. S. Tucker, “Systematic Effects in Polarizing Fourier Transform Spectrometers for Cosmic Microwave Background Observations,” *Astrophys. J. Supp.*, vol. 221, p. 21, Nov. 2015.
- [92] R. C. Jones, “New calculus for the treatment of optical systems. I. Description and discussion of the calculus,” *Journal of the Optical Society of America (1917-1983)*, vol. 31, p. 488, July 1941.
- [93] H. Mueller, “Memorandum on the polarization optics of the photo-elastic shutter,” tech. rep., 1943.
- [94] M. Born and E. Wolf, *Principles of Optics*. Oct. 1999.
- [95] J. J. Bock, A. E. Lange, M. K. Parikh, and M. L. Fischer, “Emissivity measurements of reflective surfaces at near-millimeter wavelengths,” *Applied Optics*, vol. 34, pp. 4812–4816, Aug. 1995.

- [96] D. T. Chuss, E. J. Wollack, R. Henry, H. Hui, A. J. Juarez, M. Krejny, S. H. Moseley, and G. Novak, “Properties of a variable-delay polarization modulator,” *Applied Optics*, vol. 51, p. 197, Jan. 2012.
- [97] L. D. Spencer, D. A. Naylor, P. A. R. Ade, and J. Zhang, “Beam-splitter effects in dual-input Fourier transform spectroscopy,” *Journal of the Optical Society of America A*, vol. 28, p. 1805, Sept. 2011.
- [98] W. Hu, M. M. Hedman, and M. Zaldarriaga, “Benchmark parameters for CMB polarization experiments,” *Phys. Rev. D*, vol. 67, p. 043004, Feb. 2003.
- [99] J. R. Connes, *Recherches sur la spectroscopie par transformations de Fourier*. Éd. de la" Revue d'optique théorique et instrumentale, 1961.
- [100] M. L. Forman, W. H. Steel, and G. A. Vanasse, “Correction of Asymmetric Interferograms Obtained in Fourier Spectroscopy,” *Journal of the Optical Society of America (1917-1983)*, vol. 56, p. 59, Jan. 1966.
- [101] H. Sakai, G. A. Vanasse, and M. L. Forman, “Spectral Recovery in Fourier Spectroscopy,” *Journal of the Optical Society of America (1917-1983)*, vol. 58, p. 84, Jan. 1968.
- [102] R. J. Bell, *Introductory Fourier transform spectroscopy*. 1972.
- [103] L. Mertz, “Auxiliary computation for Fourier spectrometry,” *Infrared Physics*, vol. 7, pp. 17–23, Mar. 1967.
- [104] D. J. Fixsen, E. S. Cheng, D. A. Cottingham, R. E. Eplee, Jr., T. Hewagama, R. B. Isaacman, K. A. Jensen, J. C. Mather, D. L. Massa, S. S. Meyer, P. D. Noerdlinger, S. M. Read, L. P. Rosen, R. A. Shafer, A. R. Trenholme, R. Weiss, C. L. Bennett, N. W. Boggess, D. T. Wilkinson, and E. L. Wright, “Calibration of the COBE FIRAS instrument,” *ApJ*, vol. 420, pp. 457–473, Jan. 1994.

- [105] A. Kogut, G. F. Smoot, C. L. Bennett, E. L. Wright, J. Aymon, G. de Amici, G. Hinshaw, P. D. Jackson, E. Kaita, P. Keegstra, C. Lineweaver, K. Loewenstein, L. Rokke, L. Tenorio, N. W. Boggess, E. S. Cheng, S. Gulkis, M. G. Hauser, M. A. Janssen, T. Kelsall, J. C. Mather, S. Meyer, S. H. Moseley, T. L. Murdock, R. A. Shafer, R. F. Silverberg, R. Weiss, and D. T. Wilkinson, “COBE Differential Microwave Radiometers - Preliminary systematic error analysis,” *ApJ*, vol. 401, pp. 1–18, Dec. 1992.
- [106] W. A. Holmes, J. J. Bock, B. P. Crill, T. C. Koch, W. C. Jones, A. E. Lange, and C. G. Paine, “Initial test results on bolometers for the Planck high frequency instrument,” *Applied Optics*, vol. 47, pp. 5996–6008, Nov. 2008.
- [107] A. Kusaka, E. J. Wollack, and T. R. Stevenson, “Angular and polarization response of multimode sensors with resistive-grid absorbers,” *Journal of the Optical Society of America A*, vol. 31, p. 1557, July 2014.
- [108] Planck Collaboration, P. A. R. Ade, N. Aghanim, C. Armitage-Caplan, M. Arnaud, M. Ashdown, F. Atrio-Barandela, J. Aumont, C. Baccigalupi, A. J. Banday, and et al., “Planck 2013 results. X. HFI energetic particle effects: characterization, removal, and simulation,” *Astron. & Astrophys.*, vol. 571, p. A10, Nov. 2014.
- [109] B. I. Shklovskii and A. L. Efros, *Electronic properties of doped semiconductors*, vol. 45. Springer Science & Business Media, 2013.
- [110] R. L. Kelley, K. Mitsuda, C. A. Allen, P. Arsenovic, M. D. Audley, T. G. Bialas, K. R. Boyce, R. F. Boyle, S. R. Breon, G. V. Brown, J. Cottam, M. J. Dipirro, R. Fujimoto, T. Furusho, K. C. Gendreau, G. G. Gochar, O. Gonzalez, M. Hirabayashi, S. S. Holt, H. Inoue, M. Ishida, Y. Ishisaki, C. S. Jones, R. Keski-Kuha, C. A. Kilbourne, D. McCammon, U. Morita, S. H. Moseley,

- B. Mott, K. Narasaki, Y. Ogawara, T. Ohashi, N. Ota, J. S. Panek, F. S. Porter, A. Serlemitsos, P. J. Shirron, G. A. Sneiderman, A. E. Szymkowiak, Y. Takei, J. L. Tveekrem, S. M. Volz, M. Yamamoto, and N. Y. Yamasaki, “The Suzaku High Resolution X-Ray Spectrometer,” *PASJ*, vol. 59, pp. 77–112, Jan. 2007.
- [111] InterFET Corporation, *NJ14AL Junction Field-Effect Transistor Process*, 01 1999. <http://www.interfet.com/Process/NJ14AL>.
- [112] F. S. Porter, J. S. Adams, G. V. Brown, J. A. Chervenak, M. P. Chiao, R. Fujimoto, Y. Ishisaki, R. L. Kelley, C. A. Kilbourne, D. McCammon, K. Mitsuuda, T. Ohashi, A. E. Szymkowiak, Y. Takei, M. Tashiro, and N. Yamasaki, “The detector subsystem for the SXS instrument on the ASTRO-H Observatory,” in *Space Telescopes and Instrumentation 2010: Ultraviolet to Gamma Ray*, vol. 7732 of *Proc. SPIE*, p. 77323J, July 2010.
- [113] R. C. Jones, “The general theory of bolometer performance,” *Journal of the Optical Society of America (1917-1983)*, vol. 43, pp. 1–10, Jan. 1953.
- [114] P. L. Richards, “Bolometers for infrared and millimeter waves,” *Journal of Applied Physics*, vol. 76, pp. 1–24, July 1994.
- [115] A.-D. Brown, W.-T. Hsieh, S. H. Moseley, T. R. Stevenson, U. Kongpop, E. J. Wollack, *et al.*, “Fabrication of an absorber-coupled mkid detector and read-out for sub-millimeter and far-infrared astronomy,” in *SPIE Astronomical Telescopes+ Instrumentation*, pp. 77410P–77410P, International Society for Optics and Photonics, 2010.
- [116] K. Rostem. Private communication, 2016.
- [117] Planck Collaboration, A. Abergel, P. A. R. Ade, N. Aghanim, M. I. R. Alves, G. Aniano, C. Armitage-Caplan, M. Arnaud, M. Ashdown, F. Atrio-Barandela,

- and et al., “Planck 2013 results. XI. All-sky model of thermal dust emission,” *Astron. & Astrophys.*, vol. 571, p. A11, Nov. 2014.
- [118] C. Schmidt, “Thermal boundary (Kapitza) resistance at niobium-epoxy interfaces in the superconducting and normal states,” *Phys. Rev. B*, vol. 15, pp. 4187–4192, May 1977.
- [119] A. L. Woodcraft, G. Ventura, V. Martelli, and W. S. Holland, “Thermal conductance at millikelvin temperatures of woven ribbon cable with phosphor-bronze clad superconducting wires,” *Cryogenics*, vol. 50, pp. 465–468, Aug. 2010.
- [120] P. Duthil, “Material Properties at Low Temperature,” *ArXiv e-prints*, Jan. 2015.
- [121] P. A. Schroeder, R. Wolf, and J. A. Woollam, “Thermopowers and Resistivities of Silver-Palladium and Copper-Nickel Alloys,” *Physical Review*, vol. 138, pp. 105–111, Apr. 1965.
- [122] Copper Development Association, *Copper-Nickel 90/10 and 70/30 Alloys Technical Data*, 09 1982.
<http://copperalliance.org.uk/docs/librariesprovider5/resources/tn-31-cu-ni-90-10-and-70-30-pdf.pdf>.
- [123] C. Hagmann and P. L. Richards, “Adiabatic demagnetization refrigerators for small laboratory experiments and space astronomy,” *Cryogenics*, vol. 35, pp. 303–309, 1995.
- [124] L. Duband, L. Hui, and A. Lange, “Thermal isolation of large loads at low temperature using Kevlar rope,” *Cryogenics*, vol. 33, pp. 643–647, June 1993.
- [125] F. Rondeaux, P. Bredy, and J. M. Rey, “Thermal conductivity measurements of epoxy systems at low temperature,” in *Advances in Cryogenic Engineering*

- ICMC* (B. Baluchandran, D. Gubser, and K. T. Hartwig, eds.), vol. 614 of *American Institute of Physics Conference Series*, pp. 197–203, May 2002.
- [126] E. J. Wollack, D. T. Chuss, K. Rostem, and K. U-Yen, “Impedance matched absorptive thermal blocking filters,” *Review of Scientific Instruments*, vol. 85, p. 034702, Mar. 2014.
- [127] E. J. Wollack, D. J. Fixsen, R. Henry, A. Kogut, M. Limon, and P. Mirel, “Electromagnetic and Thermal Properties of a Conductively Loaded Epoxy,” *International Journal of Infrared and Millimeter Waves*, vol. 29, pp. 51–61, Jan. 2008.
- [128] A. S. Sedra and K. C. Smith, *Microelectronic Circuits*. Oxford University Press, fifth ed., 2004.
- [129] National Aeronautics and Space Administration, *Announcement of Opportunity, Astrophysics Explorers Program, 2016 Medium Explorer (MIDEX)*, 09 2016. <https://nspires.nasaprs.com/external>.
- [130] National Aeronautics and Space Administration, *General Environmental Verification Standard (GEVS) For GSFC Flight Programs and Projects*, 04 2013. <https://standards.nasa.gov/standard/gsfcs/gsfcs-std-7000>.